2018-05-02

Multiple resonant multiconductor transmission line resonator design using circulant block matrix algebra

Sasidhar Tadanki
Worcester Polytechnic Institute

Multiple resonant multiconductor transmission line resonator design using circulant block matrix algebra

By

Sasidhar Tadanki

A Dissertation
Submitted to the Faculty
of the

WORCESTER POLYTECHNIC INSTITUTE

in partial fulfillment of the requirements for
the Degree of Doctor of Philosophy
in
Electrical and Computer Engineering

May 2018

Approved by the

Dissertation Committee:

Prof. Reinhold Ludwig, Advisor

Prof. Sergey N. Makarov, Member

Prof. John M. Sullivan Jr, Member

Dr. Yoshinori Hamamura, Member

Dedication

ॐ गुरु ब्रह्म गुरु विष्णु गुरु देवो महेश्वर
गुरु साक्षात्परंब्रह्म तस्मै श्री गुरवे नमः

Guru Brahma, Guru Vishnu, Guru Devo Maheshwara
Guru Saakshaat, Param Brahma,
Tasmai Shree Guruvey Namaha

The Guru (teacher) is Brahma (The God of Creation)
The Guru is Vishnu (The God of Sustenance)
The Guru is Shiva (The God of Annihilation)
My Salutation to such a Guru, who is verily the Supreme God

I would like to dedicate this research to my advisors, my faculty, my teachers and all the people who directly and indirectly imparted knowledge in me

Acknowledgments

Foremost, I would like to thank my advisor Prof. Reinhold Ludwig for introducing me to the wonderful field of multiconductor transmission lines and also for providing me with the opportunity to pursue my doctoral studies at the WPI. I am thankful to him for the tremendous academic and financial support provided to me throughout my graduate studies.

I would like to express my appreciation to Dr. Gene Bogdanov, WPI whose work has formed the basis for my research. Without his insights and suggestions, this work would not have been possible.

With a great pleasure, I want to thank members of my Ph.D. committee, Prof Sergey Makarov, Prof John Sullivan, and Dr. Yoshinori Hamamura for their time and efforts. It was such a great honor to have them on my committee

I want to thank Mat Brevard and Chris Refuse for helping me with coil building and testing.

I must express my gratitude to Prof John Gore, Vanderbilt university institute of imaging sciences (VUIIS) for supporting me and allowing me to use his 7T scanner.

A big thanks should go to my former and current colleagues at WPI, INSL, Phillips medical systems, Cleveland, Vanderbilt University, Nashville and Canon medical research USA, Cleveland for helping me at various stages my thesis.

I want to thank my friends at Salisbury estate and acquaintances at Indian student organization, WPI for making my stay at Worcester a memorable thing.

Lastly, I am deeply thankful to my parents, sisters, and my in-laws for their support and encouragement throughout my career. This last word of acknowledgment is for my dear wife Dr. Pavansirisha Kallakuri, who made a lot of sacrifices to see me achieve the end of my Ph.D. dream.

Table of Contents

List of Figures

List of Tables

Abstract

The purpose of this dissertation is to provide a theoretical model to design RF coils using multiconductor transmission line (MTL) structures for MRI applications. In this research, an MTL structure is represented as a multiport network using its port admittance matrix. Resonant conditions and closed-form solutions for different port resonant modes are calculated by solving the eigenvalue problem of port admittance matrix using block matrix algebra.

A mathematical proof to show that the solution of the characteristic equation of the port admittance matrix is equivalent to solving the source side input impedance is presented. The proof is derived by writing the transmission chain parameter matrix of an MTL structure, and mathematically manipulating the chain parameter matrix to produce a solution to the characteristic equation of the port admittance matrix.

A port admittance matrix can be formulated to take one of the forms depending on the type of MTL structure: a circulant matrix, or a circulant block matrix (CB), or a block circulant circulant block matrix (BCCB). A circulant matrix can be diagonalized by a simple Fourier matrix, and a BCCB matrix can be diagonalized by using matrices formed from Kronecker products of Fourier matrices. For a CB matrix, instead of diagonalizing to compute the eigenvalues, a powerful technique called "reduced dimension method" can be used.

In the reduced dimension method, the eigenvalues of a circulant block matrix are computed as a set of the eigenvalues of matrices of reduced dimension. The required reduced dimension matrices are created using a combination of the polynomial representor of a circulant matrix and a permutation matrix. A detailed mathematical formulation of the reduced dimension method is presented in this thesis. With the application of the reduced dimension method for a 2n+1 MTL structure, the computation of eigenvalues for a 4n X 4n port admittance matrix is simplified to the computation of eigenvalues of 2n matrices of size 2 X 2. In addition to reduced computations, the model also facilitates analytical formulations for coil resonant conditions.

To demonstrate the effectiveness of the proposed methods (2n port model and reduced dimension method), a two-step approach was adopted. First, a standard published RF coil was analyzed using the proposed models. The obtained resonant conditions are then compared with the published values and are verified by full-wave numerical simulations. Second, two new dual tuned coils, a surface coil design using the 2n port model, and a volume coil design using the reduced dimensions method are proposed, constructed, and bench tested. Their validation was carried out by employing 3D EM simulations as well as undertaking MR imaging on clinical scanners. Imaging experiments were conducted on phantoms, and the investigations indicate that the RF coils achieve good performance characteristics and a high signal-to-noise ratio in the regions of interest.

Chapter 1

Introduction and thesis outline

1.1 Introduction

Magnetic resonance imaging (MRI) is a noninvasive clinical imaging methodology, which uses principles of nuclear magnetic resonance to generate images of protons in biological tissues. The current clinical standard employ imagers with magnetic fields up to 3 Tesla [1]. However, with the advent of high field imaging scanners (field strength above 3T), there is a considerable interest in imaging of other nuclei [2]. Even though RF coil technology is a mature technology, coil designs for higher field strengths and other nuclei are still evolving [3].

1.2 Motivation

Volume resonator designs have been used successfully in various high and ultrahigh-field MRI applications [4][5]. Some of the commonly used volume resonator designs are the single-tuned coupled multiconductor transmission line resonator (CMTL) [4], the classical single-tuned [5] and dual-tuned [6] TEM resonator, the shielded birdcage design [7], and various multichannel configurations [8]–[11]. Most of the designs mentioned above are derived from multiconductor transmission line (MTL) arrays.

In general, a standard MTL is an $(n+1)$-element structure composed of n conducting strips/conductors inside a conductive shield (acting as a ground) and terminated by an impedance network [4],[5]. The operating characteristics of an MTL depend upon the distinct terminating conditions at the conductor terminals. For example, an MTL composed of microstrips is transformed into a single-tuned CMTL by terminating its microstrips with capacitive loads [4]. An MTL structure is similarly altered into a dual-tuned TEM resonator by using different capacitive terminations on alternating conductors[2],[3]. An MTL constructed with coaxial conductors can be converted into a classical, single-tuned TEM resonator by terminating the coaxial conductors to the shield by using end loads (realized by using either open or short-

circuited coaxial transmission lines) [5]. Furthermore, multichannel, volume strip arrays for both single resonance and dual resonance operation can be realized by decoupling and terminating the MTL with a proper capacitive or inductive terminations [8]–[11]. Very few attempts have been made to develop a unified model to understand the different, realizable configurations of MTL and their termination requirements.

The objective of this thesis is to present a simple approach to design RF coils for both single and multiple resonances. The practical objective is to produce a volume and surface multi-resonant multiconductor RF coil design.

1.3 Thesis outline

In this thesis, a new design procedure to determine resonant conditions for a multiconductor transmission line resonator is proposed. The MTL is represented as a multiport network using its port admittance matrix. The port admittance matrix is generated and rearranged to retain a circulant block nature. Closed form solutions for different port resonant modes are calculated by solving the eigenvalue problem of an admittance matrix using the block matrix algebra.

The dissertation is organized as follows:

Chapter 2 introduces the basic principles of NMR and MRI. A brief overview of an MR signal is presented, and a general formulation for a signal from the magnetization vector is described using principles of magnetic resonance. In later sections, introductory MR imaging and details of MR instrumentation with a required glossary of terms are presented.

Chapter 3 introduces a brief survey of existing techniques for obtaining resonant conditions for volume resonators. After the introductory section, a multiport representation of an MTL structure using the port admittance matrix is presented, and numerous ways of calculating the admittance matrix are described. In the subsequent theory section, a short but an essential block matrix algebra terminology is presented which is then followed by a mathematical proof for determining the resonant condition using the admittance

matrix. Closed form solutions for port resonant mode frequencies are calculated by applying the Kronecker product operated Fourier matrices on the port admittance matrix. The practical utility of the proposed method is demonstrated with a novel dual tuned dual element surface coil design.

Chapter 4 contains a literature survey covering key publications of multi-resonant volume coils. The multiport model proposed in Chapter 3 is extended to determine the resonating conditions for multi-tuning of transmission line resonators. Closed form solutions for different port resonant modes are calculated by solving the eigenvalue problem of the admittance matrix, using the reduced dimension method. When applying the reduced dimension method, an eigenvalue problem for a circulant-block matrix is decomposed into a set of eigenvalue problems of reduced dimension matrices. A detailed formulation is presented, and simulated results are compared with standard published results. Two new dual tuned head coils, a) phosphorus-31 (162.09 MHz) and sodium-23(105.9 MHz), b) sodium-23(105.9 MHz) and oxygen-19(53.2MHz) for a 9.4T human MRI system are analyzed and developed, and their validation is presented.

Chapter 5 concludes with a summary of achievements and outlines future work.

The following topics are covered in the appendix sections: Examples of commonly used matrices in this thesis, a hand calculated example which demonstrates the reduced dimension method, port admittance matrices of different MTL structures, PCB layouts, and the list of components used in the proposed coils.

Chapter 2

Basic principles of MRI

2.1 Introduction

Purcell [12] and Bloch [13] received the 1952 physics Nobel Prize for describing the property of Nuclear Magnetic Resonance (NMR) in 1946. Since then NMR has found its application in the field of chemical analysis. In 1973, Lauterbur [14] used the principles of NMR to describe an imaging technique for determining the physical structure. Following Lauterbur's breakthrough research, Magnetic Resonance (MR) has been used as an imaging tool in many biomedical, chemical and engineering applications [15].

This current chapter is introductory in nature and presents basic principles of NMR and MRI specifically a brief overview of an MR signal is given. Using principles of MR, a general formulation of the signal from the magnetization vector is described. The basics of MR imaging and details of MR instrumentation are presented in later sections.

2.2 A brief overview of MR signal

The property of spin angular momentum can be described using a quantum mechanical description of atomic nuclei. The spin angular momentum is characterized by the spin quantum number I which is an intrinsic property of the nucleus. The total spin angular momentum is Ih, where h is Planck's constant. Spin quantum numbers for some atomic nuclei are shown in Table 1. The model of spinning nuclei forms the basis for the phenomenon of nuclear magnetic resonance [16].

The property of magnetic resonance is exhibited when the nuclei have a non-zero value of I. The proton (^{1}H) becomes the nucleus of interest, because of its high natural abundance. However, other nuclei have also been studied.

Table 1: Properties of NMR nuclei

Nucleus	Spin (I)	$\gamma/2\pi$ (MHz/T)	Natural Abundance (% of Mass)	Biological Abundance (% of Mass)
^{1}H	$1/2$	42.576	99.985	10
^{13}C	$1/2$	10.705	1.10	0.198
^{17}O	$5/2$	-5.772	0.048	0.025
^{23}Na	$3/2$	11.262	100	0.15
^{31}P	$1/2$	17.235	100	1

When placed in a static magnetic field, a nucleus with a spin will precess around the axis of the applied field. A nuclear spin is similar to a spinning top, which precesses about its vertical axis under the torque of the gravitational field. With the above picture in mind, the following facts can be derived from Bloch equations [17].

- The rate of precession of a nucleus in a magnetic field **B** is proportional to the net strength of the magnetic field it is experiencing. The rate of precession, known as Larmor frequency is given by (1),

$$\omega = \gamma \mathbf{B} \tag{1}$$

- A nucleus emits no signal when it is in equilibrium, i.e., when its spin is aligned with the applied magnetic field. When external stimuli, in the form of RF pulses, disturb the alignment, nuclei tend to relax to equilibrium by emitting signals.

As the precession frequency is dependent on the static magnetic field, any variation in the field will change the precession frequency. A controlled non-uniform magnetic field created in space can be used to encode the spatial spin density information. The controlled non-uniformity forms the basis for Magnetic Resonance Imaging [5].

2.3 Mathematical principles of NMR

For a spin magnetization vector $\boldsymbol{M}$ placed in a magnetic field $\mathbf{B}$, the Bloch equation, neglecting relaxation effects, can be written as

$$\frac{d\boldsymbol{M}}{dt} = \gamma \boldsymbol{M} \times \mathbf{B} \tag{2}$$

Here, γ is the gyromagnetic ratio and $\mathbf{B}$ is the static magnetic field along the z-axis, such that $\mathbf{B} = \mathrm{B_o}\boldsymbol{z}$

Writing the Bloch equation in Cartesian form leads to following equations

$$\frac{dM_x}{dt} = \gamma M_y \mathrm{B}_0 \tag{3}$$

$$\frac{dM_y}{dt} = -\gamma M_x \mathrm{B}_0 \tag{4}$$

$$\frac{dM_z}{dt} = 0 \tag{5}$$

The above equations have the following solution

$$M_x(t) = M_x^0 \cos\omega_0 t - M_y^0 \sin\omega_0 t \tag{6}$$

$$M_y(t) = M_x^0 \sin\omega_0 t + M_y^0 \cos\omega_0 t \tag{7}$$

$$M_z(t) = M_z^0 \tag{8}$$

where M_y^0, M_y^0 and M_z^0 are components of the initial magnetization, and $\omega_0 = \gamma\mathbf{B_0}$ is called the Larmor frequency.

Consider an RF field $\mathbf{B_1}$ with a precession frequency ω_0, $\mathbf{B_1}$ (t) is its circularly polarized component rotating in the same direction as the precessing magnetization vector and is given as

$$\mathbf{B}_1(t) = \mathrm{B}_1 \cos\omega_0 t\, \boldsymbol{x} - \mathrm{B}_1 \sin\omega_0 t\, \mathbf{y} \tag{9}$$

If $\mathbf{B}_1(t)$ is applied perpendicularly to $\mathbf{B}$, then substituting $\mathbf{B}_1(t)$ in the Bloch equation results in

$$\frac{dM_x}{dt} = \gamma\,(M_y \mathrm{B}_0 + M_z\,\mathrm{B}_1 \sin\omega_0 t\,) \quad (10)$$

$$\frac{dM_y}{dt} = -\gamma\,(M_x \mathrm{B}_0 - M_z\,\mathrm{B}_1 \cos\omega_0 t\,) \quad (11)$$

$$\frac{dM_z}{dt} = -\gamma\,(M_x \mathrm{B}_1 \sin\omega_0 t + M_y \mathrm{B}_1 \cos\omega_0 t\,) \quad (12)$$

If the initial condition $M(0) = M^0$ is defined, then the solution for $\boldsymbol{M}$ is given as

$$M_x(t) = M^0 \sin\omega_1 t \sin\omega_0 t \quad (13)$$

$$M_y(t) = M^0 \sin\omega_1 t \cos\omega_0 t \quad (14)$$

$$M_z(t) = M^0 \cos\omega_1 t \quad (15)$$

where $\omega_1 = \gamma \mathbf{B}_1$.

From above equations, it follows that by applying an oscillating magnetic field of frequency ω_1, the magnetization simultaneously precesses around $\mathbf{B_0}$ at ω_0 and $\mathbf{B_1}$ at ω_1.

To understand the evolution of the magnetization vector, it is necessary to make $\mathbf{B_0}$ static in the frame of reference; this is achieved by considering a new rotating frame of reference, which rotates about the z-axis at a frequency ω_0. The modified set of unit vectors now become

$$\boldsymbol{x}'(t) = \cos\omega_0 t\,\boldsymbol{x} + \sin\omega_0 t\,\boldsymbol{y} \quad (16)$$

$$\boldsymbol{y}'(t) = -\sin\omega_0 t\,\boldsymbol{x} + \cos\omega_0 t\,\boldsymbol{y} \quad (17)$$

$$\boldsymbol{z}'(t) = \boldsymbol{z} \quad (18)$$

In the new rotating frame of reference, equation (2) becomes

$$\frac{d\boldsymbol{M}}{dt} = \gamma\,\boldsymbol{M} \times \mathbf{B_{eff}} \quad (19)$$

where $\mathbf{B_{eff}} = \left(\mathrm{B}_0 - \frac{\omega}{\gamma}\right)\boldsymbol{z}' + \mathrm{B}_1\boldsymbol{x}'$ and $\boldsymbol{x}', \boldsymbol{y}'$ and $\boldsymbol{z}'$ are unit vectors in the transformed frame of reference.

The result of solving the equation (19) is a magnetization vector, which precess about $\mathbf{B_{eff}}$.

When a pulse of the $\mathbf{B_1}$ field is applied, based on the duration of the pulse t, the magnetization vector will rotate at an angle $\theta = \gamma B_1 t$. In a typical MR experiment, a pulse is applied, which tips the magnetization vector from the longitudinal plane (parallel to $\mathbf{B_0}$) to the transverse plane (perpendicular to $\mathbf{B_0}$) [18]. The precessing magnetization vector in the transverse plane induces an MR signal voltage in the RF coil.

2.3.1 Effects of relaxation

Spins are disturbed with the application of RF energy, and once the excitation is removed, the spins will tend to relax back to their original equilibrium due to the effects of relaxation. There are two kinds of relaxations: spin-lattice relaxation and spin-spin relaxation that cause the spin system to evolve back to its equilibrium state [16].

Spin-lattice relaxation

Spin systems which are in an excited state attempt to return to their original equilibrium state by exchanging energy between themselves and their surroundings. Such a process is called spin-lattice relaxation, and it results in the tilting of the magnetization vector away from the transverse plane as shown in Fig. 1. The rate at which equilibrium is restored is characterized by the spin-lattice or longitudinal relaxation time constant T_1. The constant T_1 governs the evolution of M_z towards its equilibrium value M_0.

The spin-lattice relaxation can be modeled by

$$\frac{dM_x}{dt} = -\frac{(M_z - M^0)}{T_1} \tag{20}$$

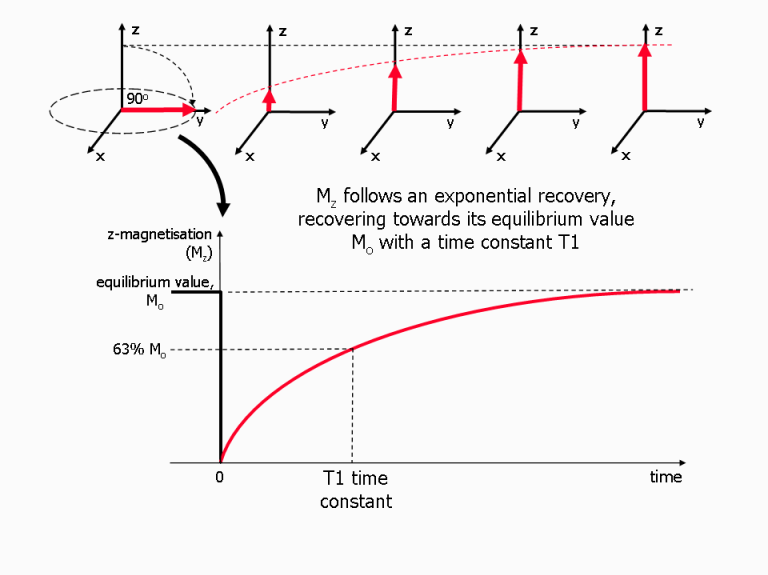

Fig. 1: T_1 relaxation process. Diagram showing the process of T_1 relaxation after a 90° RF pulse is applied at equilibrium. The z component of the net magnetization, M_z is reduced to zero, but then recovers gradually back to its equilibrium value if no further rf pulses are applied. The recovery of M_z is an exponential process with a time constant T_1. This is the time at which the magnetization has recovered to 63% of its value at equilibrium. (reproduced from [19]).

Spin-spin relaxation

Spin systems oriented at an angle to the static magnetic field tend to lose their transverse magnetization phase coherence due to spin-spin interactions. The loss of phase coherence is characterized by the time constant T_2 or "Spin-spin" relaxation time. T_2 governs the evolution of transverse magnetization $M_x \boldsymbol{x} + M_y \boldsymbol{y}$, towards its equilibrium value of zero. T_2 relaxation is the result of spin-spin interactions and due to the random nature of molecular motion, this process is irreversible. T_2* relaxation accounts for the more rapid decay of the FID signal, however, the additional decay caused by field inhomogeneity can be reversed by the application of a 180° refocusing pulse. There is an additional de-phasing caused by local variations (inhomogeneity's) in the applied magnetic field called T_2* relaxation. T_2* relaxation accounts for the more rapid decay of the FID signal, however, the additional decay caused by field inhomogeneity can be reversed by the application of a 180° refocusing pulse in the MRI experiment. Fig. 2 shows both transverse (T_2 and T_2*) relaxation processes.

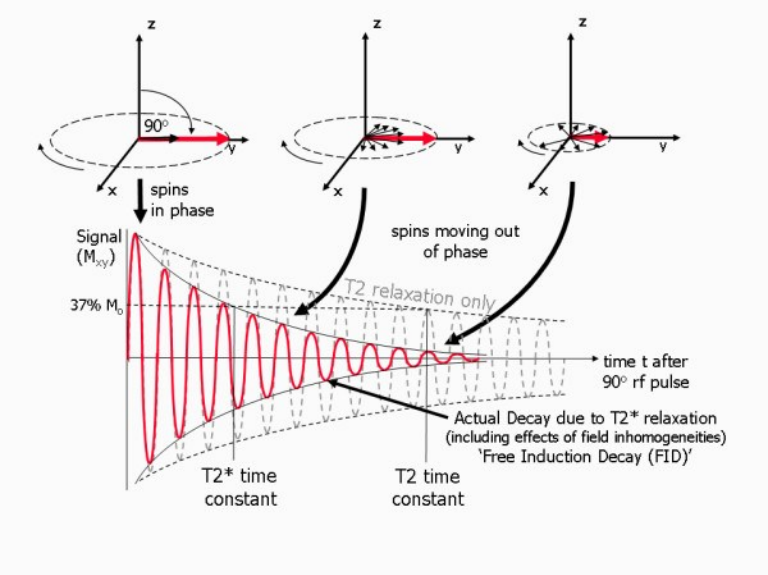

Fig. 2: Transverse (T_2 and T_2*) relaxation processes. A diagram showing the process of transverse relaxation after a 90° RF pulse is applied at equilibrium. Initially, the transverse magnetization (red arrow) has a maximum amplitude as the spins rotate in phase. The amplitude of the net transverse magnetization (and therefore the detected signal) decays as the spins move out of phase with one another (shown by the small black arrows). The overall term for the observed loss of phase coherence (de-phasing) is T_2* relaxation, which combines the effect of T_2 relaxation and additional dephasing caused by local variations (inhomogeneities) in the applied magnetic field. Both T_2 and T_2* are exponential processes with times constants T_2 and T_2* respectively. This is the time at which the magnetization has decayed to 37% of its initial value immediately after the 90° rf pulse. (reproduced from [19]).

Since the T_2* process is reversible for certain MRI experiments, we consider only T_2 for our equations.

The effects of T_2 relaxation are described using the following equations.

$$\frac{dM_x}{dt} = -\frac{M_x}{T_2} \tag{21}$$

$$\frac{dM_y}{dt} = -\frac{M_y}{T_2} \tag{22}$$

By substituting the effects of relaxation into the Bloch equation and writing them in the rotating frame of the system with angular frequency ω, it follows

$$\frac{dM_x}{dt} = \gamma\left(\mathrm{B}_0 - \frac{\omega}{\gamma}\right)M_y - \frac{M_x}{T_2} \tag{23}$$

$$\frac{dM_y}{dt} = \gamma \mathrm{B}_1 M_z - \gamma\left(\mathrm{B}_0 - \frac{\omega}{\gamma}\right)M_y - \frac{M_y}{T_2} \tag{24}$$

$$\frac{dM_z}{dt} = \gamma \mathrm{B}_1 M_y - \frac{(M_z - M^0)}{T_1} \tag{25}$$

The initial components of the magnetization vector after application of an RF pulse (which tips the magnetization vector at an angle Θ with respect to applied magnetic field B_0) are

$$M_x(t) = 0 \quad (26)$$

$$M_y(t) = M^0 \sin\Theta \quad (27)$$

$$M_z(t) = M^0 \cos\Theta \quad (28)$$

The solution of the Bloch equations is given by

$$M_x(t) = M^0 \sin\Theta \sin\omega_0 t \; exp\left[-\frac{t}{T_2}\right] \quad (29)$$

$$M_y(t) = M^0 \sin\Theta \cos\omega_0 t \; exp\left[-\frac{t}{T_2}\right] \quad (30)$$

$$M_z(t) = \mathrm{M}^0\left[1-(1-\cos\Theta)exp\left[-\frac{t}{T_2}\right]\right] \quad (31)$$

It is convenient to express the transverse component of the magnetization by defining a complex quantity

$$\boldsymbol{S} = M_x + jM_y \quad (32)$$

Then

$$\boldsymbol{S}(t) = M^0 \sin\Theta \, exp\left[j\omega_0 t - \frac{t}{T_2}\right] \quad (33)$$

where $M^0 = M_x^0 + j\,M_y^0$

Equation (33) gives the NMR free induction decay (FID) signal. The NMR signal is detected using an RF coil placed in the transverse plane that is perpendicular to the $\mathbf{B_0}$ field. The EMF induced in the coil is proportional to M_x.

2.4 Basics of MRI

A basic MR image can be defined as a map of spatial nuclear spin density $\rho(\mathbf{r})$, where $\mathbf{r}$ is a point in the region of interest [20]. The information on $\rho(\mathbf{r})$ is obtained by observing the behavior of spins, which are

modulated by using cogent combinations of delays, radio frequency (RF) pulses, and gradients. MR imaging is done by using B_0 (static fields) and B_1 (time-varying RF) fields. The B_0 gradient fields give a spatial dependent effect on the resonant frequency, and the B_1 fields provide a spatial dependent effect on the nutation angles. The following section describes the mathematics of MR imaging.

2.4.1 Mathematics of MR imaging

The fundamental equation, which describes the MR image formation, is the Larmor equation as represented by equation (1). In the presence of gradients **G,** the Larmor equation becomes

$$\omega(\mathbf{r}) = \gamma \mathbf{B}_0 + \gamma \mathbf{G} \cdot \mathbf{r} \tag{34}$$

where ω (rad s^{-1}) is Larmor frequency and γ (rad $T^{-1}s^{-1}$) is the gyromagnetic ratio.

From equation (34) it is evident that a spatially well-defined gradient applied to the nuclear spin results in a spatially dependent Larmor frequency. The signal from the sample in the presence of gradients can then be described by

$$S(t) = \iiint \rho(\boldsymbol{r}) e^{j\,(\gamma \mathbf{B_0} + \gamma \mathbf{G}\cdot\mathbf{r})t}\, d\boldsymbol{r} \tag{35}$$

Let's define a quantity $\boldsymbol{k}$ called reciprocal space vector, which has units of m^{-1} and is defined by

$$\boldsymbol{k} = \frac{1}{2\pi} \gamma \mathbf{G} \mathrm{t} \tag{36}$$

where t is the time duration of application of **G**.

The $\boldsymbol{k}$ space can be traversed either by changing the magnitude of **G** and t, or both. By changing variables and expressing the observed signal as a function of $\boldsymbol{k}$

$$S(\boldsymbol{k}) = \iiint \rho(\boldsymbol{r}) e^{j\,(2\pi \boldsymbol{k}\cdot\mathbf{r})t}\, d\boldsymbol{r} \tag{37}$$

Thus from equation (37), it can be seen that $\rho(\mathbf{r})$ in the conjugate **r**-space can be reconstructed from $S(\boldsymbol{k})$ by the Fourier transformation.

$$\rho(\boldsymbol{r}) \quad = \quad \frac{1}{2\pi}\iiint S(\boldsymbol{k})e^{-j\,(2\pi\boldsymbol{k}\cdot\mathbf{r})}\,d\boldsymbol{k} \tag{38}$$

From equations (35)-(38), it is evident that $\boldsymbol{k}$ is the conjugate variable of **r**. The resolution of the image depends on the $\boldsymbol{k}$-space that is sampled. Imaging techniques that are currently available describe combinations of gradients and RF pulses to fill the $\boldsymbol{k}$-space under different optimized conditions [21].

In NMR imaging, pulse sequences play an important role and are intimately related to image reconstruction algorithms employed. These different pulse sequences describe different ways to sample a $\boldsymbol{k}$-space [18]. The spin density map obtained by various imaging methods is not a real spin density map. It is weighted by relaxation effects of the sample (T_1, T_2 or both). These weighted spin density maps give an extra information and are useful in many applications like flow imaging, clinical imaging, and so forth. In this thesis, a simple GRE sequence and a twisted projection imaging (TPI) sequence are used to quantify the proposed coil designs.

2.5 Magnetic resonance instrumentation

Thus far, we presented the basic concepts of magnetic resonance. In the present section, instrumentation related to magnetic resonance imaging scanner is described. The key components of an MR instrument [22] are illustrated in Fig.3. The important modules include a main magnet, a shim system, a gradient system, an RF system, a host computer and allied electronics for control.

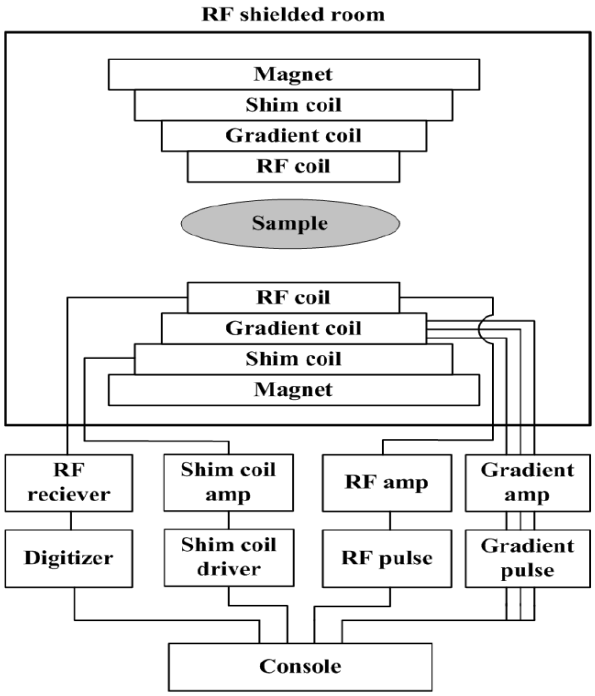

Fig.3: Block diagram of MRI system (reproduced from [22]).

A magnetic resonance instrument is required to produce both static and time-varying magnetic fields. The static fields are produced by the main magnet, shim coils, and the gradient coils. The time-varying magnetic fields are transmitted and received by the RF coils. This thesis primarily deals with the time-varying field generating devices. Consequently, we will limit our discussion to RF coil systems as described in the next section.

2.5.1 RF coil

In MR imaging systems, RF coils are used for two purposes [3]. One is to excite the spin magnetization and the second is to receive signals from relaxing spins. RF coils used for excitation are called transmit coils, and coils used only for receiving purposes are called receive only coils. Coils that are designed to operate as both transmit and receive coils are called transceiver coils. For some applications, resonating loops are used as marker probes [23]. This thesis limits its discussion to transceiver coils.

Tuning

Transmit RF coils, in general, should be able to produce a homogenous B1 field so that they can ensure a uniform excitation in the region of interest. The transmit coils should also have a high efficiency so that the power required to produce a desirable B1 field is at a minimum. The receive coils should have a high sensitivity during the reception to faithfully receive a signal without any distortion and noise addition, as well as to generate high SNR images. To produce high sensitivity and efficiency, coils are made to resonate at the Larmor precession frequency, and the process is called 'tuning of the coil.'

For coils that can be modeled using lumped elements (physical dimension of the longest conductor is less than $\lambda/10$), tuning is done by canceling out the effective reactance by using lumped components. For coil structures made out of distributed elements (like transmission lines or waveguides), tuning is achieved by making their effective electrical length a multiple of $\lambda/2$. In this research, a novel technique to determine the tuning conditions is proposed, which will be explained in detail in subsequent chapters.

Matching

RF coils are connected to MR scanners using a coupling system. A coupling system must maintain the electrical balance of the coil and also should enable an efficient transfer of power to and from the coil. There are two kinds of coupling: inductive and capacitive coupling. Inductive coupling is achieved by a coupling a small loop inductively to the coil. Inductive coupling arrangement allows a good electrical balance between coil and cables connecting to the system. Arcing between the coil and the coupling loop, some field degradation due to the coupling loop are two major problems associated with the inductive coupling. Capacitive coupling is realized by connecting the feed cable across a feed capacitor. Some special care and balun arrangements are required for capacitive coupling to maintain electrical balance. Matching of the coils is done either for efficient power transfer or optimal noise matching of the preamps. A detailed description of matching techniques is provided in specialized RF coil textbooks [3].

Detuning

Most of the MR imaging applications use different coils during transmit and receive cycles. Transmit coils and receive coils needs to be isolated from each other. This isolation is essential for safety reasons, as well as to ensure the fidelity of the associated fields. A detuning circuit is typically used for isolation purposes. Detuning circuit provides a high impedance to the coil, thereby reducing any induced RF currents from other coils. Detuning circuits are implemented using trap circuits or parallel resonant circuits, and this technique is often referred as pole insertion method. Detuning circuits are classified further as active and passive detuning circuits.

Active detuning is accomplished by application of an external bias source to the PIN diodes in the detuning circuit. In an active detuning state, the state of the circuit can be controlled externally, thereby increasing the reliability of detuning mechanism. In passive detuning, the detuning circuit is activated when induced RF energy exceeded a certain level. No external bias is required; this reduces the complexity of implementation. MR original equipment manufacturers (OEM's) insist on the presence of both active and passive circuits for more reliable operation of coils.

Coil arrays

One of the earlier applications of coil arrays is the acquisition of images with a high signal-to-noise ratio (SNR) across a large field of view. The SNR advantage arises because each element in an array responds to their local magnetization while ignoring the magnetization and the noise from the rest of the sample. Receive coil arrays are extensively used in parallel imaging [22],[23]. In parallel imaging, the acquisition time is shortened by under-sampling the k-space in the phase-encoding (and partition-encoding) direction. When the undersampled k-space data is reconstructed, it leads to spatial aliasing in the image domain. By using the sensitivity profiles of the coil arrays, either the missing k-space data is reconstructed, or the spatial aliasing is reduced by unfolding the image. Parallel imaging has had a profound impact on clinical imaging and is used clinically to improve the acquisition time, spatial resolution, temporal resolution and the image quality.

One of the recent emerging applications of coil arrays is imaging with parallel transmission [26]. In parallel transmission, the RF pulses are transmitted on multiple independent transmission channels and coil elements. The RF pulses on a specific channel are independently controlled for a different shape, amplitude, phase, and frequency; thus, providing multiple degrees of freedom that allow a full spatial and temporal control of the excitation field profiles. This control is made possible because of the fast acquisition of excitation field profile maps using novel B_1^+ mapping techniques [27]. The major advantage of parallel transmit is that it greatly shortens the duration of RF pulses for various applications. The benefits of parallel transmit are its potential for reduced SAR [28] and improved B_1 homogeneity at higher field strengths [29].

Decoupling

When two resonating elements coupled to each other either inductively or capacitively, then their frequency splits, and matching becomes difficult [30]. Bad match results in signal loss due to reflection, or increase in noise due to non-optimal match with the preamplifier. Coupled coils sometimes tend to have overlapping sensitive profiles complicating the multitransmit pulse optimization routines for parallel transmit applications, or complicating the parallel reconstructions during the receive cycle of parallel imaging applications.

Several strategies have been proposed for removing the effects of coupling. First, the geometrical overlap of 'nearest neighbor elements' is adjusted to cancel out the shared flux between them [31]. The disadvantage is that it may restrict the geometrical layouts of the coil elements. Alternately, a transformer can be inserted in series in each of the neighboring elements. The transformer is wound to cancel out the mutual inductance[32]. A capacitive decoupling network can be placed between nearest-neighbor coils within the array such that they form a parallel resonant circuit with mutual inductance [30]. All the above-mentioned methods are being used with considerable success. One of the most preferred methods for parallel receive coil arrays is the use of low-input-impedance preamplifiers [31], which limits the currents flowing in each coil and thus reduces coupling. Preamplifier decoupling is preferred because it is effective not only with

the nearest neighbor but also with not the nearest-neighbor elements. All the above methods are called passive decoupling methods.

Transmit arrays also use passive decoupling methods except for preamplifier decoupling technique as transmit B_1 field requires circulating currents in the loops. In addition to passive decoupling techniques, transmit arrays also use active decoupling techniques [33]. Some of the active decoupling techniques include the transformation of the power amplifier to some form of a current source or other decoupling techniques like pre-correcting the digital waveforms to provide uncoupled field patterns.

Multi-Resonance

For some MR experiments, RF coil needs to resonate at two frequencies to study nuclei other than protons potentially giving access to information not available from proton imaging. Often the proton signal is used in preparatory phases like pulse calibration, shimming and slice localization. Most of the times, a proton image is used as an image for co-registration., For applications like decoupling experiments, a second B_1 field is used to enhance the signal on other nuclei using techniques like polarization transfer [34], nuclear Overhauser effect (NOE) or J-decoupling experiments [15]. Tuning for multi-resonance is similar to tuning a single resonant coil. Instead of using lumped elements like capacitors, complex circuits like traps or poles to realize variable impedance and active switches like diodes are used [35]. Any use of active switches or inserted poles reduces coil efficiency. In this work, we extended our novel model to determine multi-resonance conditions and design multi-resonant coils without utilization of active switches or inserted poles.

2.6 Chapter Summary

In this chapter, a brief glossary of terms related to magnetic resonance is presented. An overview of MR signal with its mathematical formulations is offered. The purpose of the chapter is to lay the foundations for MRI and RF coil basics that will be subsequently used to propose, develop, and validate a novel methodology for the design of RF coils using multiconductor transmission lines.

Chapter 3

Coil design using 2n-port model and Kronecker products of Fourier matrices

3.1 Introduction

In recent years, transmission line resonators have been widely used for MR applications [3]. This usage is due to the fact that in contrast to conventional shielded and unshielded birdcage coils, transmission line resonators are more efficient, easy to construct, and have a compact size. In general, a transmission line resonator can be a two conductor or a multiconductor system. The resonance that occurs in a transmission line resonator is a standing wave resonance, and its modes are standing wave resonant modes. Standing wave resonance for a distributed transmission line occurs due to the interference between a forward and a reverse traveling waves whose amplitudes are dependent on the terminations or discontinuities present at the line terminals [36]. To realize a practical and a useful design in terms of size, shape and field patterns, the electrical length of the transmission line is altered by deploying lumped elements at the ends. The method of altering the electrical length is called electrical lengthening/shortening, and such transmission lines are called "reduced-length" transmission line (RTL).

Two conductor transmission line resonators can be classified into different types [37]: a short-circuited $\lambda/2$ line, an open-circuited $\lambda/2$ line, a short-circuited $\lambda/4$ line. If a short is considered as an open-ended $\lambda/4$ transmission line and an open is considered as a short-ended $\lambda/4$ line, then the above classifications can be reduced to just two kinds: the electrically lengthened, short-circuited $\lambda/2$ line and the electrically shortened, open-circuited $\lambda/2$ line. If a passive lumped element is considered as a transmission line stub of certain electrical length, then any resonant transmission line terminated with lumped elements can be classified into one of the above two categories. The above-mentioned classification is a very interesting observation because it articulates the fact that the effective electrical length of any transmission line resonator is a multiple of $\lambda/2$.

Several methods were used to determine the values of lumped element terminations for reduced-length transmission line resonator. Lee et al. [38] computed the series resistance, shunt resistance, series inductance, and shunt capacitance of the transmission line using the per-unit-length quantities. After determining the per-unit-length quantities, the input admittance of the RTL is derived from the so-called ABCD matrix by letting the load at one port to be infinity[38]. The required terminating capacitance value is then computed by equating the susceptance of the input admittance equal to zero. Similarly, Zhang et al. [39] computed the input impedance of capacitively shunted microstrip. By applying the resonant condition of a parallel resonant circuit to the input impedance, the required value of the shunt tuning capacitor is calculated by the following equation

$$f_r = \frac{(2\pi f_r Z_0)^2 C_t C_{t1} - 1}{2\pi Z_0 (C_t + C_{t1})} \tan\left(\frac{2\pi l \sqrt{\varepsilon_{eff}}}{c} f_r\right) \quad (39)$$

here f_r is the frequency of resonance, Z_0 is the characteristic impedance of the transmission line. C_t and C_{tl} are the terminating capacitances, l is the length of the transmission line, c is the velocity of light, and ε_{eff} is the effective permittivity.

The approaches as mentioned above are for the two conductor transmission lines. Comparable approaches are adapted for multiconductor transmission lines. One of the primary application of multiconductor transmission line resonators is its use as a volume coil for MR imaging. Currently, two design approaches for volume coils using multiconductor transmission line structures exist [4], [40], [41].

The first approach uses a multiconductor transmission line (MTL) theoretical model based on a quasi-TEM approximation [4], [40]. The per-unit-length transmission line parameters are computed by 2D or 3D electromagnetic (EM) simulations. Using MTL theory, the reflection coefficient matrices Γ_S and Γ_L are computed at the source side and load sides, respectively. The input impedance at the source side for complex resonant frequencies can be computed numerically, as in [40], to find the required terminating impedances.

An alternative to computing the reflection coefficient matrix, the terminating impedances can also be found by applying chain parameter matrix terms as demonstrated in [4]. By clever mathematical manipulation of these terms, the source side input impedance is represented using the load impedance network and chain matrix parameters. The required terminating capacitance values are then computed by numerically solving the source side's Kirchhoff's voltage law (KVL) equation at resonance.

The second approach to CMTL design, described in [41], entails measuring the coupling coefficients between the elements experimentally and then using the obtained values to solve the KVL equation via iterative and numerical techniques. This approach assumes that at the required resonant frequency, the elements possess a co-sinusoidal current distribution. Both CMTL design approaches outlined above utilize iterative solutions which couple the termination values into the resonance equation nonlinearly.

Even though the above models places no restriction on the kind of terminations, they suggest and analyze using capacitive terminations only. While such an analysis is useful, it does not provide a complete depiction of resonant modes in MTL coils. This is particularly true in the case of inductive terminations where the axial field profile remains the same as that of capacitive termination, but longitudinal field profiles defer significantly. Ref [5] analyzes the issues of unequal terminations, but it limits its discussion only to current and field distributions. A detailed analysis of how unequal terminations affect the resonant frequency, resonant modes, currents, and field distributions are required.

In the approach presented in this thesis, a multiconductor transmission line is modeled as a multiport network. Resonant conditions are obtained by equating the determinant of its port admittance matrix to zero. A direct computation of eigenvalues is possible because of the circulant block nature of the port admittance matrix, and also the ability to be diagonalizable by a set of Fourier matrices. The proposed model can be used efficiently to design CMTL coils with unequal and off-diagonal terminations in load admittance matrix, and also for special cases of MTL coils like shielded birdcage coils, multi-channel volume strip arrays, and dual resonant coils.

This chapter is structured such that it explicitly discusses our research. After a brief introductory section, multiport representation of an MTL structure using a port admittance matrix, and numerous ways of calculating the admittance matrix are described. In the subsequent theoretical part, a short but essential block matrix algebra terminology is presented which is then followed by a mathematical proof for determining the resonant condition using an admittance matrix.

3.2 Theory

3.2.1 2n-port representation of MTL

An (n+1) conductor CMTL treated as a passive 2n-port network system as shown in Fig.4

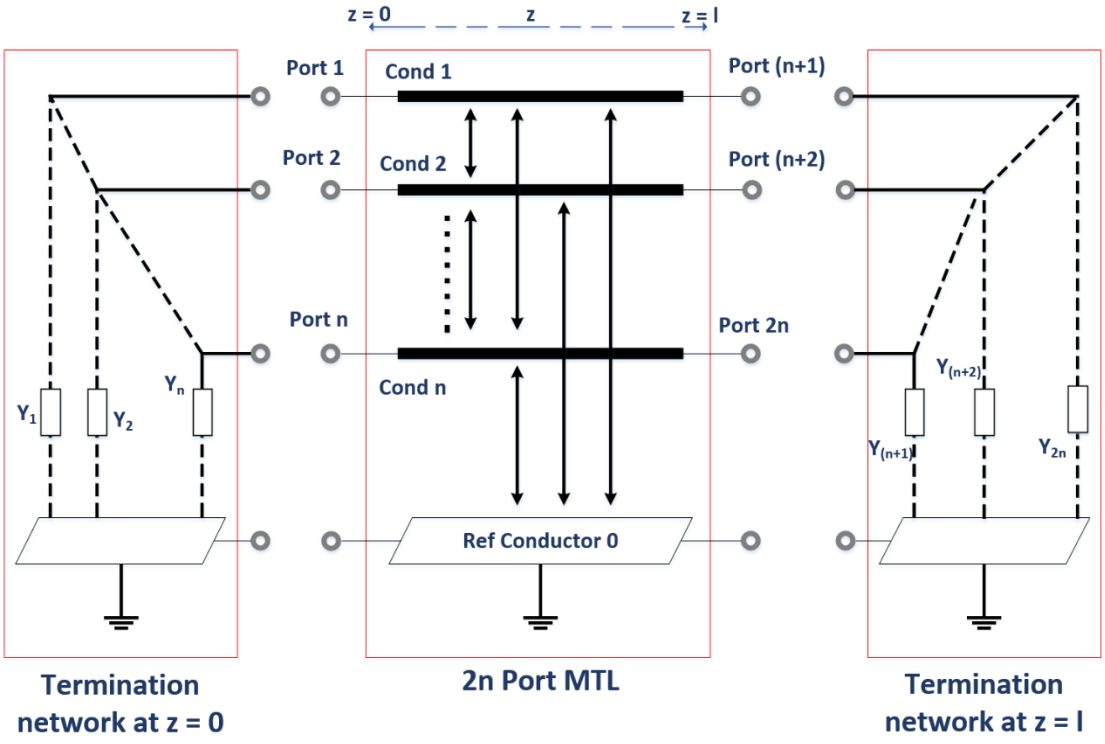

Fig.4: A 2n port representation of an (n+1) conductor,coupled multiconductor transmission line structure.

The CMTL can be represented with an open-circuit admittance parameter matrix $\hat{\mathbf{Y}}$ as [42]

$$\begin{bmatrix} \mathbf{I}(z) \\ -\mathbf{I}(0) \end{bmatrix} = \begin{bmatrix} \mathbf{Y_{00}} & \mathbf{Y_{0z}} \\ \mathbf{Y_{z0}} & \mathbf{Y_{zz}} \end{bmatrix} \begin{bmatrix} \mathbf{V}(z) \\ \mathbf{V}(0) \end{bmatrix} \tag{40}$$

where currents at both ends, **I**(z) and **I**(0), are directed into the 2n ports. The sub-matrices $\mathbf{Y_{00}}$ and $\mathbf{Y_{zz}}$ of $\widehat{\mathbf{Y}}$ for a (n+1) CMTL of length *z* represent a *n* x *n* element driving point admittance matrix for n-ports at z = 0 and z = l, respectively. Similarly, matrices $\mathbf{Y_{0z}}$ and $\mathbf{Y_{z0}}$ represent the transfer admittance matrix at z = 0 and z = l respectively.

If voltages and currents on 2n ports are represented by vectors **V**(p) and **I**(p), where p = 0,1,…2n is the port index, then in port space, by invoking Kirchhoff's equations, a CMTL terminated with load admittance at both ends can be represented as

$$\mathbf{I}(p) \quad = \quad (\widehat{\mathbf{Y}} + \mathbf{Y_L})\mathbf{V}(p) \tag{41}$$

where $\mathbf{Y_L}$ is called the admittance matrix of the terminations, which is of size 2n x 2n.

3.2.2 Admittance matrix calculation

There are numerous ways of computing the admittance matrix $(\widehat{\mathbf{Y}})$ at the ports. The admittance matrix can be theoretically derived, experimentally determined, or numerically computed. A complete 3D full wave EM simulation can be performed by using commercial EM simulators such as HFSS or CST Studio to determine the admittance matrix. Such simulations require expensive software and computing resources.

3.2.3 Experimental determination of admittance matrix

Experimental determination of the admittance matrix can be performed by the technique described in [11]. A multiconductor transmission line structure is characterized by its S-parameters which are measured using a network analyzer. Then using the standard S-parameter to Y-parameter conversion, the admittance matrix is computed. The experimental approach becomes a useful tool when electromagnetic simulation tools are unavailable. However, lack of flexibility in performing optimization of structure because of availability of only a single dataset limits the usage of the above technique.

3.2.4 Admittance matrix calculation using per-unit values

In this section, the admittance matrix calculation is described by using chain parameters and MTL equations. Per-unit length transmission line parameters are computed by relying on an in-house developed 2D BEM code [4]. The advantage of a per-unit-length technique is that the chain parameter matrix can be computed for different lengths and subsequently used to compute current and voltage distributions along the length of the coil.

The time-domain MTL equations for an (n+1) conductor transmission line are given in matrix form by the following equations as

$$\frac{\partial}{\partial z}\boldsymbol{V}(z,t) = -\mathbf{R}\boldsymbol{I}(z,t) - \mathbf{L}\frac{\partial}{\partial t}\boldsymbol{I}(z,t) \tag{42}$$

$$\frac{\partial}{\partial z}\boldsymbol{I}(z,t) = -\mathbf{G}\boldsymbol{V}(z,t) - \mathbf{C}\frac{\partial}{\partial t}\boldsymbol{V}(z,t) \tag{43}$$

where **R, L, G,** and **C** are per-unit-length resistance, inductance, conductance and capacitance matrices of size *n* x *n* respectively. Independent variables *z* and *t* represent the position along the line and time,respectively.

The time-domain MTL equations rewritten in the frequency domain for sinusoidal and steady state excitation are expressed as

$$\frac{d}{dz}\begin{bmatrix}\boldsymbol{V}(\mathrm{z})\\ \boldsymbol{I}(\mathrm{z})\end{bmatrix} = \begin{bmatrix}\mathbf{0} & -\mathbf{Z}\\ -\mathbf{Y} & \mathbf{0}\end{bmatrix}\begin{bmatrix}\boldsymbol{V}(z)\\ \boldsymbol{I}(z)\end{bmatrix} \tag{44}$$

where $\mathbf{Z} = \mathbf{R} + j\omega\mathbf{L}$ and $\mathbf{Y} = \mathbf{G} + j\omega\mathbf{C}$ are the per-unit impedance, and admittance matrices, and ω is the angular frequency.

The above system has a solution

$$\begin{bmatrix}\mathbf{V}(\mathbf{z_2})\\ \mathbf{I}(\mathbf{z_2})\end{bmatrix} = \boldsymbol{\Phi}(\mathbf{z_2}-\mathbf{z_1})\begin{bmatrix}\mathbf{V}(\mathbf{z_1})\\ \mathbf{I}(\mathbf{z_1})\end{bmatrix} \tag{45}$$

Here $\boldsymbol{\Phi}(z)$ is called the chain parameter matrix of size 2n x 2n, and is defined in terms of the matrix exponential as

$$\boldsymbol{\Phi}(z) = e^{z\mathbf{A}} \quad ; \quad \mathbf{A} = \begin{bmatrix} \mathbf{0} & -\mathbf{Z} \\ -\mathbf{Y} & \mathbf{0} \end{bmatrix} \tag{46}$$

There are numerous ways to compute the chain parameter matrix [43]. The "expm" function in MATLAB [44] which uses the Padé approximation with scaling and squaring can be used as one solution method. The phasor voltages and currents at the two ends of the line of length z can be related through a chain parameter matrix as

$$\begin{bmatrix} \mathbf{V}(\mathbf{z_2}) \\ \mathbf{I}(\mathbf{z_2}) \end{bmatrix} = \begin{bmatrix} \boldsymbol{\Phi}_{\mathbf{11}}(\mathrm{z}) & \boldsymbol{\Phi}_{\mathbf{12}}(\mathrm{z}) \\ \boldsymbol{\Phi}_{\mathbf{21}}(\mathrm{z}) & \boldsymbol{\Phi}_{\mathbf{22}}(\mathrm{z}) \end{bmatrix} \begin{bmatrix} \mathbf{V}(0) \\ \mathbf{I}(0) \end{bmatrix} \tag{47}$$

here $\boldsymbol{\Phi}_{\mathbf{ij}}$ is a matrix of size n x n.

The relation between terms of the chain parameter matrix and the admittance parameter matrix is given by the following equations [42]:

$$\mathbf{Y_{11}} = -\boldsymbol{\Phi}_{\mathbf{12}}^{-\mathbf{1}}\boldsymbol{\Phi}_{\mathbf{11}} \tag{48}$$

$$\mathbf{Y_{12}} = -\boldsymbol{\Phi}_{\mathbf{12}}^{-\mathbf{1}} \tag{49}$$

$$\mathbf{Y_{21}} = -\boldsymbol{\Phi}_{\mathbf{21}}^{-\mathbf{1}} \tag{50}$$

$$\mathbf{Y_{22}} = -\boldsymbol{\Phi}_{\mathbf{12}}^{-\mathbf{1}}\boldsymbol{\Phi}_{\mathbf{11}} \tag{51}$$

It should be noted that for an (n+1) conductor CMTL that is being represented as a 2n–port network, the sub-matrices $\mathbf{Y_{11}}$, $\mathbf{Y_{22}}$, $\mathbf{Y_{12}}$, and $\mathbf{Y_{21}}$ are all of size n x n and the overall admittance matrix $\mathbf{Y}$ is a block matrix of size 2n x 2n. To exploit the advantages of representing an MTL structure using port admittance matrix, it is essential to understand the terminology and definitions of block matrix algebra. The subsequent section presents essential block matrix algebra theory.

3.2.5 Block matrix algebra

Circulant matrix

A circulant matrix is a special kind of Toeplitz matrix, where each row vector is rotated one element to the right relative to the preceding row vector [45] as shown

$$\boldsymbol{C} = \begin{bmatrix} c_0 & c_1 & \cdots & c_{n-2} & c_{n-1} \\ c_{n-1} & c_0 & \ddots & c_{n-3} & c_{n-2} \\ \vdots & \ddots & \ddots & \ddots & \vdots \\ c_2 & c_3 & \ddots & c_0 & c_1 \\ c_1 & c_{n-2} & \cdots & c_{n-1} & c_0 \end{bmatrix} \tag{52}$$

A circulant matrix can be fully specified by a vector represented in the first column of $\boldsymbol{C}$. The remaining columns are each cyclic permutations of the vector with an offset equal to the column index. Circulant matrices exhibit the special property of fixed eigenvectors. The normalized eigenvectors of a circulant matrix are given by

$$\begin{bmatrix} \mathbf{V}(\mathbf{z_2}) \\ \mathbf{I}(\mathbf{z_2}) \end{bmatrix} = \frac{1}{\sqrt{n}}\left(1, \omega_p, \omega_p^2, \cdots, \omega_p^{n-1}\right)^T, \quad p = 0,1,\cdots,n-1 \tag{53}$$

Here $\omega_p = \mathrm{e}^{\left(2\pi p j/\mathrm{n}\right)}$ are the p[th] root of unity amongst n-roots and $j = \sqrt{-1}$ is the imaginary number.

The corresponding eigenvalues are given by

$$\lambda_p = c_0 + c_1\omega_p + c_2\omega_p^2 + \cdots + c_{n-1}\omega_p^{n-1}, \quad \mathrm{p} = 0,1,\cdots,n-1, \tag{54}$$

The eigenvectors of a circulant matrix form a Fourier matrix.

Fourier matrix

Fourier matrix $\mathbf{F_n}$ is a square matrix of size n x n, with entries given by

$$F_{p,\mathrm{q}} = \omega^{(\mathrm{p}-1)(\mathrm{q}-1)} \;\forall\; p = 0,1,\cdots,n-1;\; q = 0,1,\cdots,n-1; \tag{55}$$

$$\omega = e^{\left(2\pi j/n\right)} \text{ and } j = \sqrt{-1}$$

$$\boldsymbol{F_n} = \frac{1}{\sqrt{n}} \begin{bmatrix} 1 & 1 & \cdots & 1 & 1 \\ 1 & \omega^{1} & \ddots & \omega^{(n-2)} & \omega^{(n-1)} \\ \vdots & \ddots & \ddots & \ddots & \vdots \\ 1 & \omega^{(n-2)} & \ddots & \omega^{(n-2)(n-2)} & \omega^{(n-2)(n-1)} \\ 1 & \omega^{(n-1)} & \cdots & \omega^{(n-2)(n-1)} & \omega^{(n-1)(n-1)} \end{bmatrix} \quad (56)$$

Some of the properties of a Fourier matrix are

1. $\mathbf{F} = \mathbf{F}^{\mathbf{T}}$, where ^{T} is the transpose of a matrix
2. $\mathbf{F}^{*} = \overline{\boldsymbol{F}}$, where * is the complex-conjugate of a matrix and $\bar{}$ is the conjugate of the matrix
3. $\mathbf{F}^{*}\mathbf{F} = \mathbf{F}\,\mathbf{F}^{*} = \mathbf{I}$ or $\mathbf{F}^{-1} = \mathbf{F}^{*}$
4. A Fourier matrix is also known as the discrete Fourier transform, and it is the normalized eigenvector matrix of a circulant matrix

Block matrix

A block matrix is a matrix which is subdivided into rectangular blocks of element sections called blocks or sub-matrices. Subscripts can label each submatrix or block, and original matrix can be displayed with sub-matrices or blocks as its elements.

Kronecker product operator

The Kronecker product (direct matrix product) of a $m \times n$ matrix **A** and a $p \times q$ matrix **B** is the $(m\,p) \times (n\,q)$ matrix is given by $\mathbf{A} \otimes \mathbf{B}$ in block form as

$$\mathbf{A} \otimes \mathbf{B} = \begin{bmatrix} a_{11}\mathbf{B} & \cdots & a_{n1}\mathbf{B} \\ \vdots & \ddots & \vdots \\ a_{1n}\mathbf{B} & \cdots & a_{nn}\mathbf{B} \end{bmatrix} \quad (57)$$

where $a_{s,t}$ are the elements of matrix **A**

Some of the important properties of Kronecker product operator are

1. $(\mathbf{A}+\mathbf{B})\otimes\mathbf{C})=(\mathbf{A}\otimes\mathbf{C})+(\mathbf{B}\otimes\mathbf{C})$
2. $(\mathbf{A}\otimes\mathbf{B})\otimes\mathbf{C})=\mathbf{A}\otimes(\mathbf{B}\otimes\mathbf{C})$

Block circulant matrix

A matrix is called block circulant if each row of blocks is a periodic shift of its previous row of blocks. A block circulant matrix is represented as $BC_{m,n}$. Block circulant matrix A has the following property

$$diag(\boldsymbol{M_1}, \boldsymbol{M_2}, \dots, \boldsymbol{M_n}) \quad = \quad (\mathbf{F_m}\otimes\mathbf{F_n})\mathbf{A}(\mathbf{F_m}\otimes\mathbf{F_n})^* \tag{58}$$

where the $\mathbf{M_k}$ are arbitrary square matrices of order n.

Circulant block matrix

A matrix is called circulant block matrix if every block is a circulant matrix and is represented by $CB_{m,n}$. Circulant block matrix exhibits the following relation

$$(\boldsymbol{\theta}_{s,r}) \quad = \quad (\mathbf{F_m}\otimes\mathbf{F_n})\mathbf{A}(\mathbf{F_m}\otimes\mathbf{F_n})^* \tag{59}$$

where the $\boldsymbol{\theta}_{s,r}$ are arbitrary diagonal matrices of order n

Block circulant with circulant block

A matrix is called block circulant with circulant blocks (BCCB) if each row of blocks is a periodic shift of its previous row of blocks, and every block is a circulant matrix. A *BCCB* is characterized by order or type and level. A BCCB matrix of order 'mnp' is of type (m,n,p) if it has been divided into m x m blocks, each of which is divided into n x n blocks, each of which is of order p. The integers are ordered from 'outside' to 'inside.' Similarly, the number of variables in type represent the level.

1. A circulant of level 1 is an ordinary circulant matrix
2. A circulant of level 2 is a block circulant matrix whose blocks are circulant

A circulant of level q>2 is a block circulant matrix whose blocks are level q-1 circulant metrics

A Level 2 *block circulant with circulant blocks* matrix $BCCB_{m,n}$ of order m and n is by definition an m x m sized circulant matrix, with each element in that matrix representing a circulant block of size n x n [46]. A $BCCB_{m,n}$ matrix **A** can be converted into a diagonal matrix **M** using the following mathematical operation:

$$diag(\boldsymbol{M_1}, \boldsymbol{M_2}, \dots, \boldsymbol{M_n}) \quad = \quad (\mathbf{F_m} \otimes \mathbf{F_n})\mathbf{A}(\mathbf{F_m} \otimes \mathbf{F_n})^* \tag{60}$$

Here $\otimes$ represents the Kronecker product operation between two vectors, * represents the complex conjugate operation, and $\mathbf{F_m}$ and $\mathbf{F_n}$ are Fourier matrices of order m and n respectively.

In general, a level q $BCCB_{m,n}$ matrix **A** can be converted into a diagonal matrix **M** using the following mathematical operation:

$$diag(\boldsymbol{M_1}, \boldsymbol{M_2}, \dots, \boldsymbol{M_n}) \quad = \quad (\mathbf{F_m} \otimes \mathbf{F_n})\left(\mathbf{F_m} \otimes \mathbf{F_n} \otimes \cdots \otimes \mathbf{F_q}\right) \mathbf{A} \, (\mathbf{F_m} \otimes \mathbf{F_n} \otimes \cdots \otimes \mathbf{F_q})^* \tag{61}$$

3.3 Resonant conditions using admittance matrix

In this section, we present the background that allows us to determine the resonant conditions for a reduced transmission line resonator. At first, mathematical proof is presented for a two conductor transmission line structure. Governing equations for two-conductor transmission lines are then extended for multiconductor transmission lines by using general matrix theory.

The transfer matrix (ABCD) representation of a shunt capacitor terminated transmission line as shown in Fig.5 is given by the following equation:

$$\begin{bmatrix} A & B \\ C & D \end{bmatrix} = \begin{bmatrix} 1 & 0 \\ j\omega C & 1 \end{bmatrix} \begin{bmatrix} a & b \\ c & d \end{bmatrix} \begin{bmatrix} 1 & 0 \\ j\omega C & 1 \end{bmatrix} \tag{62}$$

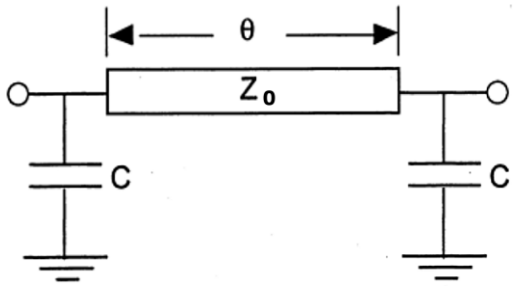

Fig.5: A shunt capacitor terminated reduced length transmission line with electrical length θ.

where $j\omega$C is the admittance of termination capacitor and *abcd* are the transfer matrix coefficients of a transmission line and are discussed further below. Following term-by-term multiplication, we arrive at

$$\begin{bmatrix} \mathrm{A} & \mathrm{B} \\ \mathrm{C} & D \end{bmatrix} = \begin{bmatrix} 1 & 0 \\ j\omega\mathrm{C} & 1 \end{bmatrix} \begin{bmatrix} a & b \\ c & d \end{bmatrix} \begin{bmatrix} 1 & 0 \\ j\omega\mathrm{C} & 1 \end{bmatrix} \tag{63}$$

$$\begin{bmatrix} \mathrm{A} & \mathrm{B} \\ \mathrm{C} & D \end{bmatrix} = \begin{bmatrix} a + (b \cdot j\omega C) & b \\ (\,(a \cdot j\omega C) + c) + \big((b \cdot j\omega C) + d\big) \cdot j\omega C\,) & (b \cdot j\omega C) + d \end{bmatrix} \tag{64}$$

$$\begin{bmatrix} \mathrm{A} & \mathrm{B} \\ \mathrm{C} & D \end{bmatrix} = \begin{bmatrix} a + (b \cdot j\omega C) & b \\ (a \cdot j\omega C) + (d \cdot j\omega C) + c - b\omega^2 C^2\,) & (b \cdot j\omega C) + d \end{bmatrix} \tag{65}$$

Using ABCD to Y-parameters transformation;

$$\begin{bmatrix} \mathrm{Y}^{full}{}_{11} & \mathrm{Y}^{full}{}_{12} \\ \mathrm{Y}^{full}{}_{21} & \mathrm{Y}^{full}{}_{22} \end{bmatrix}$$

$$= \frac{1}{b}\begin{bmatrix} a + (b \cdot j\omega\mathrm{C}) & -[\,(a + b \cdot j\omega\mathrm{C})\,(b \cdot j\omega\mathrm{C} + d) - b \cdot (a \cdot j\omega\mathrm{C} + d \cdot j\omega\mathrm{C} + c - b\omega^2\mathrm{C}^2\,))] \\ -1 & (b \cdot j\omega\mathrm{C}) + d \end{bmatrix}$$

For a uniform transmission line $a = d$, and the above equation reduces to

$$\begin{bmatrix} \mathrm{Y}^{full}{}_{11} & \mathrm{Y}^{full}{}_{12} \\ \mathrm{Y}^{full}{}_{21} & \mathrm{Y}^{full}{}_{22} \end{bmatrix} = \frac{1}{b}\begin{bmatrix} a + (b \cdot j\omega\mathrm{C}) & -[\,a^2 - bc] \\ -1 & (b \cdot j\omega\mathrm{C}) + a \end{bmatrix} \tag{66}$$

Solving the characteristic equation by equating its determinant to zero.

$$(a + b \cdot j\omega \mathrm{C})\,(b \cdot j\omega \mathrm{C} + a) - (a^2 - bc) = 0 \tag{67}$$

$$2 \cdot a \cdot b \cdot j\omega \cdot \mathrm{C} - b \cdot \omega^2 \cdot \mathrm{C}^2 + b \cdot c = 0 \tag{68}$$

$$2 \cdot a \cdot j\omega \mathrm{C} = b \cdot \omega^2 \mathrm{C}^2 - c \tag{69}$$

For a uniform transmission line,

$$a = \cosh \gamma l \overset{if\ lossless}{\Longleftrightarrow} a = \cos \beta l = d \tag{70}$$

$$c = \frac{\sinh \gamma l}{Z_0} \overset{if\ lossless}{\Longleftrightarrow} c = \frac{j \sin \beta l}{Z_0} \tag{71}$$

Here $\gamma = \alpha + j\beta$ is the complex propagation constant, α is the attenuation constant, β is the phase constant and Z_0 is the characteristic impedance of a transmission line

Then equation (69) reduces to :

$$2j\omega \mathrm{C} \cosh \gamma l = \sinh \gamma l \left[\omega^2 \mathrm{C}^2 Z_0 - \frac{1}{Z_0}\right] \tag{72}$$

$$2j\omega \mathrm{C}\, Z_0 \cosh \gamma l = \sinh \gamma l \left[\omega^2 \mathrm{C}^2 {Z_0}^2 - 1\right] \tag{73}$$

$$\omega = \frac{\left[\omega^2 \mathrm{C}^2 {Z_0}^2 - 1\right]}{2j\mathrm{C}\, Z_0} \tanh \gamma l \tag{74}$$

For a lossless line, we see that

$$\omega = \frac{\left[\omega^2 \mathrm{C}^2 {Z_0}^2 - 1\right]}{2\mathrm{C}\, Z_0} \tan \beta l \tag{75}$$

It should be observed that equation (75) and equation (39) are identical if C_{t1}, C_{t2} are considered equal to C, ω is replaced with $2\pi f_r$, and $\beta = \frac{2\pi\sqrt{\varepsilon_{eff}}}{c} f_r$.

From the above mathematical derivation, it can be deduced that the solution of the characteristic equation for the admittance matrix provides the conditions for resonance. The stated proof can be easily extended

from twin conductor configuration to multiconductor configuration by replacing the transfer matrix coefficients with chain parameter matrices of a multiconductor structure.

3.4 Design of single resonant MTL coil

An MTL structure composed of microstrip lines can be tuned to a single frequency by terminating the microstrips with capacitive loads [4]. A similar MTL structure made with co-axial conductors can also be converted into a classical single tuned *TEM resonator* by terminating its coaxial conductors to the shield, using end loads (realized using either open or short-circuited coaxial transmission lines). If an MTL is symmetrical, cyclic structure (which is a most general case for single resonant volume coils), then $\mathbf{Y_{11}}$, $\mathbf{Y_{22}}$, $\mathbf{Y_{12}}$, and $\mathbf{Y_{21}}$ are circulant matrices. However $\widehat{\mathbf{Y}}$ is not a circulant matrix, but it is a matrix of circulant blocks. Using block matrix notation, $\widehat{\mathbf{Y}}$ is called a *block circulant with circulant blocks* matrix $BCCB_{m,n}$, where m = 2 [45].

In mode space, the voltages and currents regarding basic modes are defined as $V_s(k)$ and $I_s(k)$, where k = 0,1, ...2n is the basic mode index, and subscript s represent a model quantity, then by definition, a CMTL in mode space is written as

$$\mathbf{I_s}(k) \quad = \quad (\mathbf{M} + \mathbf{Y_{sL}})\mathbf{V_s}(k) \tag{76}$$

where

$$\widehat{\mathbf{Y}} = (\mathbf{F_m} \otimes \mathbf{F_n})^{*}\mathbf{M}(\mathbf{F_m} \otimes \mathbf{F_n}) \text{ and } \mathbf{Y_L} = (\mathbf{F_m} \otimes \mathbf{F_n})^{*}\mathbf{Y_{sL}}(\mathbf{F_m} \otimes \mathbf{F_n}) \tag{77}$$

The following equations give the relationship between mode space and port space quantities:

$$\mathbf{I_s}(k) \quad = \quad (\mathbf{F_m} \otimes \mathbf{F_n})\,\mathbf{V}(p) \tag{78}$$

$$\mathbf{I_s}(k) \quad = \quad (\mathbf{F_m} \otimes \mathbf{F_n})\,\mathbf{I}(p) \tag{79}$$

Mode space description is more favorable because the normal mode frequencies ω can be found simply by solving $det\,(\mathbf{M} + \mathbf{Y_{sL}}) = 0$ [47], as both $\mathbf{M}$ and $\mathbf{Y_{sL}}$ are functions of ω.

To keep the brevity of terminology, the method of solving *det* (**M** + $\mathbf{Y_{sL}}$) to determine the resonant conditions is from now on called as a 2n-port model.

3.4.1 Equal admittance terminations

Consider the case where the terminating admittances on all terminals are equal and are defined as Y_T. Now $\mathbf{Y_{sL}}$ becomes a diagonal matrix with Y_T as its diagonal elements. For a diagonal matrix, the determinant can be calculated by the product of the eigenvalues:

$$Det(\mathbf{M} + \mathbf{Y_{sL}}) = \prod_{i=1}^{2n} [M_{ii} + Y_T] \quad (80)$$

The k^{th} eigenvector of any *block circulant with circulant block* matrix $BCCB_{m,n}$ can be given by the k^{th} row vector of its diagonalizing matrix $(\mathbf{F_m} \otimes \mathbf{F_n})$. The required terminating capacitance value is determined by assuming the required k^{th} mode frequency and equating the corresponding k^{th} eigenvalue to zero. In this case, the k^{th} eigenvalue is simply the k^{th} term under the product operator in equation (80). For a case where the termination value is known, the k^{th} mode frequency can be computed by sweeping the frequency and finding a value where the k^{th} eigenvalue equals to zero.

3.4.2 Unequal admittance terminations

For a case where the terminating admittance for all terminals at end z = 0 is $Y_{T1,}$ and at end z = l is Y_{T2}, then $\mathbf{Y_{mL}}$ becomes a 2 X 2 element matrix with each element representing a diagonal matrix. The value of the diagonal elements of the main diagonal blocks will be $\frac{1}{2}(Y_{T1} + Y_{T2})$ and of the off-diagonal blocks will be $\frac{1}{2}(Y_{T1} - Y_{T2})$

The determinant of a block matrix **X** of the form $\begin{bmatrix} \mathbf{A} & \mathbf{B} \\ \mathbf{C} & \mathbf{D} \end{bmatrix}$ can be given as

$$det(\mathbf{X}) = det(\mathbf{D})det(\mathbf{A}\text{-}\mathbf{B}\mathbf{D}^{-1}\mathbf{C}) \quad (81)$$

If **CD** = **DC**, then

$$det(\mathbf{X}) \quad = \quad det(\text{AD-BC}) \tag{82}$$

Provided **A, B, C** and **D** are diagonal matrices, then

$$det(\mathbf{X}) \quad = \quad \prod_{i=1}^{n} [a_{ii}d_{ii} - b_{ii}c_{ii}] \tag{83}$$

using the identity in equation (83) it follows

$$Det(\mathbf{M} + \mathbf{Y_{sL}}) \quad = \quad \prod_{i=1}^{n} \left[\left(\left[\mathrm{M_{i,i}} + \frac{1}{2} (\mathrm{Y_{T1}} + \mathrm{Y_{T2}}) \right] \left[\mathrm{M_{n+i,n+i}} + \frac{1}{2} (\mathrm{Y_{T1}} + \mathrm{Y_{T2}}) \right] - \left[\frac{1}{2} (\mathrm{Y_{T1}} - \mathrm{Y_{T2}}) \right]^2 \right) \right] \tag{84}$$

The k^{th} mode frequency can be computed by sweeping the frequency and equating the k^{th} eigenvalue to zero for known Y_{T1} and Y_{T2}. If Y_{T1} and Y_{T2} are unknown, then by assuming a linear relationship between them, the required terminating values can be determined numerically by equating the k^{th} term in equation (84) to zero.

3.5 Design of Dual tuned, Dual-element coil

As a demonstration of the utility of the proposed theory, a new dual tuned, dual-element (DTDE) surface coil is presented. The DTDE coil consists of 2 elements, and a shield surrounding the elements. Fig.6 shows the schematic representation of the coil. Each element is terminated to the shield by lumped components as shown.

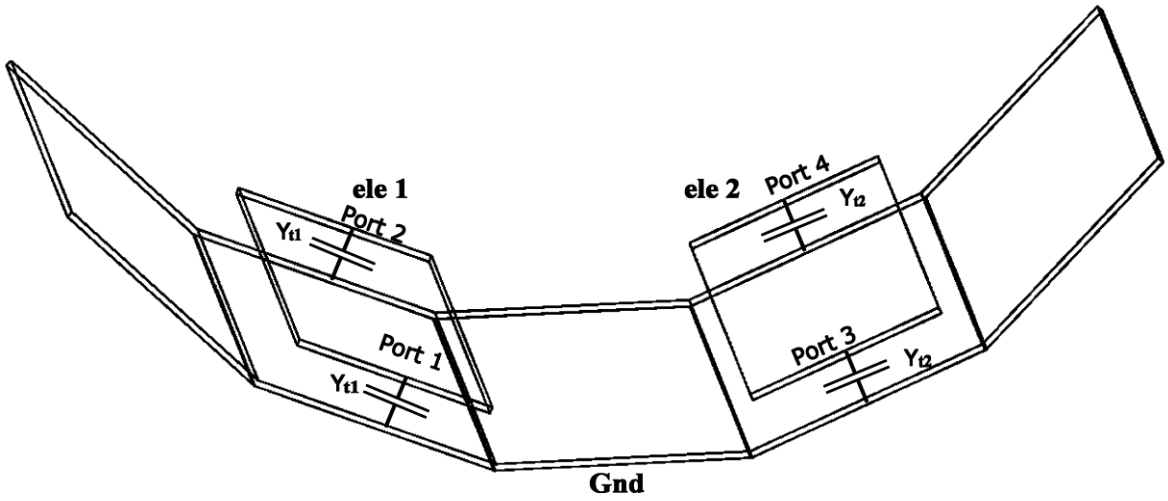

Fig.6: Schematic of the proposed dual tuned dual element coil. Both the elements are terminated with capacitors.

The port admittance matrix of the DTDE coil with terminations can be written as follows

$$\mathbf{Y} = \begin{bmatrix} \begin{vmatrix} Y_{11} & Y_{12} \\ Y_{21} & Y_{22} \end{vmatrix} & \begin{vmatrix} Y_{13} & Y_{14} \\ Y_{23} & Y_{24} \end{vmatrix} \\ \begin{vmatrix} Y_{31} & Y_{32} \\ Y_{41} & Y_{42} \end{vmatrix} & \begin{vmatrix} Y_{33} & Y_{34} \\ Y_{43} & Y_{44} \end{vmatrix} \end{bmatrix} + \begin{bmatrix} Y_{T1} & 0 & 0 & 0 \\ 0 & Y_{T1} & 0 & 0 \\ 0 & 0 & Y_{T2} & 0 \\ 0 & 0 & 0 & Y_{T2} \end{bmatrix} \tag{85}$$

If the elements are identical and symmetrical, then the port admittance matrix transforms into a 2 X 2 circulant block matrix with each block being a 2 X 2 circulant matrix. The new transformed port admittance matrix is given by equation (86)

$$\mathbf{Y} = \begin{bmatrix} \begin{vmatrix} Y_{11} & Y_{12} \\ Y_{12} & Y_{11} \end{vmatrix} & \begin{vmatrix} Y_{13} & Y_{14} \\ Y_{14} & Y_{13} \end{vmatrix} \\ \begin{vmatrix} Y_{13} & Y_{14} \\ Y_{14} & Y_{13} \end{vmatrix} & \begin{vmatrix} Y_{11} & Y_{12} \\ Y_{12} & Y_{11} \end{vmatrix} \end{bmatrix} + \begin{bmatrix} Y_{T1} & 0 & 0 & 0 \\ 0 & Y_{T1} & 0 & 0 \\ 0 & 0 & Y_{T2} & 0 \\ 0 & 0 & 0 & Y_{T2} \end{bmatrix} \tag{86}$$

A 2 X 2 circulant block matrix with each block being a 2 X 2 circulant matrix can be diagonalized by $(\mathbf{F_2} \otimes \mathbf{F_2})$ and its conjugate as follows:

$$\mathbf{M} + \mathbf{Y_{sL}} = \begin{bmatrix} M_{11} & 0 & 0 & 0 \\ 0 & M_{22} & 0 & 0 \\ 0 & 0 & M_{33} & 0 \\ 0 & 0 & 0 & M_{44} \end{bmatrix} + \frac{1}{2} \begin{bmatrix} (Y_{T1} + Y_{T2}) & 0 & (Y_{T1} - Y_{T2}) & 0 \\ 0 & (Y_{T1} + Y_{T2}) & 0 & (Y_{T1} - Y_{T2}) \\ (Y_{T1} - Y_{T2}) & 0 & (Y_{T1} + Y_{T2}) & 0 \\ 0 & (Y_{T1} - Y_{T2}) & 0 & (Y_{T1} + Y_{T2}) \end{bmatrix} \tag{87}$$

Elements in matrix $(\mathbf{M} + \mathbf{Y_{sL}})$ are frequency dependent and the determinant of $(\mathbf{M} + \mathbf{Y_{sL}})$ can be written as

$$Det(\mathbf{M}(\omega) + \mathbf{Y_{sL}}(\omega)) =$$

$$\prod_{i=1}^{2} \left[M_{i,i}(\omega) + \frac{1}{2}(Y_{T1}(\omega) + Y_{T2}(\omega)) \right] \left[M_{2+i,2+i}(\omega) + \frac{1}{2}(Y_{T1}(\omega) + Y_{T2}(\omega)) \right] - \left[\frac{1}{2}(Y_{T1}(\omega) - Y_{T2}(\omega)) \right]^2 \tag{88}$$

To determine the resonant conditions for the DTDE coil at multiple resonances, the determinant of $(\mathbf{M} + \mathbf{Y_{sL}})$ is written for both frequencies ω_{LO} and ω_{HI}. The determinant equations are then solved numerically to determine the required termination values.

Since the elements of $(\mathbf{F_2} \otimes \mathbf{F_2})$ form the eigenvectors (which represent port currents), it is interesting to observe their characteristics.

$$(\mathbf{F_2} \otimes \mathbf{F_2}) = \begin{bmatrix} 0.5 & 0.5 & 0.5 & 0.5 \\ 0.5 & -0.5 & 0.5 & -0.5 \\ 0.5 & 0.5 & -0.5 & -0.5 \\ 0.5 & -0.5 & -0.5 & 0.5 \end{bmatrix} \tag{89}$$

The notation adopted for port currents is such that all currents are flowing into the coil. Thus the preferred port current distribution is given by a row 2 vector of $(\mathbf{F_2} \otimes \mathbf{F_2})$. By directly substituting $i = 2$ in equation

(88) reduces the determinant into a quadratic form, thereby reducing the complexity for the numerical solver.

3.5.1 Calculation of current distribution along the length of the coil

Once the termination admittances are calculated, then by using the KVL equation, the current at each port is computed for a known excitation voltage. By combining the chain parameter matrix, port currents and port voltages on ports located at one end of the CMTL (preferably $z = 0$), the current distribution along the length of the coil can be calculated by the equation [4]:

$$\mathbf{I}(z) \quad = \quad \mathbf{\Phi_{21}}(\mathrm{z}) \cdot \mathbf{V}(0) + \mathbf{\Phi_{22}}(\mathrm{z}) \cdot \mathbf{I}(0) \tag{90}$$

The field distribution can be computed from the current distribution by using the standard form of Biot-Savart's law.

3.6 Results

3.6.1 Single resonant MTL coil

To validate the proposed 2n-port model, simulated results were analyzed and compared with published data for two different volume coils as described in [4]. The first coil to be analyzed, called "small coil," has an inner diameter of 7.25 cm, an outer diameter of 10.5 cm, and is 15.25 cm long. The small coil has 12 elements made with 6.4 mm wide copper strips. The second coil called "big coil." It has an inner diameter of 13.33 cm, an outer diameter of 17.78 cm, is 15.25 cm long, and has 12 elements made of 21.6 mm wide copper strips. The small coil was tuned to two different frequencies of 200MHz and 300MHz and the big coil to 200MHz. Table 2 shows the mechanical dimensions of both coils.

Table 2: Single resonant MTL volume coil parameters.

	Small Coil	Big Coil
Length (strips and former)	152.4 mm	152.4 mm
Outer diameter	105 mm	177.8 mm
Inner Diameter	72.5 mm	133.3 mm
Number of elements	12	12
Strip Width	6.4 mm	21.6 mm
Copper Thickness	1.5 mil	1.5 mil
Former Wall Thickness	2.8mm	2.8 mm

Per-unit values simulation

The per-unit values L and C for both the small and the big coils are computed using the electrostatic solver of MAXWELL SV [48]. MAXWELL SV is an electromagnetic (EM) simulation software package that uses the finite element method (FEM) analysis to simulate and solve 2D EM field problems. The per-unit capacitance values are computed by integration of normal component of the E-field as described in [4].

The small coil is discretized into a finite element mesh. The density of the mesh determines the accuracy of the solution. An adaptive meshing is used to improve the quality of mesh. Meshing solution is obtained with an error less than 0.01%. Adaptive refinement of 5% per pass with a minimum of ten passes is used, and the solution is allowed to converge to a minimum of two passes. For the small coil, the solution converged in 14.42 sec of CPU time with 55136 mesh elements on a Dell Optiplex 7010 running an i7-3770 at 3.4 GHz with 8 GB of RAM. Similarly, for the big coil, it took 62534 mesh elements and 16.9 sec of CPU time on the same PC for the solution to converge.

3.6.2 Port admittance matrix calculation

Port admittance simulation

After the per unit length values are obtained, the chain parameter matrices are computed for a given coil length as described in the theory section. The open circuit admittance matrix is calculated at the required frequency using equations (48)-(51).

Full-wave 3D EM simulations were also performed using the HFSS-driven terminal solver [49] to generate the open-circuit admittance matrix. Similar to MAXWELL SV, the 3D EM simulation software package HFSS uses the finite element method (FEM) analysis to simulate and solve 3D EM field problems.

A realistic 3-D EM model of the small coil with all its elements and housing is modeled using precise dimensions and material properties. Each coil element terminations were substituted with 50 ohm lumped ports. The substitution yielded a total number of ports as high as 24. As with MAXWELL SV, HFSS has a reliable mesh adaptation algorithm and several simulation convergence criteria. The *S*-parameter convergence criterion was defined to be better than 0.0025. The project mesh reached 2.4 million tetrahedral after 25 mesh adaptation steps. The open-circuit admittance matrix $\widehat{\mathbf{Y}}$ was calculated using both the HFSS solver and the proposed 2n-port method. A good correlation was observed for open-circuit admittance matrices obtained with both methods.

3.6.3 Port admittance matrix characteristics

While simulating the open-circuit admittance matrix $\widehat{\mathbf{Y}}$ for the small coil, ports at the location z = 0 are numbered from 1-12 and the ports at location z = l are numbered from 13-24. With the above notation, the ports on the opposite ends of the same elements are differed by 12. The open-circuit admittance matrix $\widehat{\mathbf{Y}}$ for the small coil is a 24 element square matrix. It is also a 2 x 2 block circulant matrix, with each block being a 12 element circulant matrix. As described in the theory section, $\widehat{\mathbf{Y}}$ can be diagonalized by a special matrix $(\mathbf{F_2} \otimes \mathbf{F_{12}})$ and its conjugate [45]. If such coil is made to resonate then the current distribution on the ports for the k^{th} mode is given by the complex coefficients of the k^{th} row vector of the matrix $(\mathbf{F_2} \otimes \mathbf{F_{12}})$.

3.6.4 Mode Description: Propagating modes vs. Port modes

A strongly coupled n element CMTL represented as a 2n port network, will have a port admittance matrix of size 2n x 2n. The admittance matrix will then have 2n eigenvalues, where each eigenvalue corresponds to a port resonant mode. In most of the literature, it was described that an n element CMTL produces n resonant modes (or n axial resonant modes) [4][40]. These can be attributed to the propagating modes of a transmission line. If the modes are defined by appropriately incorporating terminations and boundary conditions, then an *n*-element CMTL produces 2*n* standing wave resonant modes.

Standing wave resonant modes occur due to the boundary conditions or discontinuities at the terminals. In the 2n-port model presented in this research, port resonant modes are related to the standing wave resonant modes. The difference between a propagating mode and a standing wave resonant mode is that each propagating mode will have a distinct propagating constant γ. Each γ is associated with two standing wave resonant modes. One mode is due to the constructive interference (addition) of a forward, and a reverse traveling wave and the other mode is due to the destructive interference (subtraction) of a forward, and a reverse traveling wave. Among the 2*n* resonant modes occurring, half are axial resonant modes of an electrically lengthened, *n* conductor, short-circuited λ/2 line and the remaining half being the axial resonant modes of an electrically shortened, *n* conductor, open-circuited λ/2 line.

3.6.5 $(\mathbf{F_2} \otimes \mathbf{F_{12}})$ Matrix characteristics

It is interesting to observe the characteristics of the row vectors of the $(\mathbf{F_2} \otimes \mathbf{F_{12}})$ matrix to understand the mode currents on the ports. One remarkable property of the matrix $(\mathbf{F_2} \otimes \mathbf{F_{12}})$ is that there are ten degenerate pairs of row vectors. A degenerate pair of vectors can be described as a pair of vectors whose elements are identical in magnitude and in phase. Table 3 shows the row vectors of $(\mathbf{F_2} \otimes \mathbf{F_{12}})$ with their degeneracy characteristics.

Table 3: Row vectors of $(\mathbf{F_2} \otimes \mathbf{F_{12}})$ with degenarate charcteristics. Each mode corresponds to a row entry of $(\mathbf{F_2} \otimes \mathbf{F_{12}})$ matrix with mode 0 corresponds to the first row.

Mode 0		
Mode 1	Mode 11	Circular degenerate modes with 2 degrees of degeneracy
Mode 2	Mode 10	
Mode 3	Mode 9	
Mode 4	Mode 8	
Mode 5	Mode 7	
Mode 6		
Mode 12		
Mode 13	Mode 23	Anti-circular degenerate modes with 2 degrees of degeneracy
Mode 14	mode 22	
Mode 15	Mode 21	
Mode 16	Mode 20	
Mode 17	Mode 19	
Mode 18		

Port modes are numbered such that the port mode 0 corresponds to the first-row vector and the port mode 23 corresponds to the 24th-row vector of the matrix. Each element in a row relates to a numbered port. It can also be seen that the first twelve row vectors are anti-circular in nature and the next twelve row vectors are circular in nature. Elements are said to be exhibiting an "anti-circular behavior" when (1-n) elements of row vector quantities are in phase with (n+1)–2n elements. Similarly, "circular behavior" can be described as when the 1-n elements of the row vector are 180^0 out of phase with the (n+1)-2n elements. The description is a very distinctive feature which is the source for the association of port modes to open-ended resonance and short-circuited resonance. "Anti-circular behavior" can be attributed to axial resonant modes of an electrically lengthened, *n* conductor, short-circuited λ/2 line. "Circular behavior" can be attributed to an electrically shortened, *n* conductor, open-circuited λ/2 line.

Fig.7-Fig.12 show current distributions on the ports for different modes. In each figure, the subplots (a) and (b) represent the real and imaginary components of current distribution on the ports, and the subplots (c) and (d) represent the current distribution in a complex plane. These distributions correspond to the row vectors of $(\mathbf{F_2} \otimes \mathbf{F_{12}})$. For each mode, the real and imaginary components of its row vector are plotted as a function of port numbers. To demonstrate the degeneracy as well as the rotational and co-rotational nature, the vector elements are plotted on a X-Y plane of a 3D plot as two different sets of ports: 1-n and (n+1)-2n, where n = 12. The Z axis represent the axial length dimension. It must be recalled that ports 1-n are located at one end of the coil (z = 0) and port (n+1)-2n are located at the other end of the coil (z = 152.5mm).

The plotting used here is helpful in understanding and visualizing a mode current distribution. For example, it can be visually realized that mode 1 and mode 13 are the useful modes for MR imaging as they have sinusoidal distribution and are likely to produce the required homogeneous field. The circular behavior of mode 13 and mode 23 can be observed from the plots in the complex plane. Similarly, the anti-circular behavior of mode 1 and mode 11 can also be observed from the complex plane plots. A more detailed visual representation of the port currents and the current along the elements will be shown in the HFSS simulation results section. It is very important to recall the fact that the direction of port currents is chosen such that they all flow into the elements.

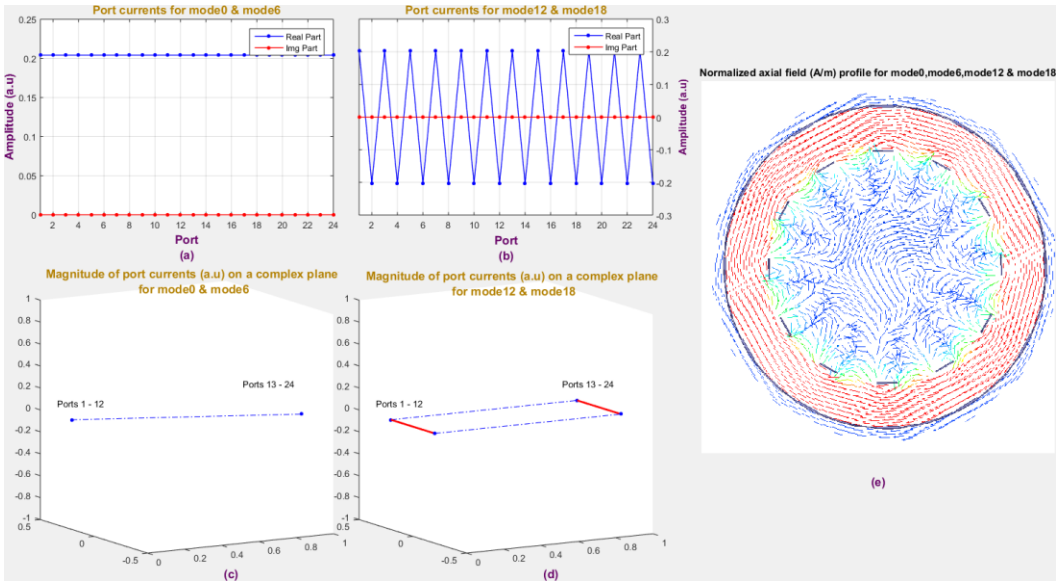

Fig.7: Port current distribution at the ports for mode 0, mode 6, mode 12 and mode 18. In the plots (a) and (b) the blue dots represent the real components, and the red dots represent the imaginary parts of the coefficients representing the port currents. Plots (c) and (d) display the magnitude of the port currents in a real and imaginary plane. Plot (e) shows the normalized axial magnetic field profile. The magnetic field is confined between the shield and the elements making to useless for MR applications.

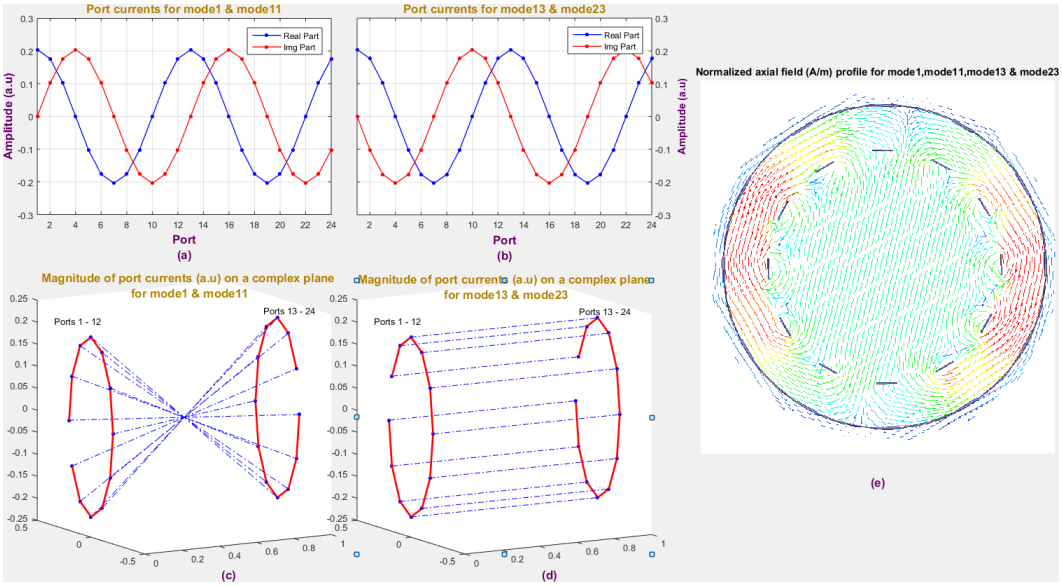

Fig.8: Port current distribution at the ports for mode 1, mode 11, mode 13 and mode 23. In the plots (a) and (b) the blue dots represent the real components, and the red dots represent the imaginary parts of the coefficients representing the port currents. Plots (c) and (d) display the magnitude of the port currents in a real and imaginary plane. Plot (e) shows the normalized axial magnetic field profile. The magnetic field is uniform at the center region making this mode useful for MR applications.

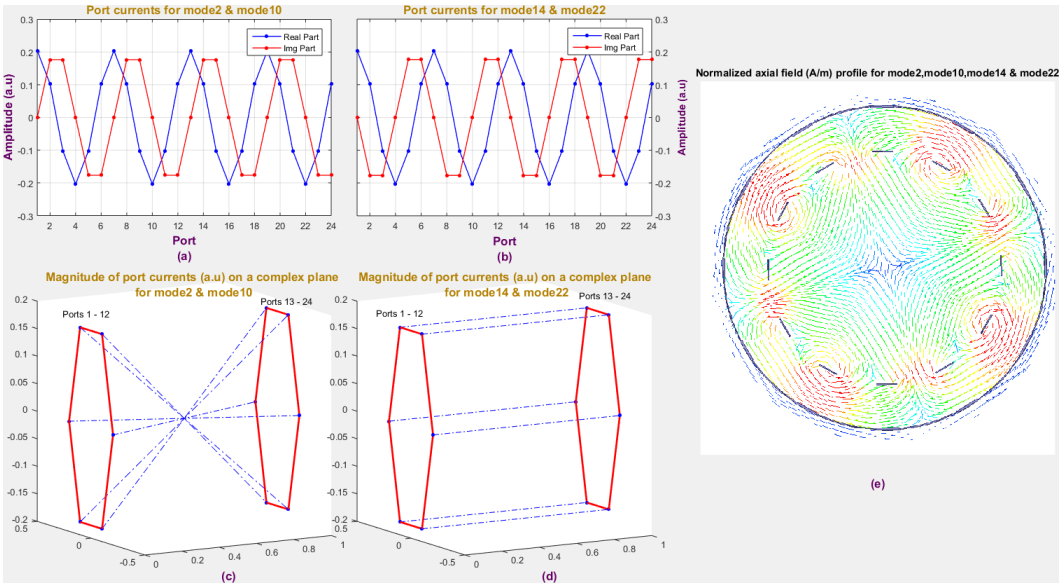

Fig.9: Port current distribution at the ports for mode 2, mode 10, mode 15 and mode 22. In the plots (a) and (b) the blue dots represent the real components, and the red dots represent the imaginary parts of the coefficients representing the port currents. Plots (c) and (d) display the magnitude of the port currents in a real and imaginary plane. Plot (e) shows the normalized axial magnetic field profile. The magnetic field has a null at the center region making this mode less useful for MR applications.

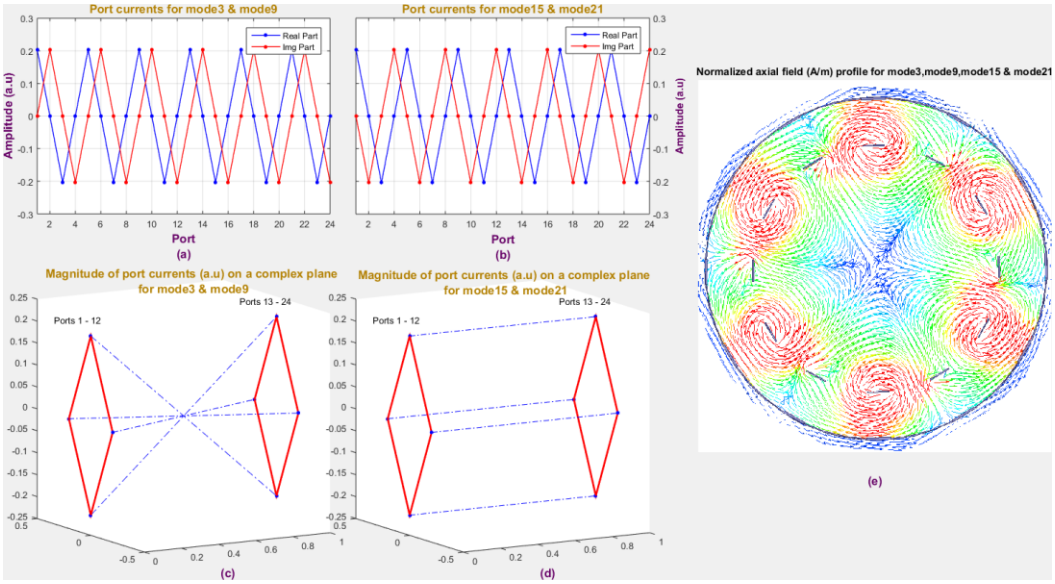

Fig.10: Port current distribution at the ports for mode 3, mode 9, mode 15 and mode 21. In the plots (a) and (b) the blue dots represent the real components, and the red dots represent the imaginary parts of the coefficients representing the port currents. Plots (c) and (d) display the magnitude of the port currents in a real and imaginary plane. Plot (e) shows the normalized axial magnetic field profile. The magnetic field has a bigger null region at the center making this mode not useful for MR applications.

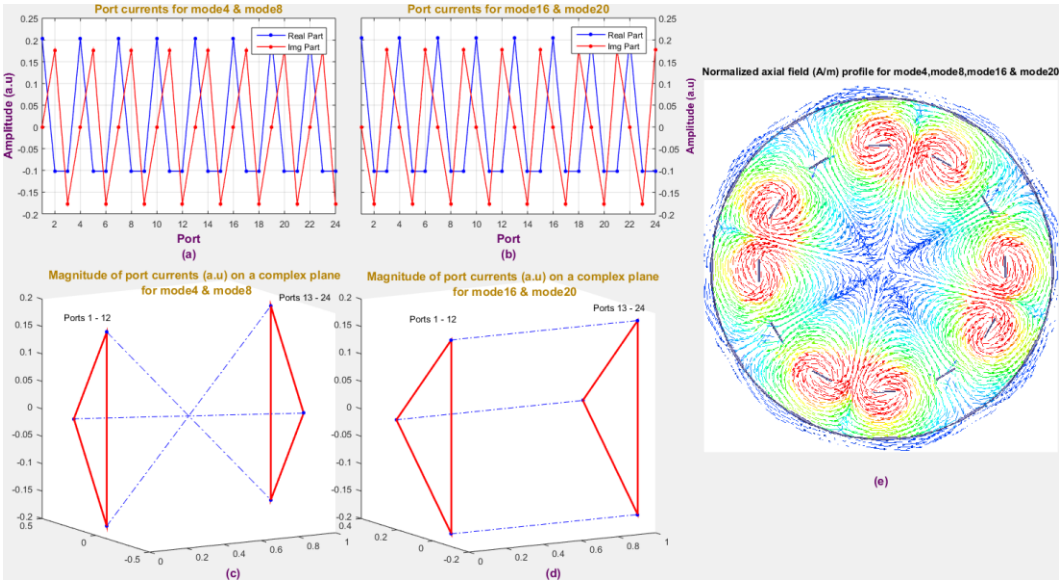

Fig.11: Port current distribution at the ports for mode 4, mode 8, mode 16 and mode 20. In the plots (a) and (b) the blue dots represent the real components, and the red dots represent the imaginary parts of the coefficients representing the port currents. Plots (c) and (d) display the magnitude of the port currents in a real and imaginary plane. Plot (e) shows the normalized axial magnetic field profile. The magnetic field has a bigger null region at the center making this mode not useful for MR applications.

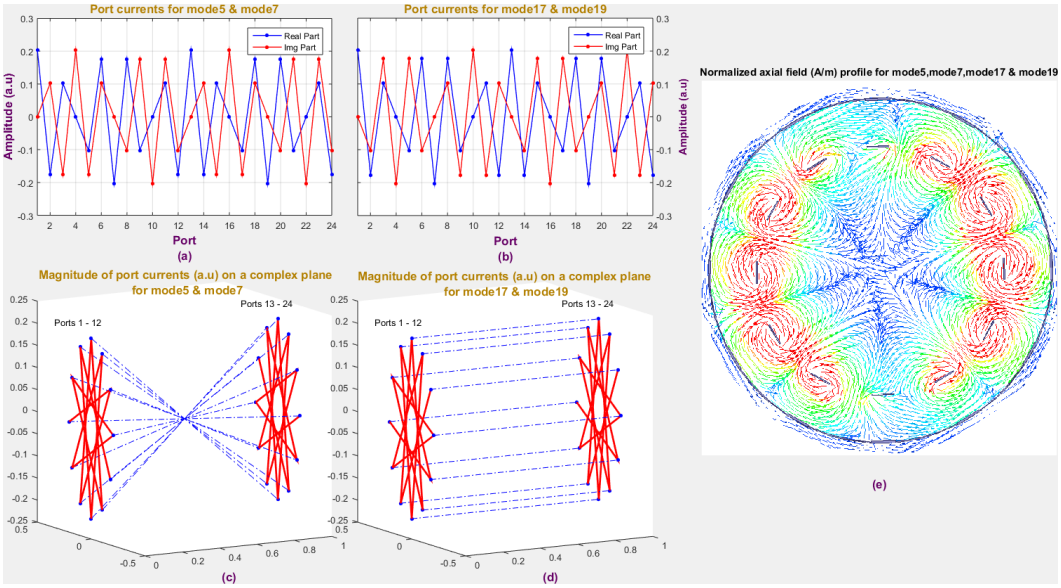

Fig.12: Port current distribution at the ports for mode 5, mode 7, mode 17 and mode 19. In the plots (a) and (b) the blue dots represent the real components, and the red dots represent the imaginary parts of the coefficients representing the port currents. Plots (c) and (d) display the magnitude of the port currents in a real and imaginary plane. Plot (e) shows the normalized axial magnetic field profile. The magnetic field has a bigger null region at the center making this mode not useful for MR applications.

3.7 Single resonant MTL coil simulation and analysis

Modes vs. termination component value

Using the proposed 2n-port model, the required terminating values for different modes are simulated. Fig.13 shows both the capacitive and the inductive termination values required to resonate various modes of the small coil for frequencies at 200MHz and 300MHz, and the big coil for the frequency at 200 MHz.

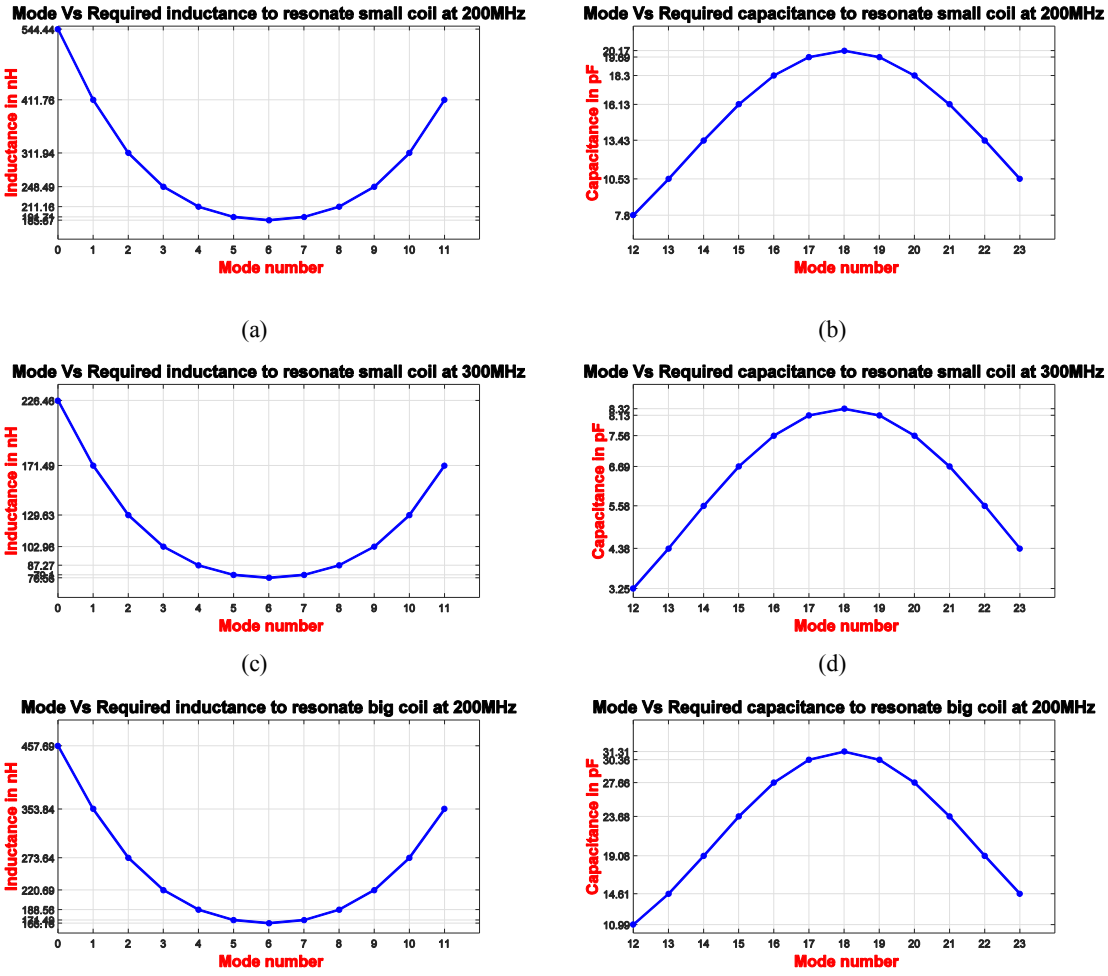

Fig.13: Required terminating component values for different mode resonances (a) to resonate mode 1 of the small coil at 200 MHz (b) to resonate mode 13 of the small coil at 200 MHz (c) to resonate mode 1 of the small coil at 300 MHz d) to resonate mode 13 of the small coil at 300 MHz(e) to resonate mode 1 of the big coil at 200 MHz (f) to resonate mode 13 of the big coil at 200 MHz.

A capacitance value of 10.52 pF is obtained to resonate the mode 13 (a mode of interest for MRI applications) of the small coil at 200MHz. It matches well with the published result of 10.46 pF. It is interesting to note that for the higher order modes of the chosen coil configurations (small and big rat coils) the required capacitance increases, while the inductance decreases.

Validation of 2n port model

Fig.14 displays the comparison of mode resonances as predicted by the proposed 2n-port model, the resonance predictions of the MTL model, and the network analyzer measurements of both small and big coils as described in [4]. In general, good agreement exists between 2n port simulations and MTL model.

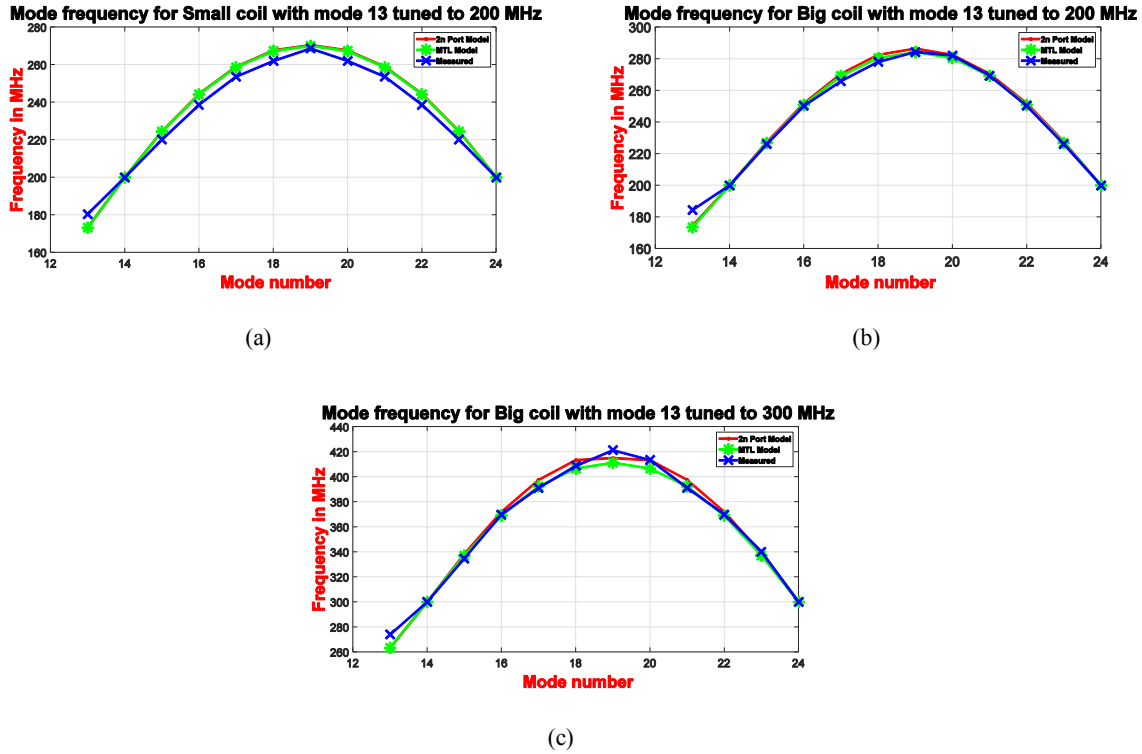

Fig.14: Comparison of 2n-port model predicted resonance frequencies with experimentally measured coil resonance frequencies, and multiconductor transmission line (MTL) model predicted mode frequencies as reported in [4] for a) resonant mode 13 of the small coil at 200MHz b) resonant mode 13 of the big coil at 200MHz and c) resonating mode 13 of the big coil at 300 MHz.

Frequency vs. termination component value

The variation of the terminating capacitance required to resonate the small coil for different frequencies is simulated. Fig.15(A) shows the terminating capacitances needed to resonate the mode 13 of the small coil as a function of frequency between 100MHz to 1000MHz. The above result is a reproduction of the result presented in [50]. Fig.15(B) shows terminating inductance required to resonate the mode 1 of the small coil as a function of frequency between 100MHz to 1000MHz.

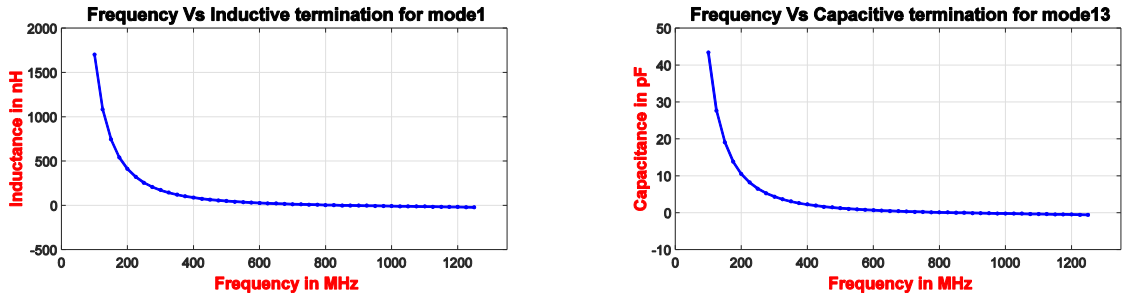

(a) (b)

Fig.15: required terminating component values to resonate the small coil at a) mode 1 and b) mode 13 for different frequencies ranging from 100MHz to 1300MHz.

Fig.16 shows the termination component values required to resonate the mode 1 and the mode 13 for an expanded frequency range of 100MHz to 3000MHz. From Fig.16 it can be observed that for the mode 13, the required admittance value is changing from positive to negative and then to positive. It implies that the required termination changes from a capacitor to an inductor and then to a capacitor and so on as a function of increasing frequency. At frequencies where the structure's electrical length is less than an odd multiple of the wavelength, the required terminating component is a capacitor. Similarly, for frequencies where the electrical length is greater than an odd multiple of the wavelength but less than next even multiple of the wavelength, the required terminating component value is an inductor.

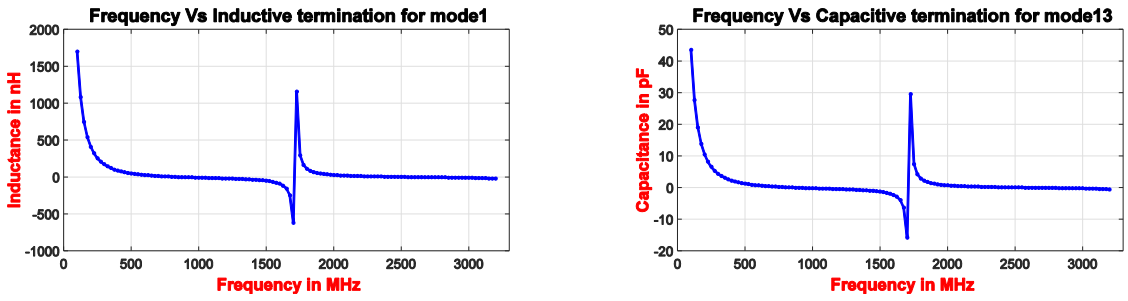

(a) (b)

Fig.16: required terminating component values to resonate the small coil at mode 13 for different frequencies ranging from 100MHz to 3500MHz.

Frequency vs. terminations for various modes

Fig.17 shows the required termination values for various modes as a function of frequency on a single plot. It should be observed that as the frequency increases, all mode terminations tend to converge. At the point of convergence, all modes collapse and the coil elements are completely decoupled with others. This situation is similar to the natural decoupling technique as proposed by Lee et al. in their seminal paper on planar strip arrays[38]. For mode 13 at the point of convergence, the termination capacitor value is zero indicating an open condition and resonance is an open-circuited λ/2 line. Similarly, for mode 1 at the point of convergence, the termination inductor value is zero showing a short condition and resonance is a short-circuited λ/2 line.

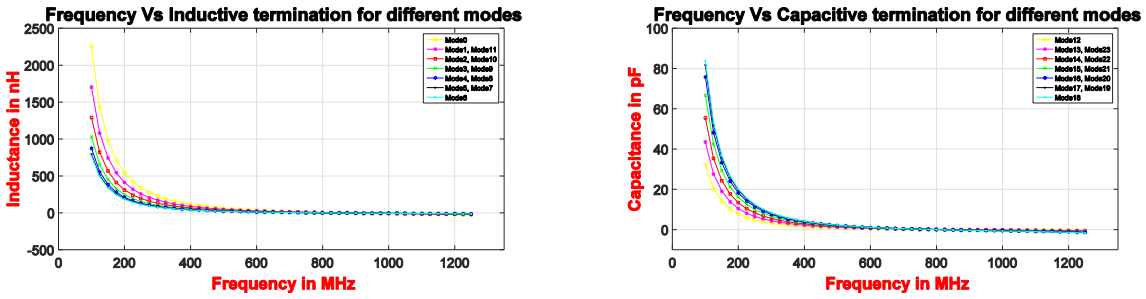

(a) (b)

Fig.17: required terminating component values for different modes as a function of frequency ranging from 100MHz to 1300 MHz for the small coil.

Length vs. termination component value

Fig.18 shows the required termination values to resonate the mode 1 and the mode 13 of the small coil at 200 MHz as a function of the length. The illustrated results are identical to results obtained in the analysis between the termination values and the frequency. As the length increases, the required components changes from capacitors to inductors or inductors to capacitors and vice versa. The similarity between the results is because the variation of frequency or length is equivalent to the change of the electrical length of the structure.

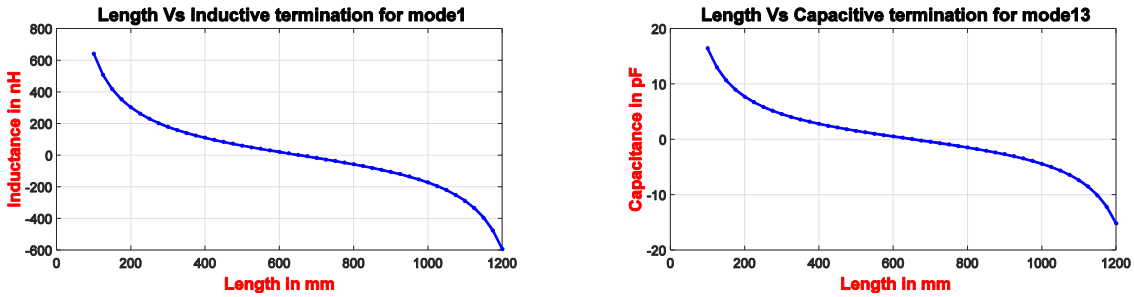

(a) (b)

Fig.18: required terminating component values as a function of length to resonate the small coil at (a) mode 13 and (b) mode 1.

Variation of termination capacitance as a function of the capacitance ratio

Fig.19 shows the variation of the terminating capacitance values as a function of their ratios, simulated for the small coil, resonating the mode 13 at 200MHz. For the case where the ratio is unity, the predicted terminations value of 10.52 pF agrees well with the published result in [1].

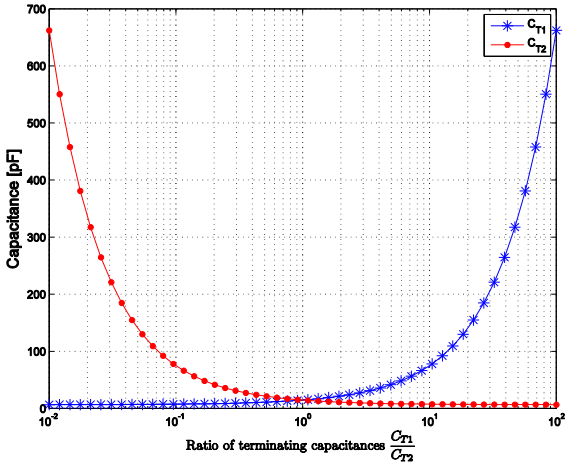

Fig.19: Variation of terminating capacitance as a function of terminating capacitance ratio $\frac{C_{T1}}{C_{T2}}$ for the small coil resonating mode 13 at 200 MHz resonant frequency.

HFSS simulation

HFSS simulations using the eigenmode solver were performed on the small coil to validate the 2*n* port model. The HFSS simulation results for the mode 13 (left column) and the mode 1 (right column) for equal terminations are presented in Fig.20. The termination component values are chosen from the 2n-port model predicted values. Port current distributions for the capacitive and the inductive terminations are shown in plot A1 and B1.

It can be observed from the plots that the mode 13 is a co-rotational mode, and the mode 1 is an anti-rotational mode. In a co-rotational mode, currents have their peak at the center of the transmission line, and in anti-rotational modes, currents have a null at the center of the transmission line. The presence of current peaks and nulls is further validated by the plots A2 and B2 of Fig.20. The A2 and B2 plots show the current distribution along the length of the strips for the mode 1 and the mode 13. Current distribution on the strips is simulated using the chain parameters, computed port currents, and voltages.

The axial, the coronal and the sagittal B_1 field profiles using the HFSS simulations for the mode 13 and the mode 1 are shown in A3-A5 and B3-B5, respectively. The HFSS field plots match well with the 2n-port model predicted current plots of A2 and B2. The axial field plot presented for the mode 1 in B3 of Fig.20

was collected at an offset point of 50 mm from the center of the coil. This offset was required as the field null occurs at the middle of the coil for the mode 1. Fig.21 presents similar results for unequal terminations with a ratio of 0.5. From the field plots in Fig.21, it is worth noting that the field peak or null can be moved away from the center and a B_1 field gradient can be created with unequal terminations.

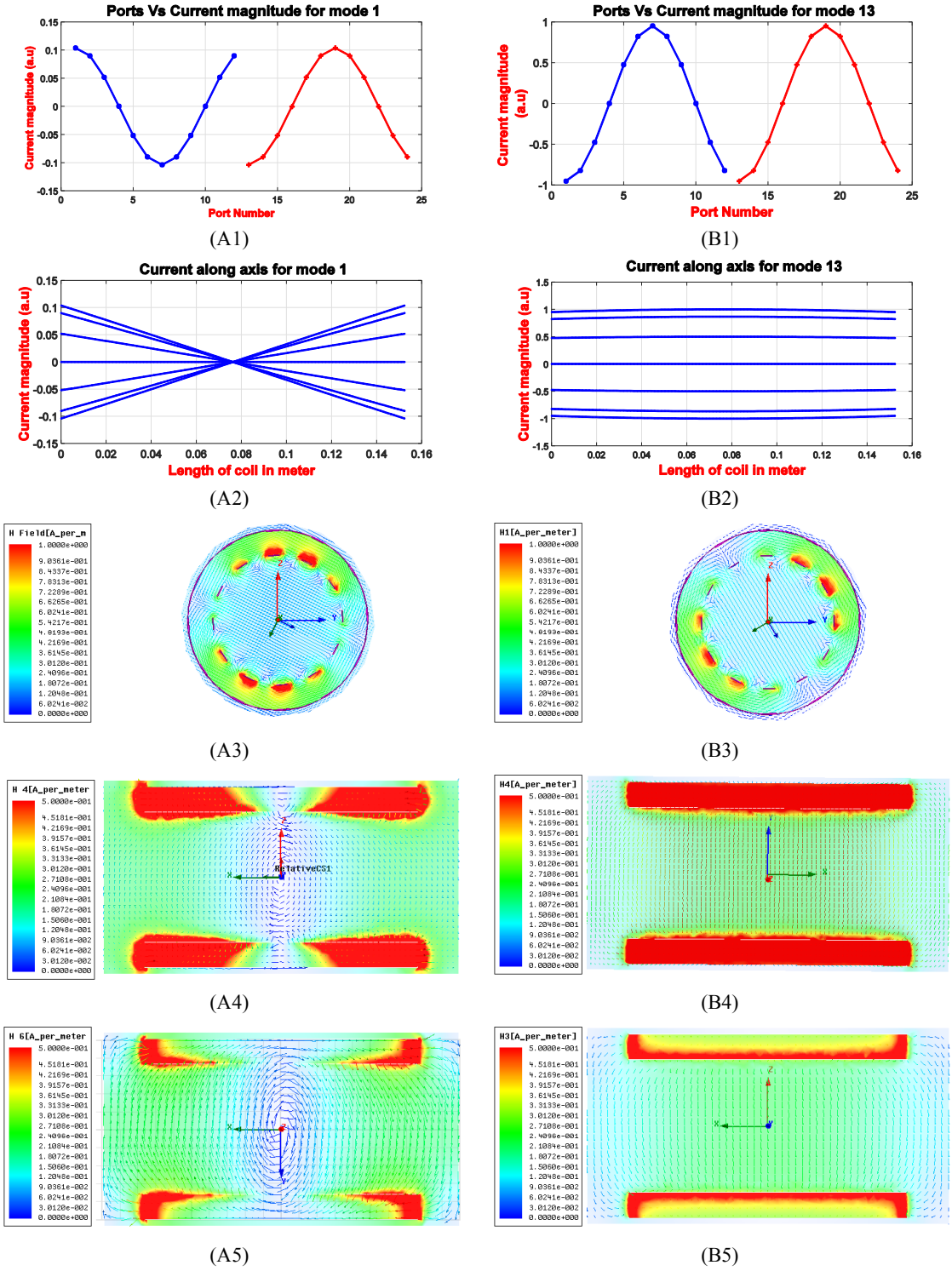

Fig.20: Current distribution and field plots with equal admittance terminations on both ends. Port currents for A1) anti-rotational mode1 B1) co-rotational mode13. Current distribution along the axis of the coil for A2) mode1 B2) mode13. Axial field plot in XY plane for A2) mode1 B2) mode13. Coronal field plots in XZ plots for A4) mode1 B4) mode13. Sagittal plots in YZ plane for A5) mode1 B5) mode13.

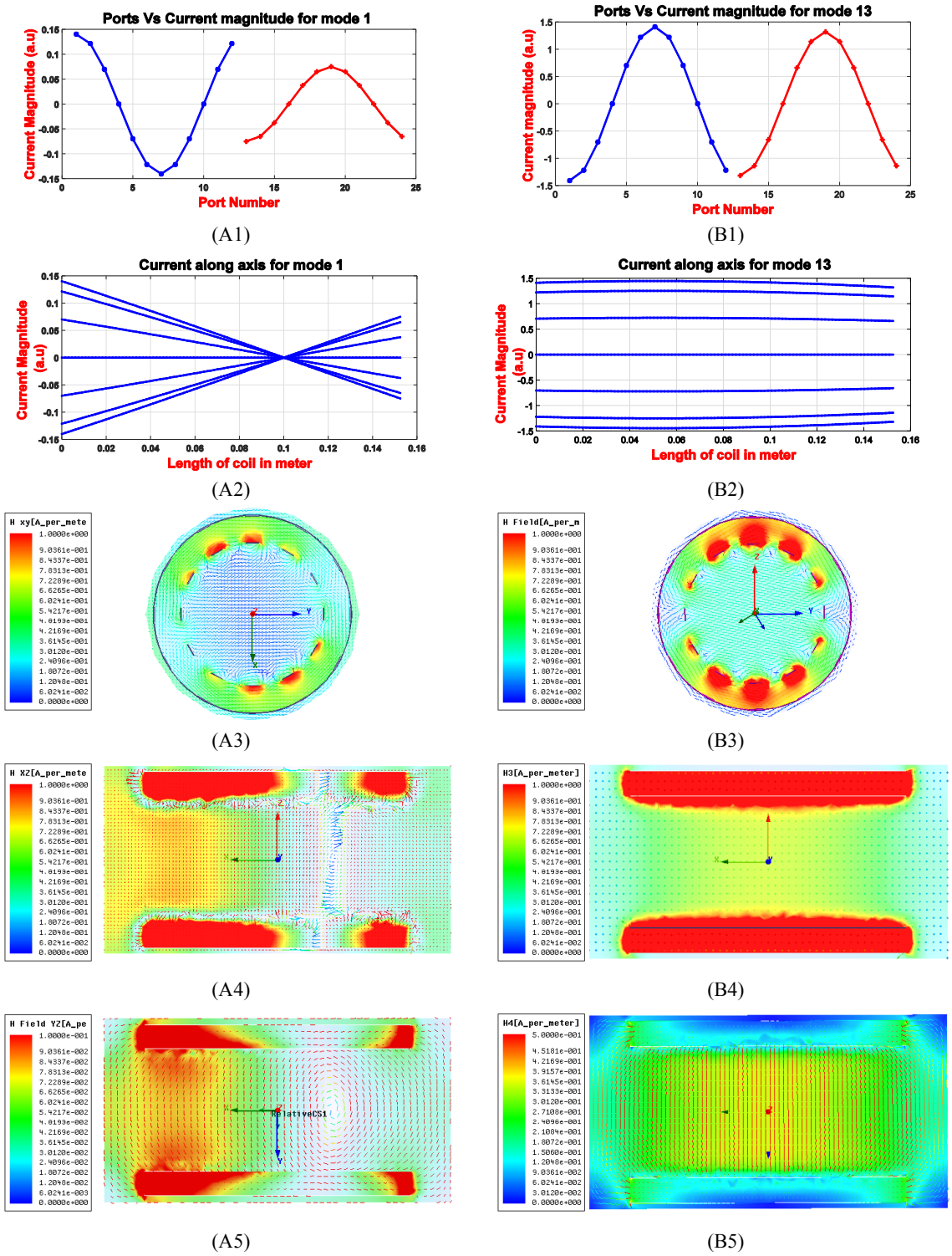

Fig.21: Current distribution and field plots with unequal admittance terminations on both ends. Port currents for A1) anti-rotational mode1 B1) co-rotational mode13. Current distribution along the axis of the coil for A2) mode1 B2) mode13. Axial field plot in XY plane for A2) mode1 B2) mode13. Coronal field plots in XZ plots for A4) mode1 B4) mode13. Sagittal plots in YZ plane for A5) mode1 B5) mode13.

3.8 Dual tuned dual-element coil analysis

As a demonstration of the proposed 2n-port model, a new dual element, dual-tuned surface coil for a 7T MRI scanner was developed. The proposed coil was designed to image the proton nuclei (298 MHz) and the sodium nuclei (78.6 MHZ) in a Philips 7T MRI scanner.

3.8.1 Coil construction

The coil consists of two strip elements made with a copper-clad FR4 sheet of 1mm thickness, 12.7mm in width and 152.4mm in length. Both elements were placed on an arc of radius 140mm and describing an angle of 45 degrees (center to center). The shield consists of 5 pieces of copper-clad FR4 sheets each of 1mm thickness, 12.7mm in width and 152.4mm in length. The shield pieces were placed on an arc of radius 152.4mm. The complete structure formed a partial volume coil with an arc length of 90 degrees. Both the elements and the shield were bolted to a front PCB board, and a back PCB board using machined brass pieces. The brass pieces provide the electrical connectivity and the mechanical strength. The requisite cable connectors, termination chip capacitors, and impedance matching networks were placed on the PCB boards. For tuning purposes, a trimmer capacitor (55H01, Johannsson Manufacturing, USA) was mounted in parallel to a chip capacitor (Passive Plus, NY, USA) on one end of each element. Impedance matching of the coil was achieved by a trimmer capacitor (55H01, Johansson Manufacturing, USA) connected in series with the microstrip element.

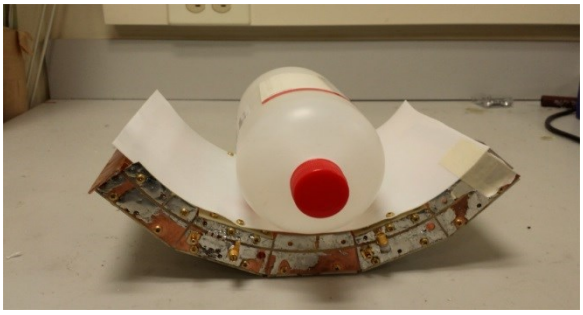

Fig.22: Photograph of the front view of the dual element dual tuned coil loaded with a phantom.

3.8.2 Coil simulation

Port admittance calculation

A 152.4mm long, 100mm diameter cylindrical bottle filled with 75mM NaCl solution was used as a loading and imaging phantom. Its conductivity of 7.8 S/m was measured using a conductivity meter (HI 8733, Hanna Instruments) and incorporated into the EM simulations. Full-wave 3D EM simulations were performed using the HFSS-driven terminal solver to generate the open port admittance matrix $\hat{\mathbf{Y}}$ at the proton frequency of 298MHz, and at the sodium frequency of 78.6MHz.

Determination of tuning capacitors

As shown in the schematic in Fig.6, Y_{T1} and Y_{T2} are the terminations used for each element. Ports are numbered such that the computed $\mathbf{Y}_{sL}$ leads to the form described in Case II. Determinant equations as shown in equation (88) are written for both frequencies, and the values of Y_{T1} and Y_{T2} are computed by solving them numerically. A capacitance of 166.2 pF for element 1 and a capacitance of 10.32 pF for element 2 are predicted with the proposed 2n-port method. The computed values of Y_{T1} and Y_{T2} were verified by performing the 3D EM simulations using the HFSS eigenmode solver. The obtained resonant frequencies using the eigenmode solver for the constructed coil are within 1 % of error tolerance.

3.8.3 Bench measurements

The reflection coefficient and the transmission coefficient were measured under loaded conditions with an Agilent 5071C network analyzer, and are shown in Fig.23. The coil was matched more than -21dB for both the channels and had an isolation between the channels better than -21dB at both the frequencies. The coil had an unloaded to loaded quality factor ratio of 3.2 at sodium frequency and 2.5 at proton frequency.

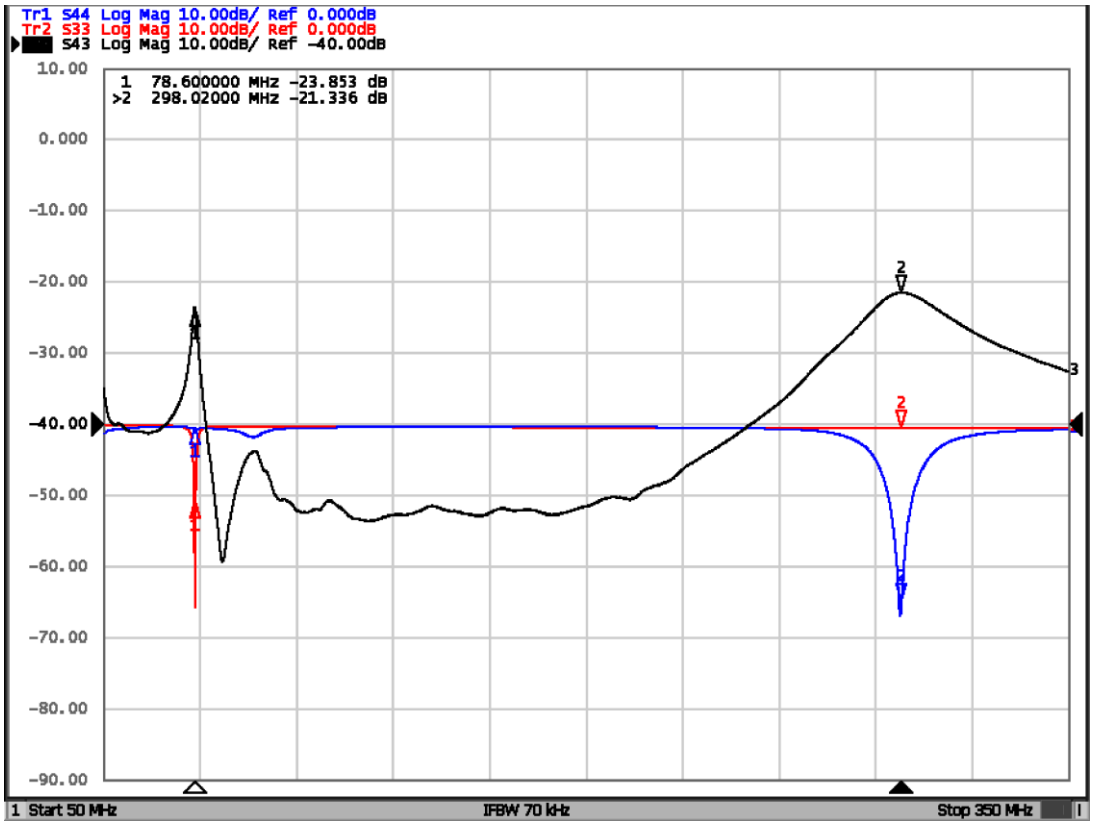

Fig.23: network analyzer measurements for the proposed dual element surface coil for the ^{23}Na channel connected to port 3 and the ^{1}H channel connected to port 4 (S_{33} and S_{44} measurements for the ^{23}Na and ^{1}H channels, respectively).

3.8.4 Imaging

Axial planar images passing through the center slice of the coil and a loading phantom were obtained using a gradient echo (GRE) sequence with the Philips 7T scanner. Two proton images were obtained, one with a saline loading phantom and the second one with a mineral oil phantom. The proton imaging acquisition parameters were: flip angle (FA) = 30 deg, TR = 150 ms, TE = 10 ms, FOV = 200 X 200 mm2, imaging matrix = 256 X 256, slice thickness = 5 mm, bandwidth = 320 Hz/pixel, number of averages = 1.

Similarly, sodium images were acquired for the same slice with the following acquisition parameters: flip angle (FA) = 30 deg, TR = 100 ms, TE = 104.5 ms, field of view (FOV) = 200 X 200 mm2, acq matrix = 32 X 32, recon matrix = 64 X 64, slice thickness = 5.5 mm, bandwidth = 260 Hz/pixel, in-plane resolution = 3.15 X 3.15, number of averages = 40.

Fig.24 shows the proton images and Fig.25 shows the sodium image, displaying the signal intensity profiles for each channel. The imaging results indicate that the prototype coil has a good intensity profile at both frequencies, thus underscoring the utility of the proposed method for the design of multi-resonant coils.

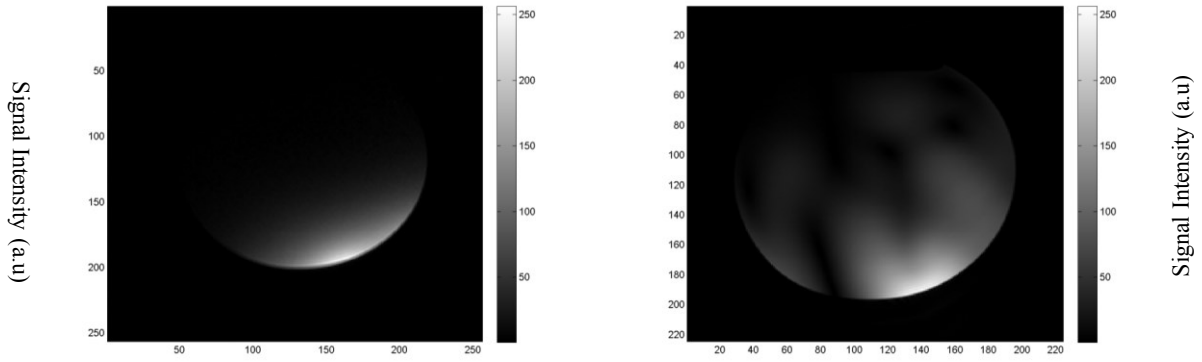

(a) (b)

Fig.24: MR images of the dual element dual tuned coil at 7 T: (a) ^{1}H signal intensity in arbitrary units (a.u.) image of an oil phantom (b) ^{1}H signal intensity (a.u.) image of a saline loading phantom.

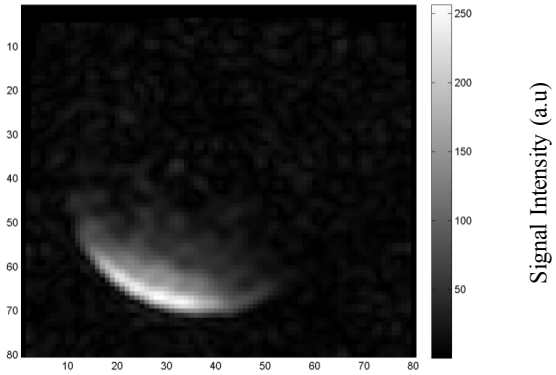

Fig.25: ^{23}Na signal intensity in arbitrary units (a.u.) image of a loading phantom on axial plane.

3.9 Discussion and Conclusion

In this chapter, a new methodology for designing RF coils using the 2n-port model and Kronecker product operator is presented. Some of the novelties presented in this chapter are: representation of MTL structure with a port admittance matrix, a mathematical proof that shows that the computation of the determinant of the admittance matrix is equivalent to solving the input impedance, application of the Kronecker product operator to simplify the eigenvalue calculation, and a new dual tuned dual element coil design.

The new 2n-port model predicts all intrinsic port modes, some of which were not considered in earlier investigations. The model also presents a theoretical formulation for unequal terminations, which explains their effects on mode separation. In contrast to the other models, the port admittance model can predict the anti-rotational modes that result in $\boldsymbol{B}_1$ field variation along the z-axis, typically used in applications such as $\boldsymbol{B}_1$ gradient encoding along the z-axis. One of the major restriction on the utilization of port admittance is for MTL structures. An open port admittance matrix does not exist for frequencies where the electrical length is an integer multiple of the coil's half wavelength. The model still finds its usefulness as this work seeks to ascertain the termination conditions for resonance using electrical lengthening or shortening of the multiconductor transmission line whose electrical length different from the half wavelength.

The strength of 2n-port model comes from the use of the Kronecker product operator to reduce the computational complexity and also to obtain analytical formulations. The limitation of the mentioned approach is that it is effective only for admittance matrices which are of the form *block circulant with circulant blocks* matrix $BCCB_{m,n}$. Even though most of the existing coils satisfy that condition, it is not a good approximation for multi-resonant designs or any future coil designs. In the next chapter, a more powerful reduced dimension method is proposed to overcome such a limitation.

With the 2n-port model, for unequal terminations for single resonance or different terminations for multiple resonances, the equation presents itself in a quadratic form. Therefore, numerical techniques are needed to obtain the solution which decreases the helpfulness of a 2n-port model. The advantage of the 2n-port model comes from the ease of getting the admittance matrix either experimentally or numerically.

The major inadequacy of the work presented in this chapter is that all work includes either unloaded conditions or symmetrically loaded conditions. Also, loss mechanism (both load and conductor losses) was not incorporated into the models. Although the presented results are useful, consideration for biological and asymmetric loads with loss mechanism would be very advantageous. Future efforts should be directed towards such goal.

Chapter 4

Coil design using reduced dimension method

4.1 Introduction

The volume coil designs include Helmholtz coils, saddle coils, and high pass and low pass birdcage coils [3], [22], [35], [51]. Of these coils, the birdcage coil is the most popular as it produces a homogeneous field over a large volume inside the coil. A birdcage resonator consists of two circular end rings connected by N equally spaced straight elements of inductance L, and each including a capacitance C. Each of the N elements introduces a phase shift $\varphi(\omega)$. The total phase shift being an integer multiple of 2π, the resonant condition appears as $N\varphi(\omega) = 2\pi M$. A standing wave in the low-frequency mode (M=1) generates currents in straight elements proportional to cos(θ) which produces the most homogeneous B1 field inside the cylinder. Higher frequency resonant modes produce increasingly less homogeneous B1 fields as M increases. The birdcage design can be operated in a quadrature mode. In the quadrature mode, the excitation of the coil or its signal reception is performed at two locations in the coil, which are 90 degrees out of phase electrically.

Most of the previously reported dual tuned volume coils are based on the birdcage design. The first design is a birdcage coil with an unequal distribution of capacitances [52]. The key idea for double resonant operation in this configuration is to arrange two linear field modes that will have two desired resonant frequencies. The major disadvantage of this configuration is that it works well only for resonant frequencies which are close to each other. There is a tradeoff for homogeneity if the frequencies are widely separated. Strong B1 field distortions will appear when the frequencies are widely separated, as they are for P_{31} and H_1. This configuration is difficult to tune. The coil needs to be fed through an inductive coupling, which under high power operation, can lead to arcing.

Amari et al.[53] extended the unequal distribution of capacitances birdcage configuration to quadrature excitation by presenting a theoretical framework for a multiple-tuned coil using unequal capacitance values.

Two disadvantages of that design are 1) the requirement for enough elements to ensure a homogeneous B_1 field and 2) an asymmetrical capacitance distribution, which theoretically creates a non-uniform B_1 field. It also increases the difficulty of two-channel balancing for quadrature design.

One more variation of Lu's design (design with unequal distribution of capacitances) is the four-legged birdcage design as described in ref [54] by Lanz and his coworkers. In Lanz's design instead of driving the coil in a quadrature mode, the two orthogonal modes are tuned for double resonance. Working in a non-quadrature drive will result in a decrease of RF homogeneity. Tuning a birdcage coil to two very different frequencies becomes possible without additional field distortions. Matson and Hill [55] have described their double-tuned birdcage coil design, which incorporates both individually tuned rungs and the use of traps (parallel resonating circuits). Normally, tuning and matching a double-tuned, double quadrature coil using this method of tuning each rung is time-consuming. In practice, implementation of these double-tuned coils in a double-quadrature can be challenging. A similar approach is used by Shen et.al[56]. They presented a new and straightforward mathematical model by using a generalized and asymmetric eigenvalue algorithm that simulates the performance of a single-tuned, low-pass birdcage coil. Shen model is extended to a dual-tuned, low-pass birdcage coil model by modifying the eigenvalues which are practically realized using the trap circuits.

One additional dual-tuned birdcage coil is the transformer coupled dual-tuned birdcage coil or coaxial birdcage coil developed by Fitzsimons et al. [57]. This design incorporates two birdcages in coaxial configurations. Each coil is tuned for individual frequencies taking the effect of mutual coupling into consideration. The disadvantage of Fitzsimons design is that it is difficult to tune co-axial coils. Mechanically coils have to be of different sizes.

The conventional volume coils like birdcage designs suffer radiation loss and self-resonance effects at high-frequency. To overcome these limitations transverse electromagnetic (TEM) resonators were introduced. A TEM resonator is a high-frequency design with similarities to a shielded birdcage coil, was introduced by Röschmann[58]. Vaughan et al. [5] extended it by analyzing the structure in terms of a cavity resonator.

Vaughan et al. also showed that the structure could be double-tuned with alternate rungs tuned for the other frequencies.

Bogdanov and Ludwig [4] introduced the coupled microstrip line TEM resonator which is similar to a TEM resonator but uses microstrip lines instead of coaxial tubes for individual elements. The primary difference between a coupled microstrip line TEM resonator and a birdcage coil is the cylindrical shield, which functions as an active element in the TEM design. It provides a return path for the currents produced on the inner conductors. The coupled microstrip line TEM resonator behaves like a longitudinal multiconductor transmission line (MTL), capable of supporting standing waves that occur at high frequencies. Unlike a birdcage coil, the coupled microstrip line TEM resonator's inner conductors, which are microstrips, do not possess connections to their closest neighbors, but instead are connected directly to the shield through capacitive elements. Resonance mode separation is accomplished through mutual inductive coupling between the strips. Since all the strips are attached to the shield with tunable capacitive elements (commonly known as termination capacitance), the field distribution can be adjusted to achieve the best homogeneity for a required frequency.

A TEM coil can be described with a wave propagation model using multiconductor transmission line theory. MTL theory treats the microstrip conductors as coupled transmission lines with waves propagating in the longitudinal direction [40], [42]. As described in the introductory section of chapter 3, transmission line resonators are a half wavelength in electrical length. Most of the previously reported TEM coil designs are equivalent to a λ/2 long open-ended multiconductor transmission line resonators [3]. This is because the magnetic field is maximum and the electric field is minimum at the center of a λ/2 open-ended transmission line.

To realize a practical and useful design regarding size, shape and field patterns, TEM coils whose electrical length is not a multiple of half wavelength, are shortened electrically,[3]. For such TEM coils, a λ/2 open-ended transmission line configuration is achieved by electrically shortening them with a set of capacitors

on both ends. Similarly, a λ/2 short-ended transmission line configuration is realized by terminating the TEM coils with a set of inductors on both ends.

Currently, there are many different types of TEM resonators. They can be classified based on their mechanical construction, coupled conductor realization technique, and the way terminations are implemented. Coupled conductors in TEM coils are built with either microstrip or coaxial elements [4],[5]. Electrical shortening/terminations are realized either by using lumped elements or distributed transmission lines [4],[5]. Style of termination plays an important role especially for multi-tuned coils as the impedance value is a linear function of frequency for lumped elements and it becomes a nonlinear function of frequency for distributed transmission lines.

One of the initial multi-tuned transmission line resonator design was proposed by Durr and Rauch [59]. In their design, they use the pole insertion method realized by filters to obtain the required termination impedance at different frequencies. A disadvantage of pole insertion method technique is that this method leads to an efficiency problem at one of the frequencies.

Another useful design is the multi-tuned TEM coils developed by using different terminations on alternative conductors [5],[6]. The above technique can be called an interleaved design. Most of the analysis treats the coils as two separate interleaved coils tuned to different frequencies. The analysis is generally useful, but it could be more accurate if the complete structure is treated as one single coil. Based on the interleaved design, multi-tuned TEM designs can be classified into four types. The first category involves a coil where all the conductors are equal in dimensions and are arranged in the same radial position [5]. For the second category, conductors are not equal in dimensions, but their radial positioning is the same [60]. For the third type, both the radial position and the conductor dimensions are not identical [6],[61]. Even though no work has been presented for designs where all conductors are equal in dimensions, and alternative conductors are arranged at different radial positions, it can be considered as the fourth type for completeness of classification.

One of the major problems for interleaved designs is shading artifacts due to mode mixing of closely spaced modes [62]. The problem can be minimized by reducing the residual coupling between conductors which is achieved through optimization of conductor geometry and radial positioning [6]. To overcome the artifacts due to mode mixing, hybrid designs using interleaved TEM and birdcage were proposed [63]. In the present work, the residual coupling between the conductors is varied using lumped elements and this technique remove the restrictions on coil geometry.

Even though multi-tuned TEM coils are widely used, very few articles describe the analytical formulation for calculating the required terminations, current, and the field profiles. In this work, an efficient approach to design multi-tuned TEM coils is provided.

A (2n+1) conductor MTL is represented as a 4n port network, and its open port admittance matrix is generated either numerically or experimentally. Based on the MTL structure, the open circuit admittance matrix is rearranged such that its circulant block nature is still retained. By using the termination admittance matrix which is assembled to exhibit circulant block nature, eigenvalues are computed using the reduced dimension method [64]. The resonant conditions on the ports are determined by equating the required eigenvalue to zero. For dual resonance, the termination admittance matrix is populated with two different value terminations. A solution for those two terminations is obtained by solving the two resonant condition equations obtained from the eigenvalue problem at the two required frequencies. The advantage of this technique comes from the reduced dimension method which reduces a 4n X 4n matrix eigenvalue problem into a simple 2 X 2 matrix eigenvalue problem.

4.2 Theory

A (2n+1) conductor MTL can be treated as a passive 4n-port network system. The MTL can be represented as an open circuit admittance matrix $\widehat{\mathbf{Y}}$ as expressed in matrix form

$$\begin{bmatrix} \mathbf{I}(\mathbf{z}) \\ -\mathbf{I}(0) \end{bmatrix} = \begin{bmatrix} \mathbf{Y_{00}} & \mathbf{Y_{0z}} \\ \mathbf{Y_{z0}} & \mathbf{Y_{zz}} \end{bmatrix} \begin{bmatrix} \mathbf{V}(\mathbf{z}) \\ \mathbf{V}(0) \end{bmatrix} \tag{91}$$

The currents at both ends $\mathbf{I}(z)$ and $\mathbf{I}(0)$ are directed into the 4n ports. The sub-matrices $\mathbf{Y_{00}}$ and $\mathbf{Y_{zz}}$ of $\widehat{\mathbf{Y}}$ for a (2n+1) MTL of length z represent 2n x 2n elements matrices of self and mutual admittance for 2n-ports at z = 0 and z = l respectively. Similarly, matrices $\mathbf{Y_{0z}}$ and $\mathbf{Y_{z0}}$ represent mutual admittance between ports at z = 0 and z = l.

For an MTL structure $\widehat{\mathbf{Y}}$ is a reciprocal matrix [42], i.e., $\mathbf{Y_{00}} = \mathbf{Y_{zz}}$ and $\mathbf{Y_{0z}} = \mathbf{Y_{z0}}$. If the MTL is a symmetrical cyclic structure then $\mathbf{Y_{11}}$, $\mathbf{Y_{22}}$, $\mathbf{Y_{12}}$, and $\mathbf{Y_{21}}$ are circulant matrices. Even though sub-matrices are circulant, $\widehat{\mathbf{Y}}$ is not circulant, but it is a matrix of circulant blocks. In block matrix notation, $\widehat{\mathbf{Y}}$ is a circulant block matrix $CB_{m.n}$ [46]. A circulant block matrix $CB_{m.n}$ of order m and n is represented to be an m x m block matrix with n x n sized circulant blocks as elements.

Most of the multi-tuned TEM coils that were designed using interleaved designs are not symmetrically cyclic structures. Even for multi-tuned TEM coils which are symmetrical cyclic structures [5], their open circuit admittance matrix can be a block circulant matrix, but their port admittance matrix which includes terminations is not a block circulant matrix.

To take advantage of block circulant matrix algebra, port admittance $\widehat{\mathbf{Y}}$ needs to be rearranged. $\widehat{\mathbf{Y}}$ can be rearranged in the following way. Ports on alternative conductors and with identical terminations are numbered in sequential order and are succeeded by ports at the opposite end.

Interleaved multi-resonant MTL coils

Let us consider a symmetrical cyclic 2n+1 conductor interleaved multi-tuned MTL. It can be assumed that n conductors belong to set 1 and are interleaved alternatively with n conductors of set 2, and the remaining single shield conductor is acting as a grounded return path for both coils. If ports at z = 0 for set 1 are sequentially numbered from 1 to n, the ports at z = l for set 1 from n+1 to 2n, ports at z = 0 for set 2 from 2n+1 to 3n, ports at z = l for set 2 from 3n+1 to 4n, then the modified admittance matrix $\widehat{\mathbf{Y}}_{new}$ can be written as

$$\begin{bmatrix} \mathbf{I}_A(z) \\ -\mathbf{I}_B(0) \\ \mathbf{I}_C(z) \\ -\mathbf{I}_D(0) \end{bmatrix} = \begin{bmatrix} \mathbf{Y_{AA}} & \mathbf{Y_{AB}} & \mathbf{Y_{AC}} & \mathbf{Y_{AD}} \\ \mathbf{Y_{BA}} & \mathbf{Y_{BB}} & \mathbf{Y_{BC}} & \mathbf{Y_{BD}} \\ \mathbf{Y_{CA}} & \mathbf{Y_{CB}} & \mathbf{Y_{CC}} & \mathbf{Y_{CD}} \\ \mathbf{Y_{DA}} & \mathbf{Y_{DB}} & \mathbf{Y_{DC}} & \mathbf{Y_{DD}} \end{bmatrix} \begin{bmatrix} \mathbf{V}_A(z) \\ \mathbf{V}_B(0) \\ \mathbf{V}_C(z) \\ \mathbf{V}_D(0) \end{bmatrix} \quad (92)$$

where A, B, C, D are set of n ports at z = 0 for set 1, ports at z = l for set 1, ports at z = 0 for set 2, ports at z = l for set 2, respectively. Sub-matrices $\mathbf{Y_{ii}}$ represents the self and the mutual admittance of the ports in the set i ϵ A, B, C, D. Sub-matrices $\mathbf{Y_{ij}}$ represent the mutual admittance of the ports in the set i ϵ A,B,C,D with the set j ϵ A,B,C,D, and i≠j.

All the sub-matrices $\mathbf{Y_{ii}}$ are circulant in nature with a size n x n. Equation (92) can be rewritten as

$$\begin{bmatrix} \mathbf{I}_1(z) \\ \mathbf{I}_2(z) \end{bmatrix} = \begin{bmatrix} \mathbf{Y_{11}} & \mathbf{Y_{12}} \\ \mathbf{Y_{21}} & \mathbf{Y_{22}} \end{bmatrix} \begin{bmatrix} \mathbf{V}_1(z) \\ \mathbf{V}_2(z) \end{bmatrix} \quad (93)$$

where the sub-matrices $\mathbf{Y_{11}}$ and $\mathbf{Y_{22}}$ represent the admittance matrix of set1 and set 2, respectively. Sub-matrices $\mathbf{Y_{12}}$ and $\mathbf{Y_{21}}$ represent the mutual admittance matrix between set 1 and set 2.

Careful observation of the admittance matrix in equation (93) leads to the conclusion that all sub-matrices $\mathbf{Y_{ii}}$ are block circulant of circulant block matrices in nature with size 2n x 2n. It can also be observed that sub-matrix $\mathbf{Y_{12}} \neq \mathbf{Y_{21}}$.

Let the voltage and currents at 4n ports be represented by vectors $\mathbf{V}(p)$ and $\mathbf{I}(p)$ where p = 0, 1,...4n is the port index. In port space, and by using Kirchhoff's equations, the MTL structure is terminated with load admittance at both ends and can be represented as

$$\mathbf{V}(p) = \left(\widehat{\mathbf{Y}} + \mathbf{Y_L}\right)\mathbf{I}(p) \quad (94)$$

where $\mathbf{Y_L}$ is called the terminating admittance matrix of size 4n x 4n.

4.2.1 Block matrix algebra

For the subsequent analysis, a few definitions are in order.

Polynomial representor of a circulant matrix

The definition of a polynomial representor of the circulant is given by equation (95) [46]

$$p_\gamma(\omega) \quad = \quad c_1 + c_2\omega + c_3\omega^2 + \cdots + c_n\omega^{n-1} \tag{95}$$

where $[c_1,c_2,...c_n]^T$ is first row of circulant matrix.

Permutation matrix J

A permutation matrix is a square binary matrix that has exactly one entry of 1 in each row and each column and 0s elsewhere. Each such matrix represents a specific permutation of m elements and, when used to multiply another matrix, can produce that permutation in the rows or columns of the other matrix. A permutation matrix **J** or forward shift permutation matrix is a simple circulant matrix as defined by

$$\mathbf{J} \quad = \quad \begin{bmatrix} 0 & 1 & 0 & & 0 \\ 0 & 0 & 1 & \cdots & 0 \\ 0 & 0 & 0 & & 0 \\ & \vdots & & \ddots & \vdots \\ 1 & 0 & 0 & \cdots & 0 \end{bmatrix} \tag{96}$$

Circulant block matrix

A circulant block matrix can be written as [64]

$$\mathbf{A(J)} \quad = \quad \begin{bmatrix} \mathbf{a_{11}(J)} & \cdots & \mathbf{a_{1m}(J)} \\ \vdots & \ddots & \vdots \\ \mathbf{a_{m1}(J)} & \cdots & \mathbf{a_{mm}(J)} \end{bmatrix} \tag{97}$$

where $\mathbf{a_{kl}(J)}$ are the matrix polynomials of degree (n-1) given by

$$\mathbf{a_{kl}(J)} \quad = \quad \sum_{\boldsymbol{l=1}}^{\mathbf{n}} a_{\boldsymbol{kl}} \mathbf{J}^{\boldsymbol{l-1}} \tag{98}$$

where a_{kl} are the first row elements of the k^{th} block of a circulant block matrix **A** for k = 1 to m and l = 1 to n. **J** is a permutation matrix of length n x n.

Circulant block matrix eigenvalue computation

To compute the eigenvalues and the eigenvectors of a circulant block matrix efficiently, Rajsanow [64] has proposed the reduced dimension method. A mathematical description of the reduced dimension method is explained in next paragraphs.

4.2.2 Reduced dimension method

Lemma: Consider a matrix **A**(t), whose elements a_{kl}(t) are arbitrary functions of t, have $\lambda(t)$ as its eigenvalue, and y(t) as its eigenvector. Consider another matrix **B** with eigenvalue ω and eigenvector x. The matrix **A**(**B**) will have eigenvalue $\lambda(\omega)$, and its corresponding eigenvector will be $y(\omega) \otimes x$, where $\otimes$ is the Kronecker product [64].

To compute eigenvalues and eigenvectors of circulant block matrix $CB_{m,n}$ **A(J)** using the above Lemma, a permutation matrix **J** with eigenvalues ω and eigenvectors **X** is considered.

Eigenvalues of **A(J)** are the union of eigenvalues of n matrices $\mathbf{A}(\omega_p)$, where ω_p is the p^{th} eigenvalue of **J.** The element $A_{q,k}(\omega_p)$ of the matrix $\mathbf{A}(\omega_p)$ is the polynomial representor of the circulant block of matrix positioned at the k^{th} row and the q^{th} column of **A(J)**.

Eigenvalues ω_p of the J matrix are given by $\omega_p = e^{j(2\pi/n)(p-1)}$ with corresponding eigenvectors J_{eig}^{n}, which are given by $(\omega_p^0, \omega_p^1, \ldots, \omega_p^{n-1})^T$ $\forall$ p = 1 to n.

If **A(J)** is circulant block matrix $CB_{m,n}$ of size m x n i.e. m x m blocks, each block of order n, then matrix $\mathbf{A}(\omega_p)$ will be of size m x m for p = 1 to n.

If $\emptyset_q$ and $\mathbf{Y}(\omega_p)$ are the eigenvalue and corresponding eigenvector of $\mathbf{A}(\omega_p)$, then eigenvectors of matrix **A (J)** will be

$$\mathbf{Y}(\omega_p, \emptyset_{p,q}) \otimes \mathbf{X}(\omega_p) \; \forall \; p = 1 \text{ to } n \text{ , } q = 1 \text{ to } m \tag{99}$$

where $\mathbf{Y}(\omega_p, \emptyset_{p,q})$ is the q^{th} eigenvector of $\mathbf{A}(\omega_p)$, $\mathbf{X}(\omega_p)$ is the p^{th} eigenvector **J**

Single cyclic symmetrical structure

A single cyclic symmetrical structure can be defined as a structure which exhibits cyclic symmetry, and its elements satisfy the periodic condition $I_{m+n} = I_m \; \forall \; m = 1,2,..n$. An example of a single cyclic symmetrical structure is a symmetrical cyclic (n+1) MTL structure, which is primarily used for single resonant coils.

Double cyclic symmetrical structure

A double cyclic symmetrical structure can be defined as a structure which exhibits cyclic symmetry and contains two sets of elements and with elements in each set satisfying one of the periodic conditions $I_{m+n} = I_m \; \forall \; m = 1,3,..n$ and $I_{k+n} = I_k \; \forall \; k = 2,4,..n$. An example of a double cyclic symmetrical structure is an interleaved cyclic (2n+1) MTL structure, which is primarily used for dual resonant coils.

4.2.3 Eigenvalue determination using reduced dimension method

The case I: Single cyclic symmetrical structure

For a symmetrical cyclic (n+1) MTL structure, which is primarily used for single resonant coils [4], $(\widehat{\mathbf{Y}} + \mathbf{Y})$ is a block circulant matrix $BC_{m,n}$ where m = 2.

By using the reduced dimension method, $(\widehat{\mathbf{Y}} + \mathbf{Y_L})$ can be reduced into a set of n matrices $\widehat{\mathbf{Y}}(\omega_\mathrm{p})$ of size 2 x 2. Eigenvectors of $(\widehat{\mathbf{Y}} + \mathbf{Y_L})$ will be given by

$$\widehat{\mathrm{Y}}_{eig}(\omega_\mathrm{p}) \otimes \mathrm{J}^{n}_{\mathrm{eig}}(\omega_\mathrm{p}) \tag{100}$$

For equal terminations, the eigenvectors of $\widehat{\mathbf{Y}}(\omega_\mathrm{p})$ will be equal and are (α, α) and (α,-α) where α is a real constant. The complete set of eigenvectors will be

$$\begin{gathered}(\alpha^{*}\mathrm{J}^{n}_{\mathrm{eig}}(\omega_\mathrm{p}),\, \alpha^{*}\mathrm{J}^{n}_{\mathrm{eig}}(\omega_\mathrm{p})) \\ (\alpha^{*}\mathrm{J}^{n}_{\mathrm{eig}}(\omega_\mathrm{p}),\, -\alpha^{*}\mathrm{J}^{n}_{\mathrm{eig}}(\omega_\mathrm{p}))\end{gathered} \tag{101}$$

From the above result, it can be seen that eigenvectors exhibit λ/2 open and λ/2 short resonance conditions.

Case II: Double cyclic symmetrical structure

As described in earlier sections, most of the multi-tuned MTL coils designed using either interleaved conductors or interleaved terminations or both, result in a matrix $(\hat{\mathbf{Y}} + \mathbf{Y_L})$ which is a block circulant matrix $BC_{m.n}$, where m = 4. As mentioned in the above sections, using the reduced dimension method, $(\hat{\mathbf{Y}} + \mathbf{Y})$ can be reduced into a set of n matrices $\hat{\mathbf{Y}}(\omega_{\mathrm{p}})$ of size 4 x 4. If similar terminations are used on both ends, the reduced matrix $\hat{\mathbf{Y}}(\omega_{\mathrm{p}})$ will be a block circulant matrix $BC_{m.n}$ where m = 2 and n = 2.

Furthermore, using the reduced dimension method, $\hat{\mathbf{Y}}(\omega_{\mathrm{p}})$ can be reduced into two matrices $\hat{\mathbf{Y}}^{\mathbf{new}}(\omega_{\mathrm{p}},\delta_{\mathrm{q}})$ of dimension 2 x 2, where p = 1 to n , q = 1 to 2 and ω_{p} is the p$^{\mathrm{th}}$ eigenvalue of the n x n sized **J** matrix and δ_q is the q$^{\mathrm{th}}$ eigenvector of the 2 x 2 sized **J** matrix.

The eigenvectors of $(\hat{\mathbf{Y}} + \mathbf{Y})$ will be given by

$$\hat{\mathrm{Y}}_{eig}^{\mathrm{new}}(\omega_{\mathrm{p}},\delta_q) \otimes \mathrm{J}_{\mathrm{eig}}^{2}(\delta_q) \otimes \mathrm{J}_{\mathrm{eig}}^{n}(\omega_{\mathrm{p}}) \tag{102}$$

For the permutation matrix **J** of order 2, the eigenvalues are (1,-1) and the corresponding eigenvectors are $(\sqrt{2},\sqrt{2})$ and $(-\sqrt{2},\sqrt{2})$

The eigenvectors of $(\hat{\mathbf{Y}} + \mathbf{Y_L})$ can be further reduced to

$$\begin{aligned} &\hat{\mathrm{Y}}_{eig}^{\mathrm{new}}(\omega_{\mathrm{p}},1) \otimes \sqrt{2}\left[\ \mathrm{J}_{\mathrm{eig}}^{n}(\omega_{\mathrm{p}})\ \mathrm{J}_{\mathrm{eig}}^{n}(\omega_{\mathrm{p}})\ \right]^{T} \\ &\hat{\mathrm{Y}}_{eig}^{\mathrm{new}}(\omega_{\mathrm{p}},-1) \otimes \sqrt{2}\left[-\mathrm{J}_{\mathrm{eig}}^{n}(\omega_{\mathrm{p}})\ \mathrm{J}_{\mathrm{eig}}^{n}\omega_{\mathrm{p}}\ \right]^{T} \end{aligned} \tag{103}$$

If ($a_{(\omega_{\mathrm{p}}),\mathrm{q}}^{1}$, $b_{(\omega_{\mathrm{p}}),\mathrm{q}}^{1}$) and ($a_{(\omega_{\mathrm{p}}),\mathrm{q}}^{2}$, $b_{(\omega_{\mathrm{p}}),\mathrm{q}}^{2}$) are the eigenvectors of $\hat{\mathrm{Y}}_{eig}^{\mathrm{new}}(\omega_{\mathrm{p}},\mathrm{q})$ then the complete eigenvector set would be

$$\begin{aligned} &\sqrt{2}\left[\ a_{(\omega_{\mathrm{p}}),1}^{1}\cdot \mathrm{J}_{\mathrm{eig}}^{n}(\omega_{\mathrm{p}})\ a_{(\omega_{\mathrm{p}}),1}^{1}\cdot \mathrm{J}_{\mathrm{eig}}^{n}(\omega_{\mathrm{p}})\ b_{(\omega_{\mathrm{p}}),1}^{1}\cdot \mathrm{J}_{\mathrm{eig}}^{n}(\omega_{\mathrm{p}})\ \ b_{(\omega_{\mathrm{p}}),1}^{1}\cdot \mathrm{J}_{\mathrm{eig}}^{n}(\omega_{\mathrm{p}})\ \right]^{T} \\ &\sqrt{2}\left[\ a_{(\omega_{\mathrm{p}}),1}^{2}\cdot \mathrm{J}_{\mathrm{eig}}^{n}(\omega_{\mathrm{p}})\ \ a_{(\omega_{\mathrm{p}}),1}^{2}\cdot \mathrm{J}_{\mathrm{eig}}^{n}(\omega_{\mathrm{p}})\ \ b_{(\omega_{\mathrm{p}}),1}^{2}\cdot \mathrm{J}_{\mathrm{eig}}^{n}(\omega_{\mathrm{p}})\ \ b_{(\omega_{\mathrm{p}}),1}^{2}\cdot \mathrm{J}_{\mathrm{eig}}^{n}(\omega_{\mathrm{p}})\ \right]^{T} \end{aligned} \tag{104}$$

$$\sqrt{2}\left[-a^{1}_{(\omega_p),-1}\cdot \mathrm{J}^{n}_{\mathrm{eig}}(\omega_p)\ \ a^{1}_{(\omega_p),-1}\cdot \mathrm{J}^{n}_{\mathrm{eig}}(\omega_p)\ -b^{1}_{(\omega_p),-1}\cdot \mathrm{J}^{n}_{\mathrm{eig}}(\omega_p)\ \ b^{1}_{(\omega_p),-1}\cdot \mathrm{J}^{n}_{\mathrm{eig}}(\omega_p)\ \right]^{T}$$

$$\sqrt{2}\left[-a^{2}_{(\omega_p),-1}\cdot \mathrm{J}^{n}_{\mathrm{eig}}(\omega_p)\ \ a^{2}_{(\omega_p),-1}\cdot \mathrm{J}^{n}_{\mathrm{eig}}(\omega_p)\ -b^{2}_{(\omega_p),-1}\cdot \mathrm{J}^{n}_{\mathrm{eig}}(\omega_p)\ \ b^{2}_{(\omega_p),-1}\cdot \mathrm{J}^{n}_{\mathrm{eig}}(\omega_p)\ \right]^{T}$$

4.2.4 Condition for multiple resonances

A double cyclic symmetrical structure can be tuned for a double resonance by using two terminations of different values in the load admittance matrix. Those two unknown values are found by solving the eigenvalue equations at the required two frequencies.

4.2.5 Port current distribution

Once the termination admittances are calculated, then by using the KVL equation, the current at each port is computed. By using the chain parameter matrix, the port currents, and the port voltages on ports located at one end (preferably z = 0) of the MTL as well as the current distribution along the length of the coil can be calculated by the following equation.

$$\mathbf{I}(z) \quad = \quad \mathbf{\Phi_{21}}(\mathrm{z})\cdot \mathbf{V}(0) + \ \mathbf{\Phi_{22}}(\mathrm{z})\cdot \mathbf{I}(0) \qquad (105)$$

After obtaining the current distribution along the length of the coil, the field distribution can be computed using Biots-Savart's law.

4.3 Simulation results and validation

In this dissertation, a closed form solution for the resonant condition of an eigenvalue problem is presented for two cases: I) single cyclic structure and II) double cyclic structure. A standard single tuned MTL coil is treated and analyzed using both of these cases.

4.3.1 Single resonant MTL coil

The proposed reduced dimension method is employed to analyze a small coil described in [4]. The analyzed results are then compared with the published results. The small coil described in [4] has an inner diameter of 7.25 cm and an outer diameter of 10.5cm. The coil is 15.25 cm long and has 12 copper strips of 6.4 mm

wide as elements. Open port admittance matrix is computed at the required frequency of 200MHz using HFSS driven terminal solver as mentioned in previous chapters.

The small coil is treated as a single cyclic structure, and its generated open port admittance matrix represents a BCCB matrix. The required resonant conditions are then computed using the reduced dimension method. A 10.52 pF value is the required capacitance for resonating the small coil at 200 MHz, and the result agrees well with the published result [4].

The open circuit admittance matrix is then rearranged to form an interleaved design (representing a double cyclic structure). This rearrangement transforms the open port admittance matrix into a CB matrix The termination capacitance value remained the same when the small coil is treated as a double cyclic structure, validating the algorithm and its implementation.

4.3.2 Dual resonant structure

Based on the proposed reduced dimension method, two new dual tuned head coils A) phosphorus-31 (165.09 MHz) and sodium-23 (105.9 MHz) B) sodium-23(105.9 MHz) and oxygen-17(54.3MHz) for a 9.4T human imaging scanner are simulated and developed. For convenience, the phosphorus-31 and sodium-23 coil is called P_{31}- Na_{23} coil and the sodium-23 and oxygen-17 coil is referred to as $Na_{23} - O_{17}$ coil.

4.3.3 Coil description

Both the P_{31}- Na_{23} coil and the $Na_{23} - O_{17}$ coil are identically interleaved designs. The complete structure has two sets of conductors and a shield element. Table 4 shows the dimensions of the proposed coils. The coils were built using two clear acrylic tubes. The inner tube is of dimensions 6.5 inches in length, 0.25 inches wall thickness, and ID of 9.5 inches. The outer tube has an outer diameter of 12.5 inches with a wall thickness of 0.25 inches, and a length of 6.5 inches. Both the tubes are concentric and are attached by acrylic endplates of thickness 0.25 inches on both the ends, which are machined to hold the PCB's.

Table 4: Dimensions of the proposed dual tuned head coils.

Parameter	P_{31}- Na_{23}	Na_{23} – O_{17}
Length of Coil	7 in (152.4 mm)	7 in (152.4 mm)
Inner Diameter of coil	9.5 in	9.5 in
Middle Strip diameter	10 in	10 in
Outer Diameter of coil	12.5 in	12.5 in
Number of Inner Strips	12	12
Number of Outer Strips	12	12
Width of inner Strips	1.67 in	0.567 in
Width of middle strips	1.67 in	0.567 in
Resonant High frequency	Phosphorus (P^{31}) 162.09 MHz	Sodium(Na^{23}) 105.9 MHz
Resonant Low frequency	Sodium (Na^{23}) 105.9 MHz	Oxygen (O^{17}) 54.3MHz

Twelve copper strips of width 1.617 inches are glued to the inner surface of the inner tube, and 12 more copper strips of width 0.567 inches are glued to the outer surface of the inner tube. The outer strips are aligned with inner strips without any rotation angle between them. All the copper strips are of length 7 inches and are connected to the front and back of the PCBs using a conductive epoxy. A slotted copper sheet interconnected with 820 pF value capacitors is wrapped around the outer surface of the outer tube. The slotted copper sheet is connected to the PCBs and is designed to act as a ground plane to the microstrips. The left side image of Fig.26 shows the arrangements of the elements and the shield. The right side image of Fig.26 illustrates the coil with an endplate and a PCB board.

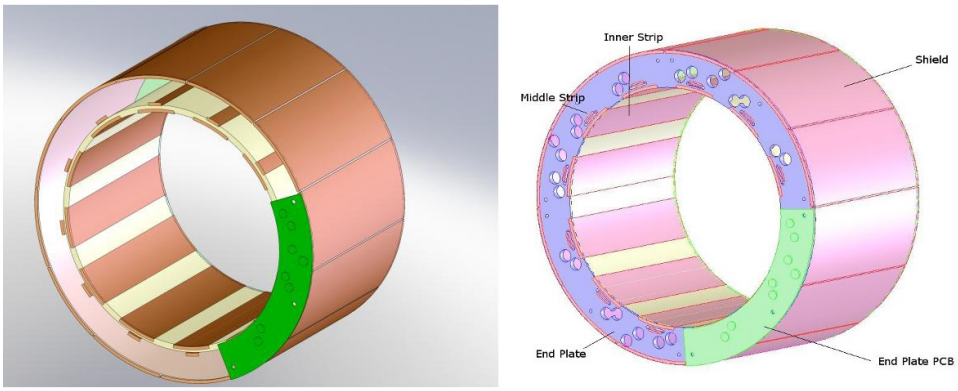

Fig.26: 3D CAD representation of the constructed dual tuned head coil.

4.3.4 Construction:

The construction method for the proposed coil involves two printed circuit boards (PCBs) attached to the acrylic end plates used to join the inner and the outer former. These circuit boards house most of the components including the connectors, terminating components and matching networks. Variable capacitors (55H02C, Johansson manufacturing) and chip capacitors (ATC 100C series) are used as termination and matching capacitors. An adhesive backed copper foil is used to create the shield and the elements. Shown in Appendix A are the PCB layouts. List of the components used are given in Appendix B.

The construction procedure for the coil is as follows.

- Layout the copper strips on the inner and outer sides of the inner former
- Attach the end plates joining the inner and the outer formers
- Layout the copper strips on the outer sides of the outer former
- Install the PCBs on to the end plates using an adhesive epoxy
- Solder the components on PCBs and wrap the coil with a protective Kapton sheet

Fig.27 shows the photograph of the constructed coil.

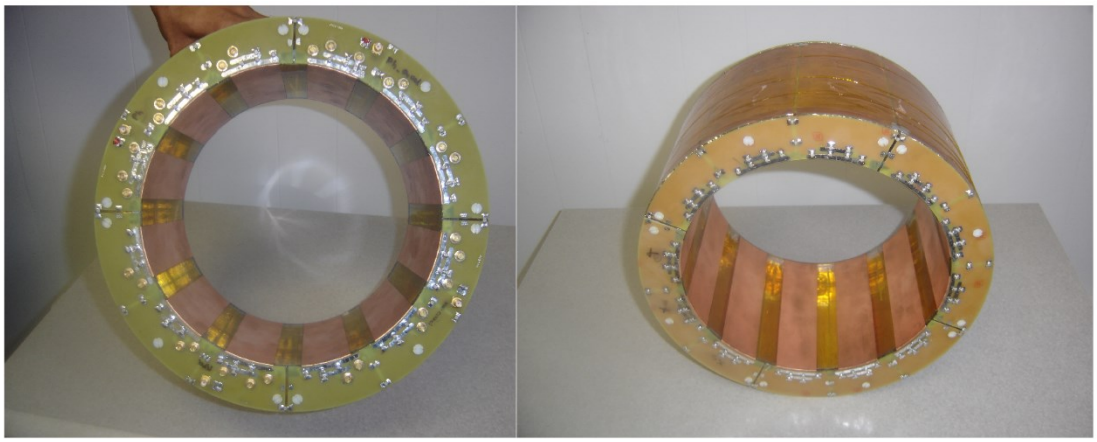

(a) (b)

Fig.27: Photographs of the constructed dual tuned head coil (a) Back end plate, (b) Front end plate.

4.3.5 Port admittance matrix characteristics

Similar to early presented coil simulations, a full-wave 3D EM simulations were performed using the HFSS-driven terminal solver [49] to generate the open-circuit admittance matrix. While simulating the open-circuit admittance matrix $\widehat{\mathbf{Y}}$, ports of the wider strip at the location $z = 0$ are numbered from 1-12 and the corresponding ports at the location $z = l$ are numbered from 13-24. Similarly, ports of the narrow strip at the location $z = 0$ are numbered from 25-36 and the corresponding ports at the location $z = l$ are numbered from 37-48. The open-circuit admittance matrix $\widehat{\mathbf{Y}}$ is a 48 by 48 element matrix

The matrix $\widehat{\mathbf{Y}}$ is a 2 X 2 block matrix, with each block again being a 2 by 2 block matrix. Further observation of the matrix $\widehat{\mathbf{Y}}$ shows that it is a 4 X 4 block matrix with each block being a 12 element circulant matrix. The matrix $\widehat{\mathbf{Y}}$ is shown as

$$\widehat{\mathbf{Y}} = \begin{bmatrix} \begin{vmatrix} \mathbf{Y_{AA}} & \mathbf{Y_{AB}} \\ \mathbf{Y_{BA}} & \mathbf{Y_{BB}} \end{vmatrix} & \begin{vmatrix} \mathbf{Y_{AC}} & \mathbf{Y_{AD}} \\ \mathbf{Y_{BC}} & \mathbf{Y_{BD}} \end{vmatrix} \\ \begin{vmatrix} \mathbf{Y_{CA}} & \mathbf{Y_{CB}} \\ \mathbf{Y_{DA}} & \mathbf{Y_{DB}} \end{vmatrix} & \begin{vmatrix} \mathbf{Y_{CC}} & \mathbf{Y_{CD}} \\ \mathbf{Y_{DC}} & \mathbf{Y_{DD}} \end{vmatrix} \end{bmatrix} \quad (106)$$

where A represents the set of ports numbered from 1 to 12, B represents the set of ports numbered from 13 to 24, represents the set of ports numbered from 25 to 36 and D represents the set of ports numbered from 37 to 48.

The port set A, and the port set B are chosen to be on the same set of elements, so they tend to be identical. Similarly, port sets C and D are also identical. The above conditions lead to the following identities

$$\mathbf{Y_{AA} = Y_{BB}}\,, \quad \mathbf{Y_{AB} = Y_{BA}}\,, \quad \mathbf{Y_{CC} = Y_{DD}}\,, \quad \mathbf{Y_{CD} = Y_{DC}}$$

$$\mathbf{Y_{AC} = Y_{BD}}\,, \quad \mathbf{Y_{AD} = Y_{BC}}\,, \quad \mathbf{Y_{CA} = Y_{DB}}\,, \quad \mathbf{Y_{CB} = Y_{DA}}$$

One important point that becomes evident here is that

$$\mathbf{Y_{AC} \neq Y_{CA}} \text{ but } \mathbf{Y_{AC} = Y'_{CA}} \text{ and } \mathbf{Y_{CB} \neq Y_{AD}} \text{ but } \mathbf{Y_{CB} = Y'_{AD}}$$

The above observations are important because they make the matrix $\widehat{\mathbf{Y}}$ a *CB* matrix rather than a *BCCB*. The matrix $\widehat{\mathbf{Y}}$ is a *CB* matrix, and it cannot be diagonalized by Kronecker product operators and need a more powerful technique like reduced dimension method.

As termination conditions, all the wide strips are terminated with an admittance of Y_{T1} and all the narrow strips with an admittance of Y_{T2}. An admittance of Y_T was connected between the strips. Admittance of any lumped element connected between two ports gets added to the self-admittance of the ports and gets subtracted with the mutual admittance between ports [65]. The resultant termination matrix $\widehat{\mathbf{Y}}_L$ is given by

$$\mathbf{Y_L} = \begin{bmatrix} \mathbf{Y_{T1} + Y_T} & \mathbf{0} & \mathbf{-Y_T} & \mathbf{0} \\ \mathbf{0} & \mathbf{Y_{T1} + Y_T} & \mathbf{0} & \mathbf{-Y_T} \\ \mathbf{-Y_T} & \mathbf{0} & \mathbf{Y_{T2} + Y_T} & \mathbf{0} \\ \mathbf{0} & \mathbf{-Y_T} & \mathbf{0} & \mathbf{Y_{T2} + Y_T} \end{bmatrix} \tag{107}$$

To resonate the coil at dual frequency, the port admittance matrix ($\widehat{\mathbf{Y}} + \mathbf{Y_L}$) is written for two frequencies, and its determinant is solved simultaneously at both frequencies. Careful observation reveals that there are three variables Y_{T1}, Y_{T2}, and Y_T but only two equations to solve. For all our simulations Y_T is assumed with a given fixed value, and Y_{T1} and Y_{T2} are then determined.

4.3.6 Phosphorous-31 - Sodium-23 coil

The prototype P_{31}- Na_{23} coil was designed to resonate at 165.09 MHz (resonant frequency of phosphorus nuclei at 9.4T) and 105.9 MHz (resonant frequency of sodium nuclei at 9.4T). By applying the reduced dimension method, the following required capacitances are predicted. The capacitance between the inner strip (wider strip) and the shield is 12.5 pF, between the middle strip (narrow strip) and the shield is 31.24 pF and between the wide strip and the narrow strip is 30 pF.

The coil was manufactured using the previously explained construction procedure. The coil was populated with the predicted component values, and it is tuned and matched for the correct frequencies. The coil was designed for a quadrature operation at both frequencies. An Agilent 8713C network analyzer was used for testing the coil resonance modes, the isolation between two quadrature ports, and matching at phosphorus and sodium channels.

Fig.28 shows the reflection coefficient S_{11} for both the sodium channels which is better than -18dB at the required frequency of 105.9MHz. Fig.28 also shows the isolation S_{21} between the quadrature ports at 105.9MHz, and it is less than -23dB. Similarly, the reflection coefficient S_{11} for both the phosphorus channels is observed to be less than -18dB at the required frequency of 162.09MHz. Fig.28 (d) shows the isolation S_{21} between the quadrature ports at 162.09MHz to be less than -23dB. Similarly, the average isolation between different nuclei channels is less than -21dB, which is further improved by using filter networks. Even though the presented results are for an unloaded coil, it was observed that for a standard human head size loading, a phantom filled with a NaCl solution, the coils display similar tuning and matching patterns.

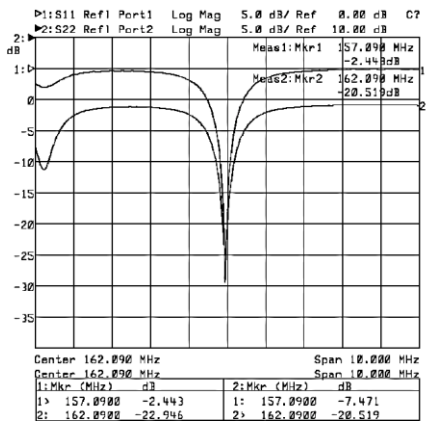

(a)

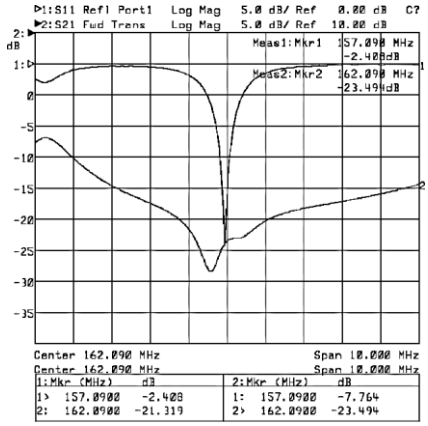

(b)

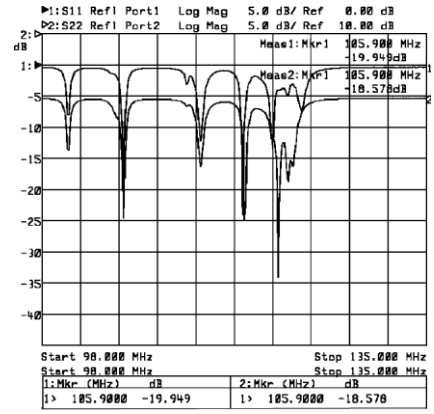

(c)

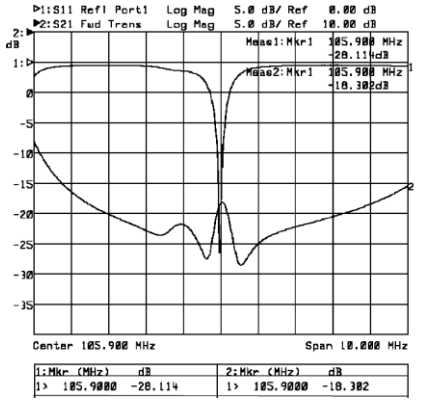

(d)

Fig.28: S-parameter coefficient measurement of the P_{31}- Na_{23} coil with network analyzer: (a) Magnitude of input reflection coefficient (S_{11}) of sodium channel, (b) Magnitude of isolation coefficient (S_{21}) between quadrature sodium channels, (c) Magnitude of input reflection coefficient (S_{11}) of phosphorus channel, (d) Magnitude of isolation coefficient (S_{21}) between quadrature phosphorus channels.

4.3.7 Sodium-23 and Oxygen-17 coil

Similarly, one more prototype coil was tuned to 105.9 MHz to image sodium nuclei and to 54.3MHz to image oxygen nuclei at 9.4T. Predicted capacitances using the reduced dimension method are as follows: Capacitance between the inner strip (wider strip) and the shield is 14.56 pF, and between the middle strips (narrow strip) to the shield is 138.6 pF. The required capacitance between the wide strips to the narrow strip is 62 pF. For the constructed coil, the measured S-parameters are shown in Fig.29. The reflection

measurements (S_{11}) for the sodium channels are less than -30dB, and for the oxygen channels, the S_{11} are less than -21db. The isolation (S_{12}) between the sodium channels is less than -35db, and for the oxygen channels, it is less than -29dB. The average isolation between the sodium and the oxygen channels is less than -21dB.

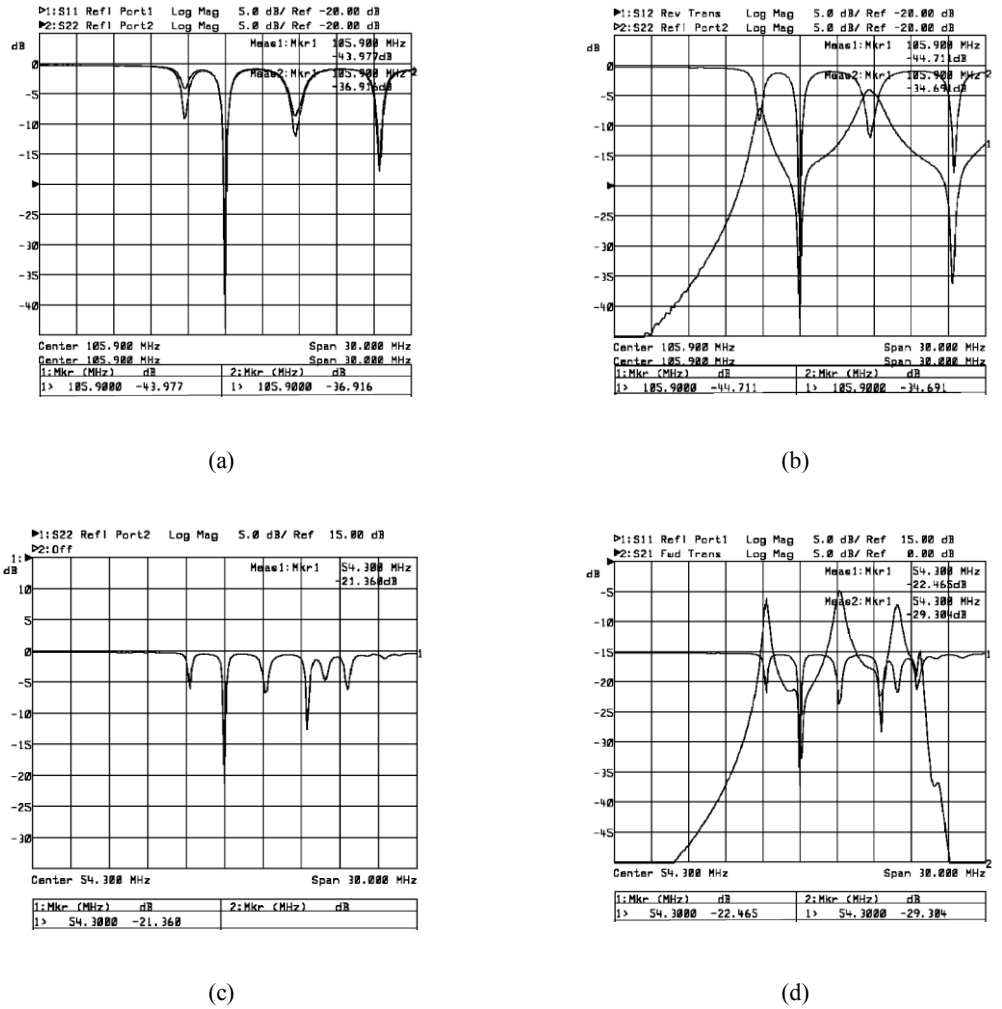

Fig.29: S-parameter coefficient measurement of the $Na_{23} - O_{17}$ coil with network analyzer: (a) Magnitude of input reflection coefficient (S_{11}) of sodium channel, (b) Magnitude of isolation coefficient (S_{21}) between quadrature sodium channels, (c) Magnitude of input reflection coefficient (S_{11}) of oxygen channel, (d) Magnitude of isolation coefficient (S_{21}) between quadrature oxygen channels.

4.3.8 HFSS simulations

HFSS eigenmode simulations are performed to validate the resonant conditions predicted by the reduced dimension method. Fig.30 shows the simulated normalized H-field plots in the axial plane for the high frequency and the low frequency for both the P_{31}- Na_{23} and the $Na_{23} - O_{17}$ coils. From the Fig.30 it can be seen that at the low frequency, currents on both the narrow and the wide strips are in phase. At high frequency, the currents are in opposite phase; the opposite phase can be deduced from the presence of null spots below the narrow strips. Currents opposite phase is further validated by the port current simulation using the reduced dimension method.

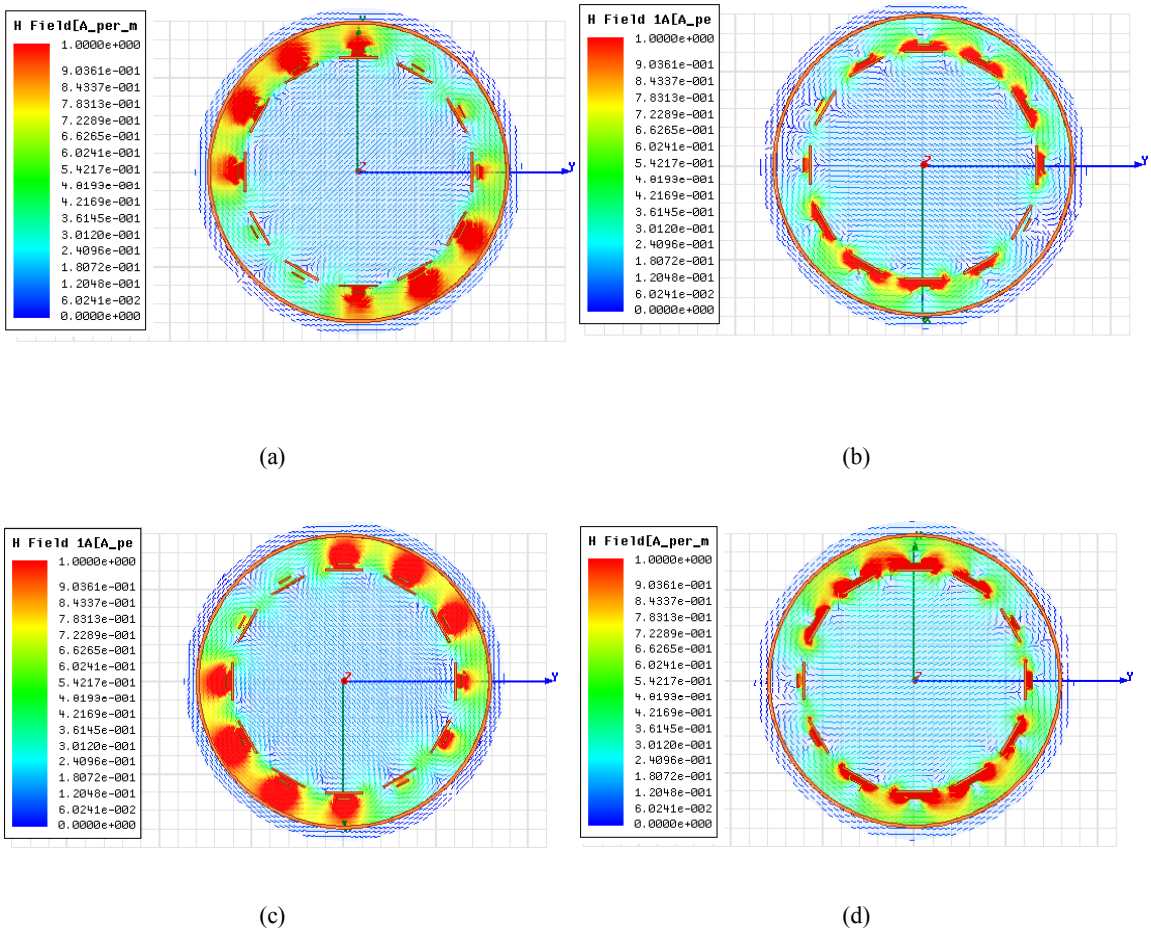

Fig.30: HFSS simulated axial magnetic field plots at the center of coil represented with overlapped vector and magnitude plots for a linearly driven: a) Oxygen channel of the $Na_{23} - O_{17}$ coil b) Sodium channel of the $Na_{23} - O_{17}$ coil c) Sodium channel of the P_{31}- Na_{23} coil d) Phosphorus channel of the P_{31}- Na_{23} coil. All plots are normalized to a maximum H field value.

4.3.9 Off-diagonal terminations

Most of the existing designs optimize the mode separation and the field profiles by varying the residual coupling between the conductors. Mode separation is achieved either by the optimization of geometrical position of the conductors or by careful selection of the conductor dimensions. In this work, the residual coupling between the conductors is varied by using the lumped components between the elements, which will remove the restrictions on coil geometry and the conductor positioning.

4.3.10 Effect of off-diagonal terminations on required termination values

A lumped capacitor is used between the wide and the narrow strip to manipulate the self and the mutual admittance between the strips. Fig.31 shows the termination capacitor values on a wider strip, and on a narrow strip as a function of lumped capacitor value between the strips. From Fig.31 it can be seen that the interconnecting capacitor has a minimum and a maximum value. Outside the range, the termination component values become complex which can only be realized with resistive and reactive components, thereby increasing the coil losses. Terminations with negative capacitances are realized with inductors to obtain the required admittance. Table 5 shows the termination values for some chosen inter-strip capacitance values.

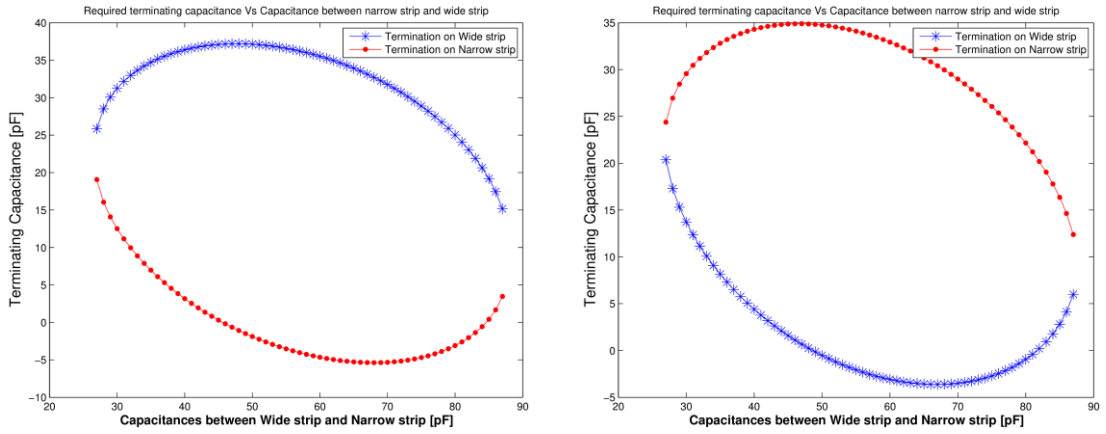

(a) (b)

Fig.31: Termination values for the P_{31}- Na_{23} coil as a function of capacitor values in between narrow and wide strip. (a) Wide strips are terminated with high impedance and narrow strips with low impedance. (b) Narrow strips with high impedance and wide strips with low impedance.

Table 5: Termination values for the P_{31}- Na_{23} coil as a function of lumped capacitor values in between narrow and wide strips

Wide strip termination	Narrow strip termination	Interconnecting capacitance between the wide strip and narrow strip
12.5 pF	31.24 pF	30 pF
6.95 pF	34.71 pF	35 pF
3.16 pF	36.38 pF	40 pF
-0.18 pF	37.15 pF	46 pF
-3.52 pF	25.89 pF	79 pF
3.46 pF	15.15 pF	87 pF

Fig.32 shows the HF mode port currents for the P_{31}- Na_{23} coil for different capacitor values between the narrow and the wide strips. Similarly, Fig.33 shows the LF mode port currents for P_{31}- Na_{23} coil for various capacitor values between the narrow and the wide strips. The Interconnecting capacitance capacitor value is chosen such that the port currents are optimized to give an optimal magnetic field.

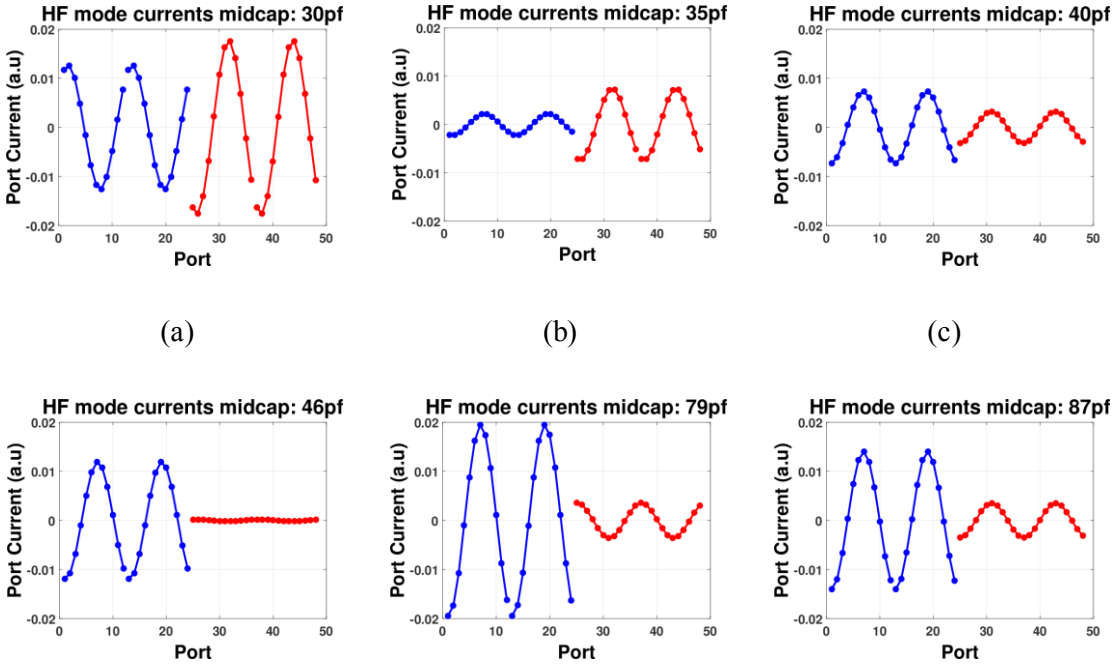

Fig.32: HF mode port currents for the P_{31}- Na_{23} coil for different capacitor values between narrow and wide strips (a) for 30 pF (b) for 35 pF (c) for 40 pF (d) for 46 pF (e) for 79 pF (f) for 87 pF.

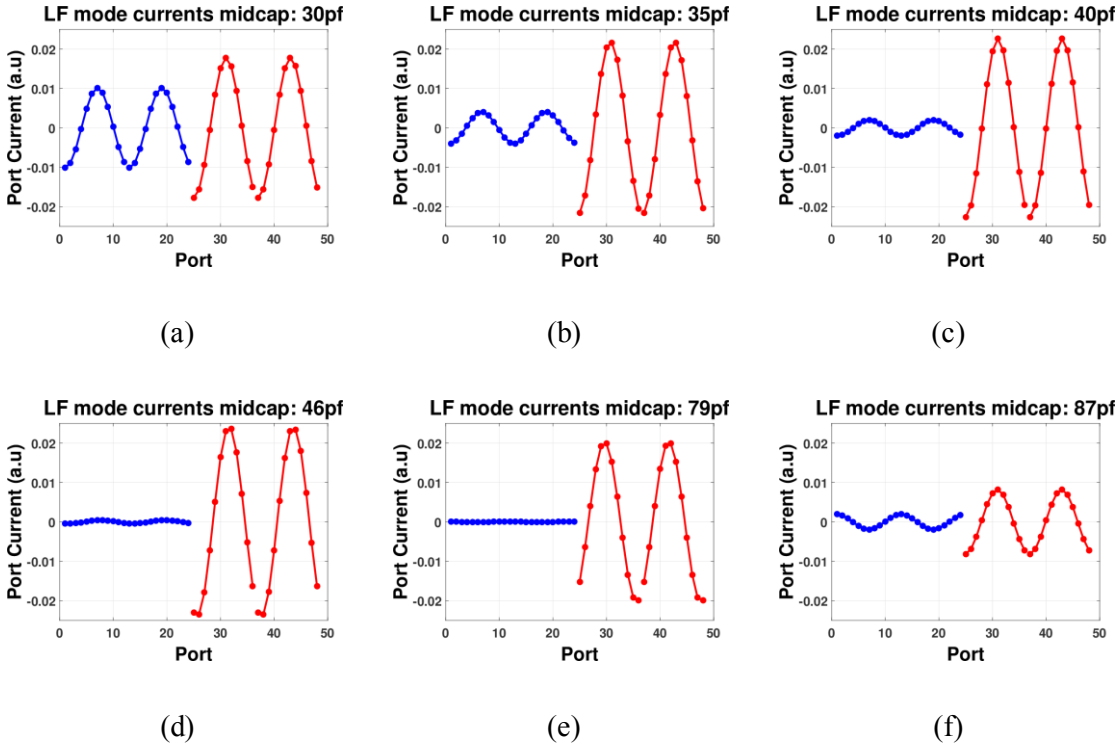

Fig.33: LF mode port currents for the P_{31}- Na_{23} coil for different capacitor values between narrow and wide strips (a) for 30 pF (b) for 35 pF (c) for 40 pF (d) for 46 pF (e) for 79 pF (f) for 87 pF.

4.4 MRI validation

The designed coils were tested on phantoms in a 9.4T human MRI scanner. The 9.4T scanner magnet (GE Healthcare, Abingdon, UK) has a clear magnet bore of 80 cm and is equipped with a head gradient set (GE Healthcare, Abingdon, UK and Florence, SC; amplifiers by Copley Controls Corp., Canton, MA) and high-order shim set (GE Healthcare, Abingdon, UK and Florence, SC; amplifiers by Resonance Research, Inc., Billerica, MA) that result in a bore access of 36 cm at isocenter, widening to 80 cm at 18 cm from isocenter. The operator interface and control electronics (Bruker Biospin, Billerica, MA) provide full proton and non-proton imaging.

4.4.1 Phantom details for coil validation

For MR imaging experiments two phantoms are used. The first phantom is "Braino" phantom (GE Medical Systems, Milwaukee, WI, USA), containing 12.5 mM of N-acetyl-L-aspartic acid [NAA], 10 mM of

creatine hydrate [Cr], 3 mM of choline chloride [Ch], 7.5 mM of Myo-inositol [mI], 12.5 mM of L-glutamic acid [Glu], 5 mM of DL-lactic acid [Lac], sodium azide (0.1%), 50 mM of potassium phosphate monobasic [KH_2PO_4], 56 mM of sodium hydroxide [NaOH] and 1 mL/L of Gd-DPTA [Magnevist].

The second phantom consisted of three sealed cylindrical tubes (3 cm diameter) containing different sodium concentrations (30, 70, 110 mM), enclosed within a sphere (16 cm diameter) containing 60mM potassium chloride to match the electrical loading of a human head while minimizing the magnetic susceptibility effects from the cylindrical tubes. The tubes were made up of 3% agar to closely match T2 values to the *in vivo* tissue values.

4.4.2 B_0 homogeneity and shimming

Magnetic field homogeneity was maximized by manual adjustment of linear and high order room temperature shims to minimize the full width at half-maximum (FWHM) of the whole field-of-view spectrum. FWHM is a measure of the width at the half the maximum value of peaked functions such as spectral lines or slice profiles. In this case, the spectral line shape describes the distribution of the relative strength of resonance as a function of frequency, which establishes a particular spectral line. Fig.34 shows the achieved line shapes for different channels of the designed coils on the above-mentioned phantoms. Table 6 shows the manually shimmed B_o homogeneity values in terms of FWHM. All the values are acceptable, and the results prove that coils are not inducing any B_0 inhomogeneity.

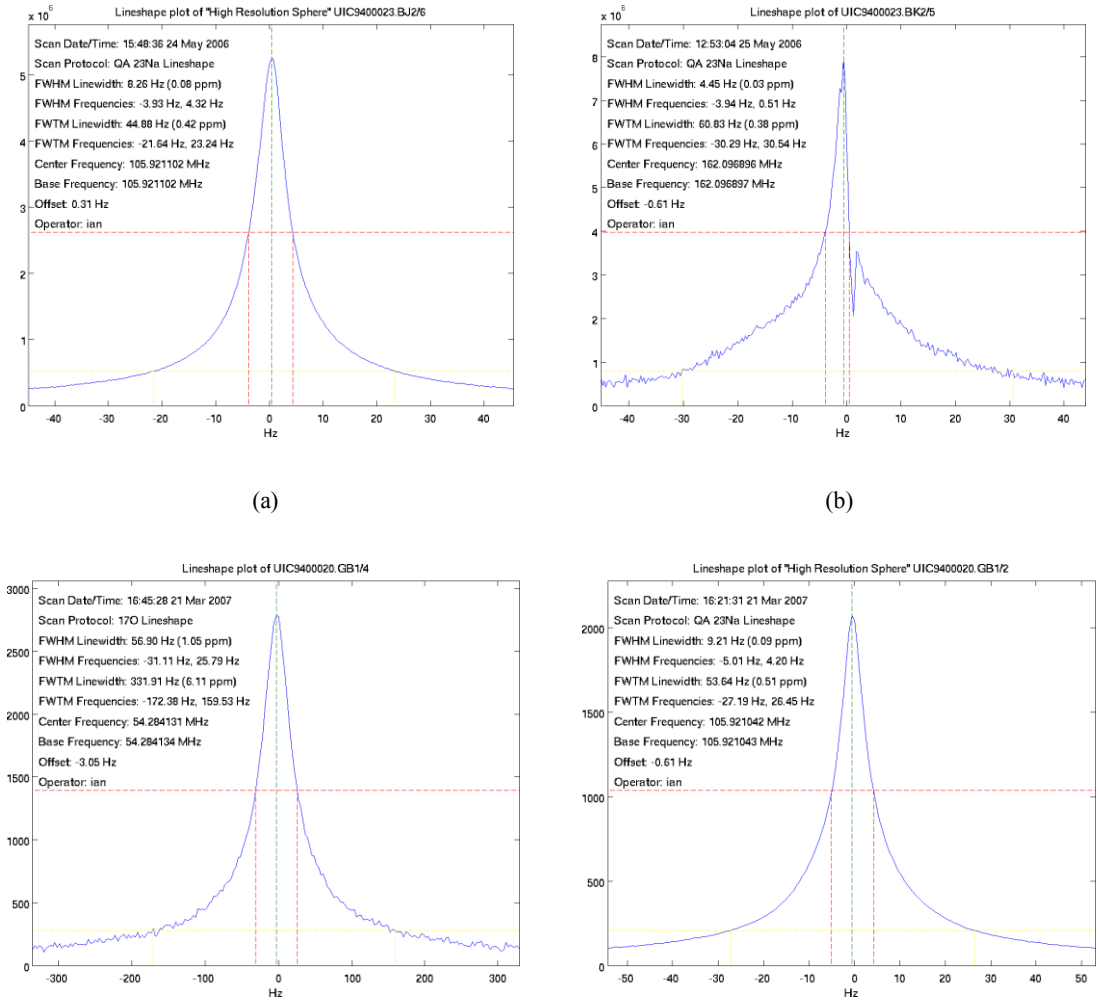

Fig.34: Line shape of different spectrums : (a) Sodium channel of the P_{31}- Na_{23} coil (b) Phosphorus channel of the P_{31}- Na_{23} coil (C) Oxygen channel of the $Na_{23} – O_{17}$ coil (d) Sodium channel of $Na_{23} – O_{17}$ coil.

Table 6: Manually shimmed B_o homogeneity values in terms of FWHM

	Na_{23} Channel	P_{31} Channel	O_{17} Channel
$P_{31} – Na_{23}$ Coil	8.26 Hz / 0.08 ppm	4.45 Hz/0.03 ppm	
$Na_{23} – O_{17}$ Coil	9.21 Hz/0.09 ppm		56.90 Hz/1.05 ppm

4.4.3 Sodium imaging

Sodium images are obtained using the sodium channel of P_{31}- Na_{23} coil and the $Na_{23} - O_{17}$ coil. The acquired sodium images are compared with sodium images acquired using custom built single resonant birdcage coil. For convenience, the custom-built single resonant birdcage coil is called "CMRR coil". For imaging a twisted projection imaging (TPI) sequence is used with parameters TE/TR = 0.4/175 msec, FOV = 200 mm x 200mm x 200mm, maximum gradient amplitude = 4mT/m, radial fraction = 0.2, total rings = 62, total trajectories=1028, K_{Max} = 100, K_0 = 20, maximum gradient slew rate = 196.0 mT/m/msec, to give a 3mm isotropic resolution, number of averages = 1 and number of repetitions = 2.

Fig.35 shows the comparison of sodium images obtained from CMRR single resonant sodium coil and from sodium channel of $Na_{23} - O_{17}$ coil. The images are acquired as axial slices of the second phantom. Comparing mean SNR measurements of sodium on both coils, it is clear that the single resonant coil performs 26% better than the dual resonant coil.

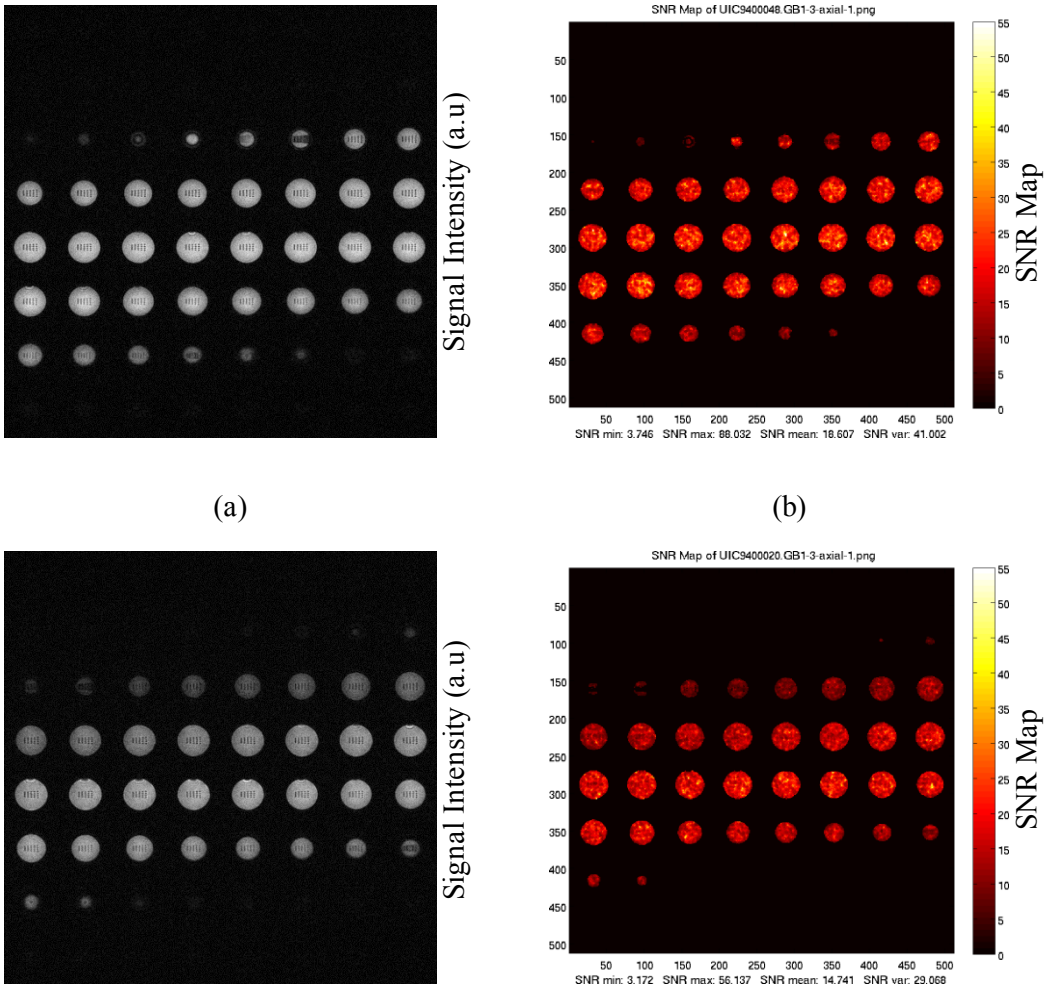

Fig.35: (a) Signal intensity in arbitrary units (a.u.) image of CMRR single tuned sodium coil (b) signal-to-noise (SNR) distribution map of CMRR single tuned sodium coil (c) Signal intensity (a.u.) image of sodium channel of $Na_{23} - O_{17}$ coil (d) signal-to-noise(SNR) distribution map of sodium channel of $Na_{23} - O_{17}$ coil.

Fig.36 and Fig.37 display the comparison of the sodium images for different coils. Individual figures in each image represent different slices of the Braino phantom. Mean SNR measurements exhibit consistency between the slices for all coils. Comparing the mean SNR measurements of sodium as a high-frequency channel in the $Na_{23} - O_{17}$ coil and as a low-frequency channel in the P_{31}- Na_{23} coil demonstrates that the proposed coil has identical efficiencies for sodium. When compared with the single resonant CMRR coil, the proposed coils exhibits similar SNR.

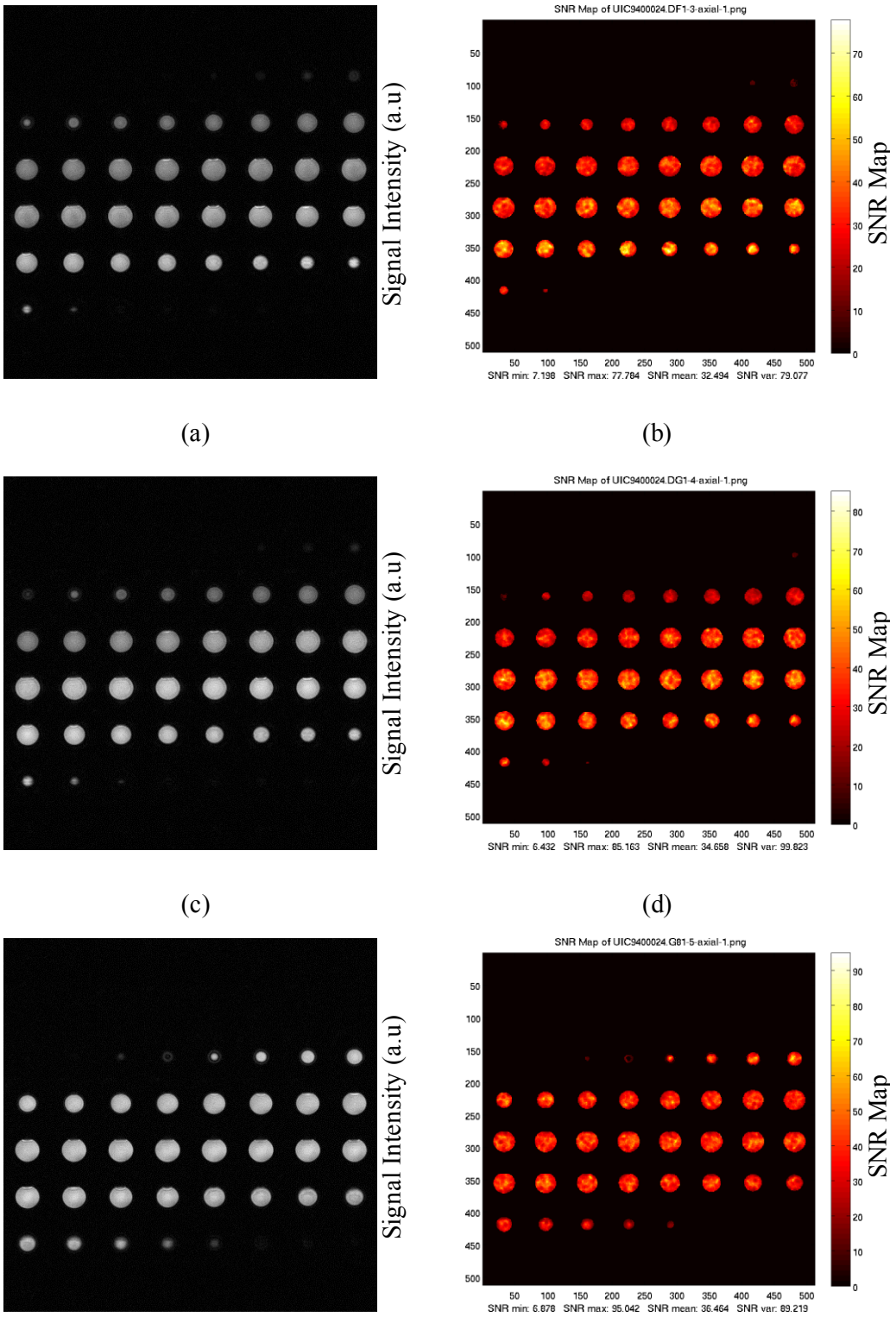

Fig.36: Comparison of center slice 1 for (a) Signal intensity in arbitrary units (a.u.) image and (b) SNR map of sodium channel of P_{31}- Na_{23} coil. (c) Signal intensity (a.u.) image and (d) SNR map of sodium channel of sodium channel of $Na_{23} - O_{17}$ coil. (e) Signal intensity (a.u.) image and (f) SNR map of CMRR single tuned sodium coil.

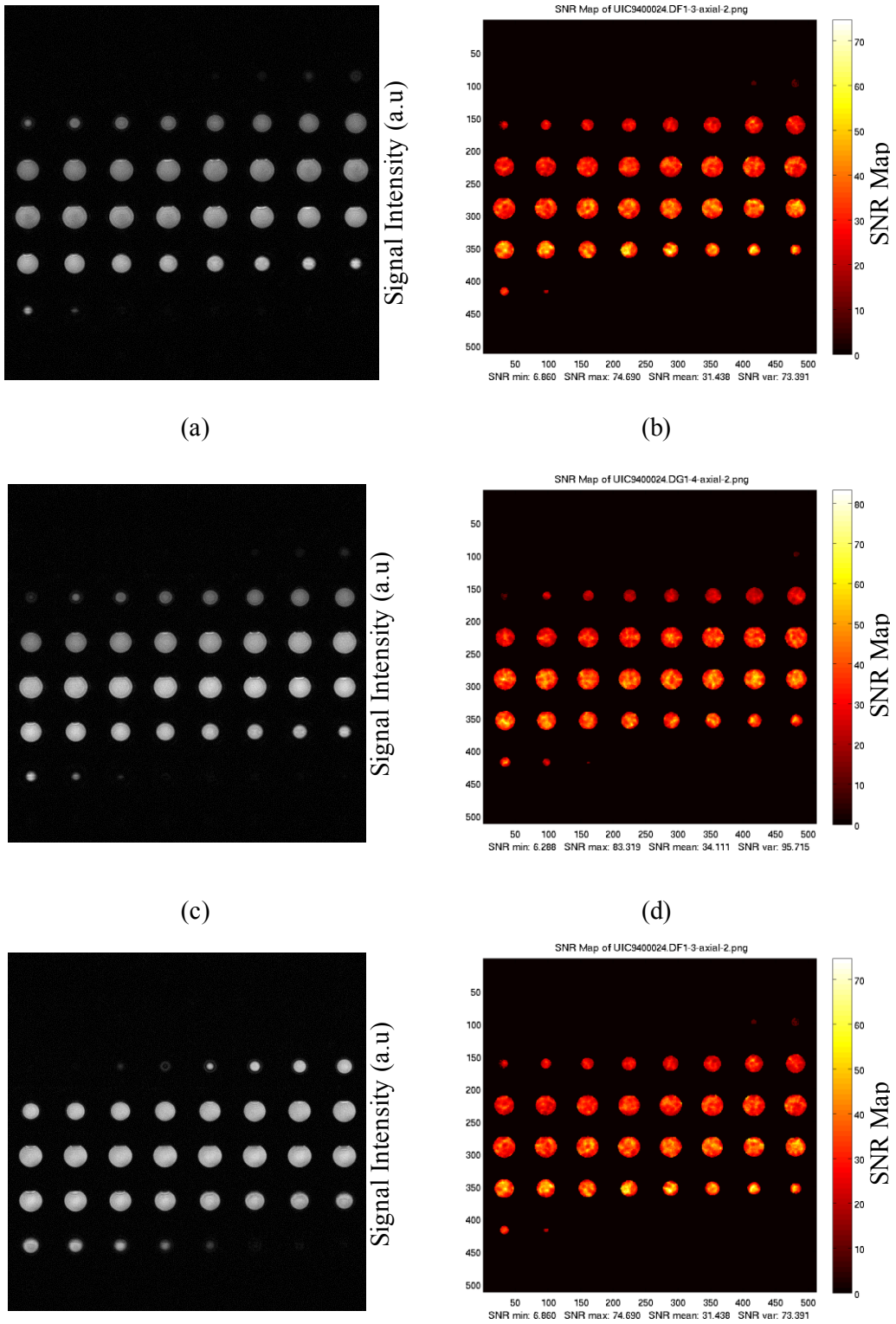

Fig.37: Comparison of center slice 2 for (a) Signal intensity in arbitrary units (a.u.) image and (b) SNR map of sodium channel of P_{31}- Na_{23} coil. (c) Signal intensity (a.u.) image and (d) SNR map of sodium channel of sodium channel of $Na_{23} - O_{17}$ coil. (e) Signal intensity (a.u.) image and (f) SNR map of CMRR single tuned sodium coil.

4.4.4 Phosphorous imaging

Phosphorous images of the second phantom are obtained using a TPI sequence with parameters TE/TR = 0.150/500 msec, FOV = 200 mm x 200mm x 200mm, maximum gradient amplitude = 4mT/m, radial fraction = 0.3, Total Rings = 32, Total Trajectories = 406, K_{Max} = 50, K_0 = 15, maximum gradient slew rate = 99.89 mT/m/msec, to give a 3mm isotropic resolution, number of averages = 1 and number of repetitions = 2. A closer inspection of phosphorous images in Fig.38 reveals that all images are of satisfactory quality and with acceptable SNR, indicating the usability of the proposed design.

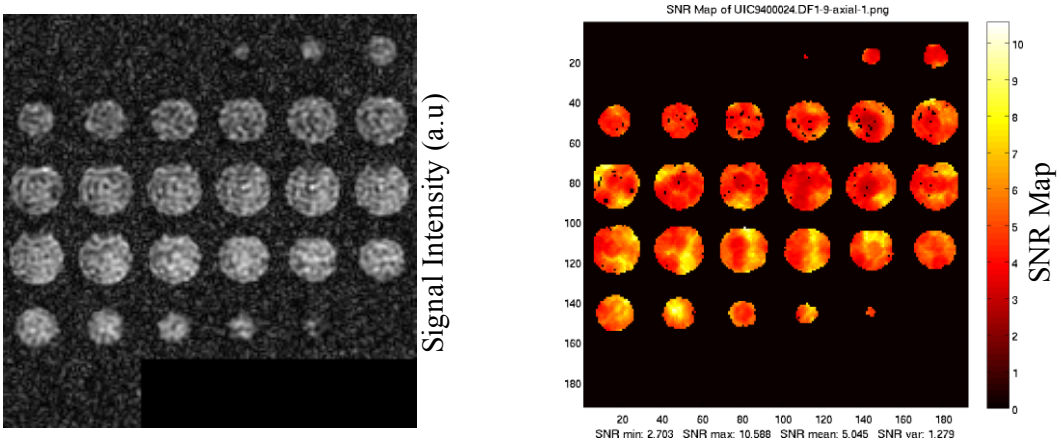

(a) (b)

Fig.38: Comparison of phosphorus images from phosphorus channel of P_{31}- Na_{23} coil. (a) is an image of signal intensity in arbitrary units (a.u) and (b) displays the SNR map.

4.4.5 Oxygen imaging

Similarly to phosphorous images, oxygen images of the second phantom are obtained using TPI sequence with parameters TE/TR = 0.260/65 msec, FOV = 180 mm x 180 mm x 180 mm, maximum gradient amplitude = 4mT/m, radial fraction = 0.36, total rings = 56, total trajectories=1502, K_{Max}=100, K_0=36.1515, maximum gradient slew rate = 58.80 mT/m/msec, to give a 3mm isotropic resolution, number of averages = 10 and number of repetitions = 2. Fig.39 shows the comparison of oxygen images from CMRR single resonant oxygen coil and images from the oxygen channel of $Na_{23} - O_{17}$ coil. The images are acquired as

axial slices of the phantom. The mean SNR measurements of the oxygen image obtained by the CMRR single resonant coil is 30% better than the dual resonant coil.

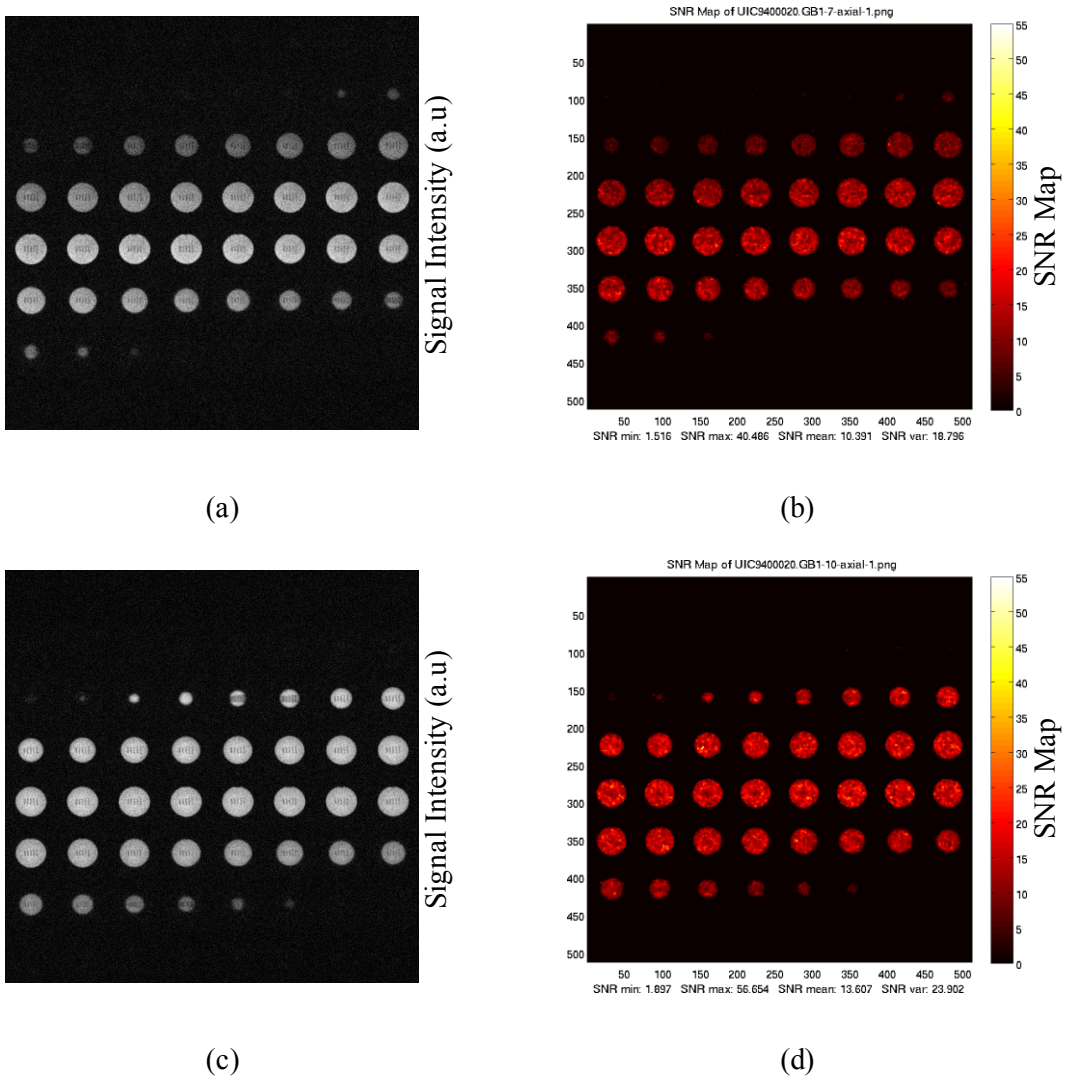

Fig.39: Comparison of images of O-17 nuclei for (a) Signal intensity in arbitrary units (a.u.) image of CMRR single tuned oxygen coil and (b) SNR map of CMRR single tuned oxygen coil. (c) Signal intensity (a.u.) image of oxygen channel of $Na_{23} - O_{17}$ coil and (b) SNR map of oxygen channel of $Na_{23} - O_{17}$ coil.

Table 7 summarizes the SNR comparison results. In general, a single resonant coil performs better than a dual resonant coil, as dual resonant coils sacrifice performance to achieve multiple resonances. It is also due to the fact that the coil was not well optimized for performance. Optimization of dual resonant coils will be pursued in future efforts.

Table 7: SNR comparison of different designs.

	Na_{23} Channel	P_{31} Channel	O_{17} Channel
P_{31} – Na_{23} Coil	31.966	5.045	--
Na_{23} – O_{17} Coil	34.384	--	10.75
CMRR Na_{23} Coil	36.2595	--	--
CMRR – O_{17} Coil	--	--	13.6

4.5 Discussion

A new theoretical approach to multi-tune a coupled multiconductor transmission line coil (CMTL) is proposed. The resonant frequencies are computed by solving the eigenvalue problem of the admittance matrix using the reduced dimension method. The proposed theory is validated with standard published single tuned TEM coil result. The model is also used to analyze two newly proposed dual tuned coils. One of the main advantages of the new approach is that it offers an analytical formulation for the port mode currents. Even though the proposed analytical approach reduces the computational effort for solving 4n X 4n eigenvalue problem, to compute the required terminations for multiple frequencies may lead to constraints of solving two or more quadratic equations using the numerical methods. As mentioned earlier, the model predicts the port mode currents, but to extend these port mode currents into the field profiles of the resonator, extra information like per-unit-length parameters are needed. The proposed model offers a way to optimize the mode separation and the field optimization using lumped element terminations. Future efforts will be focused to extend the model to analyze asymmetrically loaded coil.

Chapter 5

Conclusion and future work

5.1 Summary and findings

In this dissertation, the author embarked on developing a new approach to design and optimize RF coils for MRI. One of the key contributions of this thesis is the multiport representation of the MTL structure using a port admittance matrix and a description of numerous ways of calculating the admittance matrix. The calculation methods include both experimental and numerical procedures, thus providing flexibility to the designer to choose an optimal approach.

As a part of the theoretical development, it was mathematically proved that the solution of the characteristic equation of the admittance matrix provides the conditions for resonance. This novel approach formed the cornerstone of this dissertation. The suggested method offers flexibility to use matrix algebra to determine the resonant conditions; thus, reducing the computational complexity and also providing analytical formulations.

An admittance matrix which is of the form *block circulant with circulant blocks* matrix, $BCCB_{m.n}$, was diagonalized using a special matrix fashioned as a result of the Kronecker product operation applied to Fourier matrices. Utilization of such a special matrix allows the direct computation of termination values as compared to the other existing methods which are iterative in nature. When the new approach was applied to a standard published resonator, it predicted all the fundamental port modes, including those not considered in earlier investigations. The new method also allowed the determination of resonating conditions for unequal terminations.

As a demonstration of the practical application of the 2n-port model and Kronecker product operator, a new dual tuned dual element (DTDE) surface coil was proposed. The DTDE coil was designed to operate at sodium (78.6 MHz) and proton (298 MHz), frequencies as required in a Philips 7T human MRI scanner. The coil was designed and manufactured, and images of an oil phantom and a saline phantom were obtained

in the scanner. The performance of the DTDE coil can be regarded as a success; the observed image patterns were found to be in agreement with the full wave 3D EM simulated results.

With the use of the 2n-port model and the Kronecker product operator, the reduction of computational complexity is only pertinent to a matrix of the form *block circulant with circulant blocks* matrix. A novel, a much more powerful reduced dimension method was introduced to achieve a similar computational complexity reduction advantage for a matrix of the form circulant block matrix. The reduced dimension method is the most significant contribution in this thesis.

Finally, two new dual tuned head coils 1) phosphorus-31 (162.09 MHz) and sodium-23(105.9 MHz), and 2) sodium-23(105.9 MHz) and oxygen-17(53.2MHz) for 9.4T human MRI system are proposed, designed and analyzed using the reduced dimension method. Their validation was done using 3D EM simulations as well as using MR imaging tests on a scanner. Imaging tests were conducted on phantoms, and the tests indicated that RF coil achieved good performance limits and high SNR in the region of interest. Furthermore, performance comparisons with existing single tuned coil indicated comparable SNR in the regions of interest. As a byproduct of the proposed method, an innovative way of reducing residual coupling between conductors using lumped elements was examined using the simulations. Part of the results are presented at various International society of Magnetic Resonance in Medicine conference [66],[67]

5.2 Future applications and unsolved problems

Based on problems encountered during the development and implementation of this work, recommendations for further research should be directed towards following areas:

Partial volume coils as compared to closed volume coils have significantly higher transmit efficiency, because of their excitation region is significantly decreased. An SNR increase can also be obtained as the noise contributing region is decreased. Preference for partial volume coils is desired due to the patient comfort. A partial volume coil can be treated as a full volume coil with few conductors missing. A careful observation of the port admittance matrix reveals that the matrix is similar to a circulant block matrix form

with some missing rows and columns. The 2n port method with modifications can be explored to determine the resonating conditions.

Similar to partial volume coils, it is advantageous to use coils with unequal conductor lengths. Since such coils already exist, the 2n-port model can be used to analyze and perform optimization on those coils.

Multichannel coils are widely used for accelerated imaging, and the proposed model is well suited to explore the designs for multi-resonant multichannel coils. Similarly, the new paradigm can find applications in the design of triple resonant coils.

One interesting problem that requires attention is interleaved multi-resonant coils, where an unequal number of elements are used. These kinds of coils find their usefulness due to the requirement of one of the frequencies needing more of an imaging region than the other. The port admittance of such coils is very interesting, and a representative form of it is shown in equation (108).

$$\begin{bmatrix} \begin{bmatrix} a_1 & a_2 & a_3 & a_4 \\ a_4 & a_1 & a_2 & a_3 \\ a_3 & a_4 & a_1 & a_2 \\ a_2 & a_3 & a_4 & a_1 \end{bmatrix} & \begin{bmatrix} b_1 & b_2 \\ b_4 & b_1 \\ b_3 & b_4 \\ b_2 & b_3 \end{bmatrix} \\ \begin{bmatrix} c_1 & c_2 & c_3 & c_4 \\ c_4 & c_1 & c_2 & c_3 \end{bmatrix} & \begin{bmatrix} d_1 & d_2 \\ d_2 & d_1 \end{bmatrix} \end{bmatrix} \tag{108}$$

The overall admittance matrix is a square matrix; however, the blocks on the diagonal are circulant matrices but are of unequal sizes. The off-diagonal blocks are rectangular circulant matrices that are transposed to each other. The admittance matrix needs to be regularized, and the 2n-port model should be "tweaked" to reduce the computations. A similar matrix structure arises when analyzing rectangular planar loops.

The concepts that are presented in this thesis are largely used for RF coil designs for MRI applications. Some of the presented ideas can be utilized outside the MRI domain. The planar transmission line resonators have been considered as the most commonly used resonator designs for applications in radio frequency (RF) and microwave (MW) integrated circuits like filters, oscillators, and amplifiers because of many

attractive features, such as low-cost, compact size, lightweight, easy massive fabrication, etc. The proposed models can be used to design some of those resonators.

Block circulant matrices arise in many areas of physics or statistics, in the derivation of the theoretical formulas, as well as in the numerical methods for the computation of the related solutions. In electromagnetism, they appear when the method of moments is used to solve the integral equation of the diffraction by an axisymmetric body, whose surface is modeled by equally spaced finite segments, yielding a many-fold rotational symmetric configuration.

The biggest shortcoming of this thesis is that models are considered only for unloaded or symmetrically loaded conditions. Loss mechanisms including conductor losses, as well as complex biological tissue loading effects, were purposely avoided to reduce the complicated analytical formulations. It is a widely accepted fact that loaded conditions affect the matching conditions more than the tuned values; nevertheless, the proposed model can still be used to determine the resonant conditions for asymmetrical loads; it is only that the computational advantage may not be realized completely.

Bibliography

[1] R. R. Edelman, J. V. Crues, J. R. Hesselink, and M. B. Zlatkin, *Clinical Magnetic Resonance Imaging*, 3rd ed. W B Saunders Co, 2005.

[2] E. Moser, F. Stahlberg, M. E. Ladd, and S. Trattnig, "7-T MR--from research to clinical applications?," *NMR Biomed.*, vol. 25, no. 5, pp. 695–716, May 2012.

[3] J. R. G. (Editor) J. Thomas Vaughan (Editor), *RF Coils for MRI*. John Wiley and Sons, 2012.

[4] G. Bogdanov and R. Ludwig, "Coupled microstrip line transverse electromagnetic resonator model for high-field magnetic resonance imaging," *Magn. Reson. Med.*, vol. 47, no. 3, pp. 579–593, Mar. 2002.

[5] J. T. Vaughan, H. P. Hetherington, J. O. Otu, J. W. Pan, and G. M. Pohost, "High frequency volume coils for clinical NMR imaging and spectroscopy.," *Magn. Reson. Med.*, vol. 32, no. 2, pp. 206–18, Aug. 1994.

[6] a Vitacolonna, G. Placidi, a Sotgiu, P. Jezzard, and M. Alecci, "Theory of Double Tuned TEM Resonators and Workbench Validation in a Frequency Range of 100-350 MHz," in *Proc. Intl. Soc. Magn. Reson. Med*, 2005, vol. 13, p. 2423.

[7] N. De Zanche and P. S. Allen, "Sensitivity calculations and comparisons for shielded elliptical and circular birdcage coils," *Magn. Reson. Med.*, vol. 47, no. September 2000, pp. 364–371, 2002.

[8] B. Wu, X. Zhang, P. Qu, and G. X. Shen, "Design of an inductively decoupled microstrip array at 9.4 T," *J. Magn. Reson.*, vol. 182, no. 1, pp. 126–132, Sep. 2006.

[9] G. Adriany, P. F. Van De Moortele, F. Wiesinger, S. Moeller, J. P. Strupp, P. Andersen, C. Snyder, X. Zhang, W. Chen, K. P. Pruessmann, P. Boesiger, T. Vaughan, and K. Uğurbil, "Transmit and receive transmission line arrays for 7 tesla parallel imaging," *Magn. Reson. Med.*, vol. 53, no. 2, pp. 434–445, Feb. 2005.

[10] X. Zhang, X.-H. Zhu, and W. Chen, "Higher-order harmonic transmission-line RF coil design for MR applications.," *Magn. Reson. Med.*, vol. 53, no. 5, pp. 1234–9, May 2005.

[11] R. F. Lee and R. Xue, "A transmit/receive volume strip array and its mode mixing theory in MRI," *Magn. Reson. Imaging*, vol. 25, no. 9, pp. 1312–1332, Nov. 2007.

[12] E. M. Purcell, H. C. Torrey, and R. V. Pound, "Resonance Absorption by Nuclear Magnetic Moments in a Solid," *Phys. Rev.*, vol. 69, no. 1–2, pp. 37–38, Jan. 1946.

[13] F. Bloch, "Nuclear Induction," *Phys. Rev.*, vol. 70, no. 7–8, pp. 460–474, Oct. 1946.

[14] P. C. LAUTERBUR, "Image Formation by Induced Local Interactions: Examples Employing Nuclear Magnetic Resonance," *Nature*, vol. 242, no. 5394, pp. 190–191, Mar. 1973.

[15] N. M. Salibi and M. A. 1955- Brown, *Clinical MR spectroscopy : first principles*. Wiley-Liss, 1998.

[16] R. W. Brown, Y.-C. N. Cheng, E. M. Haacke, M. R. Thompson, and R. Venkatesan, Eds., *Magnetic Resonance Imaging*. Chichester, UK: John Wiley & Sons Ltd, 2014.

[17] A. H. L. W S Hinshaw, "An introduction to NMR imaging: From the Bloch equation to the imaging equation," *Proc. IEEE*, vol. 71, no. 3, pp. 338–350, 1983.

[18] J. P. Mugler, "Overview of MR imaging pulse sequences.," *Magnetic resonance imaging clinics of North America*, vol. 7, no. 4. pp. 661–97, Nov-1999.

[19] J. P. Ridgway, "Cardiovascular magnetic resonance physics for clinicians: part I," *J. Cardiovasc. Magn. Reson.*, vol. 12, no. 1, p. 71, 2010.

[20] Z. H. Cho, H. S. Kim, H. B. Song, and J. Cumming, "Fourier transform nuclear magnetic resonance tomographic imaging," *Proc. IEEE*, vol. 70, no. 10, pp. 1152–1173, 1982.

[21] M. A. Bernstein, K. F. King, and X. J. Zhou, *Handbook of MRI pulse sequences*. Academic Press, 2004.

[22] J. Jin, *Electromagnetic Analysis and Design in Magnetic Resonance Imaging*. CRC Press, 1998.

[23] S. Sengupta, S. Tadanki, J. C. Gore, and E. Brian Welch, "Prospective real-time head motion correction using inductively coupled wireless NMR probes," *Magn. Reson. Med.*, vol. 72, no. 4, pp. 971–985, Oct. 2014.

[24] D. K. Sodickson, "Spatial Encoding Using Multiple rf Coils : SMASH Imaging and Parallel MRI," pp. 1–12, 1995.

[25] K. P. Pruessmann, M. Weiger, M. B. Scheidegger, and P. Boesiger, "SENSE: sensitivity encoding for fast MRI.," *Magn. Reson. Med.*, vol. 42, no. 5, pp. 952–62, Nov. 1999.

[26] U. Katscher and P. Börnert, "Parallel RF transmission in MRI.," *NMR Biomed.*, vol. 19, no. 3, pp. 393–400, May 2006.

[27] A. Sharma, S. Tadanki, M. Jankiewicz, and W. A. Grissom, "Highly-accelerated Bloch-Siegert |B1+| mapping using joint autocalibrated parallel image reconstruction.," *Magn. Reson. Med.*, vol. 71, no. 4, pp. 1470–7, Apr. 2014.

[28] I. Graesslin, H. Homann, S. Biederer, P. Börnert, K. Nehrke, P. Vernickel, G. Mens, P. Harvey, and U. Katscher, "A specific absorption rate prediction concept for parallel transmission MR.," *Magn. Reson. Med.*, vol. 000, pp. 1–11, Jan. 2012.

[29] H. Homann, I. Graesslin, H. Eggers, K. Nehrke, P. Vernickel, U. Katscher, O. Dössel, and P. Börnert, "Local SAR management by RF shimming: a simulation study with multiple human body models.," *MAGMA*, vol. 25, no. 3, pp. 193–204, Jun. 2012.

[30] R. F. Lee, R. O. Giaquinto, and C. J. Hardy, "Coupling and decoupling theory and its application to the MRI phased array.," *Magn. Reson. Med.*, vol. 48, no. 1, pp. 203–13, Jul. 2002.

[31] P. B. Roemer, W. A. Edelstein, C. E. Hayes, S. P. Souza, and O. M. Mueller, "The NMR phased array," *Magn. Reson. Med.*, vol. 16, no. 2, pp. 192–225, Nov. 1990.

[32] G. C. Nascimento, F. F. Paiva, and A. C. Silva, "Inductive Decoupling of RF Coil Arrays: A Study

at 7T," *Proc. Intl. Soc. Mag. Reson. Med*, vol. 14, 2006.

[33] D. I. Hoult, G. Kolansky, D. Kripiakevich, and S. B. King, "The NMR multi-transmit phased array: a Cartesian feedback approach.," *J. Magn. Reson.*, vol. 171, no. 1, pp. 64–70, Nov. 2004.

[34] J. Moore, R. D. Colón, S. Tadanki, and K. W. Waddell, "Heteronuclear refocusing by nonlinear phase and amplitude modulation on a single transmitter channel," *J. Magn. Reson.*, vol. 245, pp. 58–62, 2014.

[35] S. Tadanki, R. D. Colon, J. Moore, and K. W. Waddell, "Double Tuning a Single Input Probe for Heteronuclear NMR Spectroscopy at Low Field," *J. Magn. Reson.*, vol. null, no. null, Jul. 2012.

[36] S. Ramo, J. R. Whinnery, and T. V. Duzer, *Fields and Waves in Communication Electronics*. Wiley-India, 2003.

[37] D. M.Pozar, *Microwave Engineering, 3rd Ed*. Wiley India Pvt. Limited, 2009.

[38] R. F. Lee, C. R. Westgate, R. G. Weiss, D. C. Newman, and P. a Bottomley, "Planar strip array (PSA) for MRI.," *Magn. Reson. Med.*, vol. 45, no. 4, pp. 673–83, Apr. 2001.

[39] X. Zhang, K. Ugurbil, R. Sainati, and W. Chen, "An inverted-microstrip resonator for human head proton MR imaging at 7 tesla.," *IEEE Trans. Biomed. Eng.*, vol. 52, no. 3, pp. 495–504, Mar. 2005.

[40] B. a. Baertlein, Ö. Özbay, T. Ibrahim, R. Lee, Y. Yu, A. Kangarlu, and P. M. L. Robitaille, "Theoretical model for an MRI radio frequency resonator," *IEEE Trans. Biomed. Eng.*, vol. 47, no. 4, pp. 535–546, Apr. 2000.

[41] X. Zhang, K. Ugurbil, and W. Chen, "A microstrip transmission line volume coil for human head MR imaging at 4T," *J. Magn. Reson.*, vol. 161, no. 2, pp. 242–251, Apr. 2003.

[42] C. R. Paul, *Analysis of Multiconductor Transmission Lines*. John Wiley & Sons, 2008.

[43] C. Moler and C. Van Loan, "Nineteen Dubious Ways to Compute the Exponential of a Matrix, Twenty-Five Years Later," *SIAM Rev.*, vol. 45, no. 1, pp. 3–49, Jan. 2003.

[44] "MATLAB R2008." Mathworks, Natick MA.

[45] S. M. Serbin, *Circulant Matrices.*, vol. 35. John Wiley & Sons, 1980.

[46] P. J. Davis, *Circulant Matrices*. Chelsea, 1994.

[47] Y.-C. N. Cheng, T. P. Eagan, T. Chmielewski, J. Flock, M.-C. Kang, T. K. Kidane, S. M. Shvartsman, and R. W. Brown, "A degeneracy study in the circulant and bordered-circulant approach to birdcage and planar coils.," *MAGMA*, vol. 16, no. 2, pp. 103–11, Jul. 2003.

[48] "ANSYS MAXWELL." ANSYS Corp, Pittusburgh, PA.

[49] "ANSYS HFSS," *Electromagnetic Simulation Solutions from ANSYS*. ANSYS Corp, Pittusburgh, PA, 2012.

[50] A. Vukovic, P. Sewell, D. McKirdy, D. Thomas, T. M. Benson, C. Christopoulos, and P. Glover, "A dynamic vector model of microstrip RF resonators for high-field MR imaging.," *IEEE Trans. Med. Imaging*, vol. 27, no. 6, pp. 766–74, Jun. 2008.

[51] C. E. Hayes, W. A. Edelstein, J. F. Schenck, O. M. Mueller, and M. Eash, "An efficient, highly homogeneous radiofrequency coil for whole-body NMR imaging at 1.5 T," *J. Magn. Reson.*, vol. 63, no. 3, pp. 622–628, Jul. 1985.

[52] P. M. Joseph and D. Lu, "A technique for double resonant operation of birdcage imaging coils.," *IEEE transactions on medical imaging*, vol. 8, no. 3. pp. 286–94, Jan-1989.

[53] U. A. Amari, Smain, J. Bornemann, P. C. M. Van Zijl, and P. B. Barker, "Multiple tuning of birdcage resonators," *Magn. Reson. Med.*, vol. 37, no. 2, pp. 243–251, Feb. 1997.

[54] T. Lanz, J. Ruff, A. Weisser, and A. Haase, "Double tuned 23Na 1H nuclear magnetic resonance birdcage for application on mice in vivo," *Rev. Sci. Instrum.*, vol. 72, no. 5, p. 2508, 2001.

[55] G. B. Matson, P. Vermathen, and T. C. Hill, "A practical double-tuned 1H/31P quadrature birdcage headcoil optimized for 31P operation.," *Magn. Reson. Med.*, vol. 42, no. 1, pp. 173–82, Jul. 1999.

[56] T. K. Shen GX, Boada FE, "Dual-frequency, dual-quadrature, birdcage RF coil design with identical B1 pattern for sodium and proton imaging of the human brain at 1.5 T." Magn Reson Med, p. 38(5), 717-25.

[57] J. R. Fitzsimmons, B. L. Beck, and H. Ralph Brooker, "Double resonant quadrature birdcage," *Magn. Reson. Med.*, vol. 30, no. 1, pp. 107–114, Jul. 1993.

[58] P. Vernickel, P. Röschmann, C. Findeklee, K.-M. Lüdeke, C. Leussler, J. Overweg, U. Katscher, I. Grässlin, and K. Schünemann, "Eight-channel transmit/receive body MRI coil at 3T.," *Magn. Reson. Med.*, vol. 58, no. 2, pp. 381–9, Aug. 2007.

[59] W. Dürr and S. Rauch, "A dual-frequency circularly polarizing whole-body MR antenna for 69/170 MHz.," *Magn. Reson. Med.*, vol. 19, no. 2, pp. 446–55, Jun. 1991.

[60] X. Zhang, X. Zhu, H. Qiao, H. Liu, T. Vaughan, K. Ugurbil, and W. Chen, "A circular-polarized double-tuned (31P and 1H) TEM coil for human head MRI/MRS at 7T," *ISMRM*, p. 423, 2003.

[61] G. Bogdanov, "Dual-tuned microstrip resonator volume coil," US 7427861 B2, 2006.

[62] J. Tropp, "A model for MR image shading in multi-mode resonators," *Proc. Work. MRI Hardw. Clevel. 2001.*, p. 11, 2001.

[63] H. P. H. N.I.Avdievich, A.S.Peshkovsky, "High-Field Double-Tuned TEM/Birdcage Hybrid Volume Coil for Human Brain Imaging," *Proc. ISMRM 13th Annu. Sci. Meet. Berlin*, p. 239, 2007.

[64] S. Rjasanow, "Effective algorithms with circulant-block matrices," *Linear Algebra Appl.*, vol. 202, pp. 55–69, Apr. 1994.

[65] R. Mongia, I. J. Bahl, and P. Bhartia, *RF and Microwave Coupled-line Circuits*. Artech House, 1999.

[66] S. Tadanki, G. Bagadanov, R. Ludwig, M. E. Brevard, K. R. Thulborn, and I. Atkinson, "Multi Tuned Coupled Microstrip Resonator for High Field Magnetic Resonance Imaging at 9.4T Human

System," in *Proc. Intl. Soc. Mag. Reson. Med, Berlin*, 2007, p. 1060.

[67] S.Tadanki, "RF coil design using circulant and block circulant matrix algebra," in *Proc. Intl. Soc. Mag. Reson. Med (24), Singapore*, 2016, p. 2163.

Appendix A

Block matrix algebra examples

Circulant matrix

This is a matrix in which each row vector is rotated one element to the right relative to the preceding row vector. Example for a 3 by 3 circulant matrix $\mathbf{A_{3x3}}$ is as follows

$$\mathbf{A_{3x3}} = \begin{bmatrix} 1 & 2 & 3 \\ 3 & 1 & 2 \\ 2 & 3 & 1 \end{bmatrix}$$

Block matrix

In this matrix, each element is a block. Example for a block matrix is $\mathbf{P_{2x3}}$ with elements **A, B, C,** and **D** is as follows

$$\mathbf{P_{2x3}} = \begin{bmatrix} \mathbf{A} & \mathbf{B} \\ \mathbf{C} & \mathbf{D} \end{bmatrix} = \begin{bmatrix} \begin{bmatrix} 1 & 2 & 3 \\ 4 & 5 & 6 \\ 7 & 8 & 9 \end{bmatrix} & \begin{bmatrix} a & b & c \\ d & e & f \\ g & h & i \end{bmatrix} \\ \begin{bmatrix} k & l & m \\ o & p & q \\ r & s & t \end{bmatrix} & \begin{bmatrix} 11 & 12 & 13 \\ 14 & 15 & 16 \\ 17 & 18 & 19 \end{bmatrix} \end{bmatrix}$$

Fourier matrix

Fourier matrix $\mathbf{F}_n$ is a square matrix with entities given by

$$F_{p,q} = \omega^{(p-1)(q-1)} \ \forall\ p = 0, 1, \cdots, n-1, \text{ and } q = 0, 1, \cdots, n-1,$$

$\omega = e^{\left(2\pi j / n\right)}$. Here $j = \sqrt{-1}$ is the imaginary number

Some of the examples of Fourier matrices

$$\mathbf{F_2} = \frac{1}{\sqrt{2}} \begin{bmatrix} 1 & 1 \\ 1 & -1 \end{bmatrix} \text{ and } \mathbf{F_3} = \frac{1}{\sqrt{3}} \begin{bmatrix} 1 & 1 & 1 \\ 1 & -0.5 + 0.866 \cdot j & -0.5 - 0.866 \cdot j \\ 1 & -0.5 - 0.866 \cdot j & -0.5 + 0.866 \cdot j \end{bmatrix}$$

Kronecker product operator

Kronecker product, denoted by $\otimes$, is the tensor product of **A** and **B**

$$\text{if } \mathbf{A} = \begin{bmatrix} a & b \\ c & d \end{bmatrix} \text{ and } \mathbf{B} = \begin{bmatrix} 1 & 2 & 3 \\ 3 & 1 & 2 \\ 2 & 3 & 1 \end{bmatrix}, \text{ then}$$

$$\boldsymbol{A} \otimes \boldsymbol{B} = \begin{bmatrix} a & b \\ c & d \end{bmatrix} \otimes \begin{bmatrix} 1 & 2 & 3 \\ 3 & 1 & 2 \\ 2 & 3 & 1 \end{bmatrix} = \begin{bmatrix} a\boldsymbol{B} & b\boldsymbol{B} \\ c\boldsymbol{B} & d\boldsymbol{B} \end{bmatrix} = \begin{bmatrix} a1 & a2 & a3 & b1 & b2 & b3 \\ a3 & a1 & a2 & b3 & b1 & b2 \\ a2 & a3 & a1 & b2 & b3 & b1 \\ c1 & c2 & c3 & d1 & d2 & d3 \\ c3 & c1 & c2 & d3 & d1 & d2 \\ c2 & c3 & c1 & d2 & d3 & d1 \end{bmatrix}$$

Block circulant matrix

Each element is a block matrix and blocks are arranged in circulant fashion. Example for a block circulant matrix is $\mathbf{AB}_{2x3}$ with elements **A, B, C,** and **D** is as follows

$$\mathbf{BC}_{2x3} = \begin{bmatrix} \mathbf{A} & \mathbf{B} \\ \mathbf{B} & \mathbf{A} \end{bmatrix} = \begin{bmatrix} \begin{bmatrix} 1 & 2 & 3 \\ 4 & 5 & 6 \\ 7 & 8 & 9 \end{bmatrix} & \begin{bmatrix} a & b & c \\ d & e & f \\ g & h & i \end{bmatrix} \\ \begin{bmatrix} a & b & c \\ d & e & f \\ g & h & i \end{bmatrix} & \begin{bmatrix} 1 & 2 & 3 \\ 4 & 5 & 6 \\ 7 & 8 & 9 \end{bmatrix} \end{bmatrix}$$

Circulant block matrix

Block matrix in which each block is a circulant matrix.

$$\boldsymbol{CB}_{2x3} = \begin{bmatrix} \mathbf{A} & \mathbf{B} \\ \mathbf{C} & \mathbf{D} \end{bmatrix} = \begin{bmatrix} \begin{bmatrix} 1 & 2 & 3 \\ 3 & 1 & 2 \\ 2 & 3 & 1 \end{bmatrix} & \begin{bmatrix} a & b & c \\ c & a & b \\ b & c & a \end{bmatrix} \\ \begin{bmatrix} k & l & m \\ m & k & l \\ l & m & k \end{bmatrix} & \begin{bmatrix} 11 & 12 & 13 \\ 13 & 11 & 12 \\ 12 & 13 & 11 \end{bmatrix} \end{bmatrix}$$

Block circulant with circulant block

Each block is circulant and blocks are arranged in circulant fashion

$$\boldsymbol{BCCB_{2x3}} = \begin{bmatrix} \mathbf{A} & \mathbf{B} \\ \mathbf{B} & \mathbf{A} \end{bmatrix} = \begin{bmatrix} \begin{bmatrix} 1 & 2 & 3 \\ 3 & 1 & 2 \\ 2 & 3 & 1 \end{bmatrix} & \begin{bmatrix} a & b & c \\ c & a & b \\ b & c & a \end{bmatrix} \\ \begin{bmatrix} a & b & c \\ c & a & b \\ b & c & a \end{bmatrix} & \begin{bmatrix} 1 & 2 & 3 \\ 3 & 1 & 2 \\ 2 & 3 & 1 \end{bmatrix} \end{bmatrix}$$

Permutation matrix J

Example for a 4 X 4 permutation matrix $\mathbf{J_{4x4}}$ is as follows

$$\mathbf{J_{4x4}} = \begin{bmatrix} 0 & 1 & 0 & 0 \\ 0 & 0 & 1 & 0 \\ 0 & 0 & 0 & 1 \\ 1 & 0 & 0 & 0 \end{bmatrix}$$

Eigenvalues of 4 X 4 permutation matrix $\mathbf{J_{4x4}}$: $\omega = [-1, 1\text{j}, -1\text{j}, 1]^{\text{T}}$

Eigenvector corresponds to eigenvalue ω = -1 is $[\ 0.5\ ,\ -0.5,\ -0.5,\ \ 0.5\ ]^{\text{T}}$

$\omega = 1\text{j}$ is $[\ 0.5\ ,\ \ 0.5\text{j},\ -0.5, -0.5\text{j}\ ]^{\text{T}}$

ω = -1j is $[\ 0.5\ ,\ -0.5\text{j},\ -0.5,\ \ 0.5\text{j}\ ]^{\text{T}}$

$\omega = 1$ is $[-0.5\ , -0.5,\ -0.5,\ -0.5\ ]^{\text{T}}$

Example for a 2 X 2 permutation matrix $\mathbf{J_{2x2}}$ is as follows

$$\mathbf{J_{2x2}} = \begin{bmatrix} 0 & 1 \\ 1 & 0 \end{bmatrix}$$

Eigenvalues of 4 X 4 permutation matrix $\mathbf{J_{2x2}}$: $\omega = [-1\ , 1]^{\text{T}}$

Eigenvector corresponds to eigenvalue

ω = -1 is $[\ -0.7071\ ,\ 0.7071\ ]^{\text{T}}$

$\omega = 1$ is $[\ \ 0.7071\ ,\ 0.7071\ ]^{\text{T}}$

Appendix B

Diagonalization examples

Circulant block matrix diagonalization

A $CB_{m,n}$ matrix A can be converted into block diagonal matrix M (where each block is a diagonal matrix) using following mathematical operation

$$\mathrm{M} = (F_m \otimes F_n)A(F_m \otimes F_n)^*$$

$$\mathrm{A} = \begin{bmatrix} \begin{bmatrix} 1 & 5 \\ 5 & 1 \end{bmatrix} & \begin{bmatrix} 3 & 9 \\ 9 & 3 \end{bmatrix} \\ \begin{bmatrix} 11 & 13 \\ 13 & 11 \end{bmatrix} & \begin{bmatrix} 23 & 29 \\ 29 & 23 \end{bmatrix} \end{bmatrix}$$

$$\mathrm{M} = (F_2 \otimes F_2)A(F_2 \otimes F_2)^* \leftrightarrow \begin{bmatrix} \begin{bmatrix} 47 & 0 \\ 0 & -9 \end{bmatrix} & \begin{bmatrix} -17 & 0 \\ 0 & 3 \end{bmatrix} \\ \begin{bmatrix} -29 & 0 \\ 0 & -1 \end{bmatrix} & \begin{bmatrix} 11 & 0 \\ 0 & -1 \end{bmatrix} \end{bmatrix}$$

If matrix A is circulant block block circulant matrix $BCCB_{m.n,}$ Then the following operation leads to diagonal matrix $diag(diag(M_1), diag(M_2), \dots, diag(M_n)) = (F_m \otimes F_n)A(F_m \otimes F_n)^*$

$$\mathrm{A} = \begin{bmatrix} 1 & 5 & \begin{bmatrix} 3 & 9 \\ 9 & 3 \end{bmatrix} \\ 5 & 1 & \begin{bmatrix} 3 & 9 \\ 9 & 3 \end{bmatrix} \\ \begin{bmatrix} 3 & 9 \\ 9 & 3 \end{bmatrix} & \begin{bmatrix} 1 & 5 \\ 5 & 1 \end{bmatrix} \end{bmatrix} \qquad \mathrm{M} = (F_2 \otimes F_2)A(F_2 \otimes F_2)^* \leftrightarrow \begin{bmatrix} 18 & 0 & 0 & 0 \\ 0 & -10 & 0 & 0 \\ 0 & 0 & -6 & 0 \\ 0 & 0 & 0 & 2 \end{bmatrix}$$

Reduced dimension method example

Let us consider the following example to demonstrate the reduced dimension method

$$\boldsymbol{CB_{2x3}} = \begin{bmatrix} \mathbf{A} & \mathbf{B} \\ \mathbf{C} & \mathbf{D} \end{bmatrix} = \begin{bmatrix} \begin{bmatrix} 1 & 2 & 3 & 5 \\ 5 & 1 & 2 & 3 \\ 3 & 5 & 1 & 2 \\ 2 & 3 & 5 & 1 \end{bmatrix} & \begin{bmatrix} 5 & 9 & 11 & 17 \\ 17 & 5 & 9 & 11 \\ 11 & 17 & 5 & 9 \\ 9 & 11 & 17 & 5 \end{bmatrix} \\ \begin{bmatrix} 5 & 9 & 11 & 17 \\ 17 & 5 & 9 & 11 \\ 11 & 17 & 5 & 9 \\ 9 & 11 & 17 & 5 \end{bmatrix} & \begin{bmatrix} 1 & 2 & 3 & 5 \\ 5 & 1 & 2 & 3 \\ 3 & 5 & 1 & 2 \\ 2 & 3 & 5 & 1 \end{bmatrix} \end{bmatrix}$$

$\boldsymbol{CB_{2x3}}$ is reduced into four 2by2 matrices by the following

$$\begin{bmatrix} [1.\omega^0 + 2.\omega^1 + 3.\omega^2 + 5.\omega^3] & [5.\omega^0 + 9.\omega^1 + 11.\omega^2 + 17.\omega^3] \\ [5.\omega^0 + 9.\omega^1 + 11.\omega^2 + 17.\omega^3] & [1.\omega^0 + 2.\omega^1 + 3.\omega^2 + 5.\omega^3] \end{bmatrix}$$

$\forall\ \omega = [-1, 1i, -1i, 1]^{\mathrm{T}}$

Reduced dimension matrix for the corresponding eigenvalue is

$\omega = 1$ is $\begin{bmatrix} 11 & 42 \\ 42 & 11 \end{bmatrix}$

its eigenvalues are $\begin{bmatrix} -31 \\ 53 \end{bmatrix}$ and the eigenvectors: $\begin{bmatrix} -\sqrt{2} & \sqrt{2} \\ \sqrt{2} & \sqrt{2} \end{bmatrix}$

$\omega = 1i$ is $\begin{bmatrix} -2+3i & -6+8i \\ -6+8i & -2+3i \end{bmatrix}$

its eigenvalues are $\begin{bmatrix} 4-5i \\ -8+11i \end{bmatrix}$ and the eigenvectors: $\begin{bmatrix} -\sqrt{2} & \sqrt{2} \\ \sqrt{2} & \sqrt{2} \end{bmatrix}$

$\omega = -1$ is $\begin{bmatrix} -3 & -10 \\ -10 & -3 \end{bmatrix}$

its eigenvalues are $\begin{bmatrix} -13 \\ 7 \end{bmatrix}$ and the eigenvectors: $\begin{bmatrix} -\sqrt{2} & \sqrt{2} \\ \sqrt{2} & \sqrt{2} \end{bmatrix}$

$\omega = -1i$ is $\begin{bmatrix} -2-3i & -6-8i \\ -6-8i & -2-3i \end{bmatrix}$

its eigenvalues are $\begin{bmatrix} 4+5i \\ -8-11i \end{bmatrix}$ and the eigenvectors: $\begin{bmatrix} -\sqrt{2} & \sqrt{2} \\ \sqrt{2} & \sqrt{2} \end{bmatrix}$

The overall eigenvalues are $[-31,\ 53\ , 4-5i\ ,\ -8+11i\ , -13\ , 7\ , 4+5i\ , -8-11i]^{\mathrm{T}}$

and eigenvectors are

$$\begin{bmatrix} -\sqrt{2} & \sqrt{2} \\ \sqrt{2} & \sqrt{2} \end{bmatrix} \otimes \begin{bmatrix} 0.5 & -0.5 & -0.5 & 0.5 \\ -0.5 & -0.5i & 0.5i & 0.5 \\ 0.5 & 0.5 & 0.5 & 0.5 \\ -0.5 & 0.5i & -0.5i & 0.5 \end{bmatrix}$$

Appendix C

Open port admittance matrices of different MTL structures

Open port admittance matrix of a small MTL coil

Table 8: The open port admittance of a small MTL coil at 200 MHz. Units are in Siemens (S).

Y_{11}	Y_{12}
-7.438E-03	1.014E-02
9.217E-04	-1.278E-03
1.656E-04	-2.209E-04
7.808E-05	-1.038E-04
5.193E-05	-6.967E-05
4.197E-05	-5.688E-05
3.925E-05	-5.342E-05
4.197E-05	-5.688E-05
5.193E-05	-6.967E-05
7.808E-05	-1.038E-04
1.656E-04	-2.209E-04
9.217E-04	-1.278E-03

Table 9: The magnitude of individual rows elements of the open port admittance matrix of a small MTL coil at 200MHz, when treated as a double cyclic structure. Units are in Siemens (S).

Y_{11}	Y_{12}	Y_{13}	Y_{14}	Y_{31}	Y_{32}	Y_{33}	Y_{34}
-7.438E-03	3.925E-05	1.014E-02	-5.342E-05	1.014E-02	-5.342E-05	-7.438E-03	3.925E-05
9.217E-04	4.197E-05	-1.278E-03	-5.688E-05	-1.278E-03	-5.688E-05	9.217E-04	4.197E-05
1.656E-04	5.193E-05	-2.209E-04	-6.967E-05	-2.209E-04	-6.967E-05	1.656E-04	5.193E-05
7.808E-05	7.808E-05	-1.038E-04	-1.038E-04	-1.038E-04	-1.038E-04	7.808E-05	7.808E-05
5.193E-05	1.656E-04	-6.967E-05	-2.209E-04	-6.967E-05	-2.209E-04	5.193E-05	1.656E-04
4.197E-05	9.217E-04	-5.688E-05	-1.278E-03	-5.688E-05	-1.278E-03	4.197E-05	9.217E-04

Open port admittance matrix of a DTDE coil

Table 10: The magnitude of rows elements of open port admittance matrix of a DTDE coil at 7T sodium frequency (78.6MHz). Units are in Siemens (S).

	Port 1	Port 2	Port 3	Port 4
Port 1	-0.00422	0.01587	-0.00073	-0.00242
Port 2	0.01587	-0.00422	-0.00242	-0.00073
Port 3	-0.00073	-0.00242	-0.00422	0.01587
Port 4	-0.00242	-0.00073	0.01587	-0.00422

Table 11: The magnitude of rows elements of open port admittance matrix of a DTDE coil at 7T proton frequency (298 MHz). Units are in Siemens (S)

	Port 1	Port 2	Port 3	Port 4
Port 1	-0.04006	0.04240	0.00223	-0.00267
Port 2	0.04240	-0.04006	-0.00267	0.00223
Port 3	0.00223	-0.00267	-0.04006	0.04240
Port 4	-0.00267	0.00223	0.04240	-0.04006

Open port admittance matrix of a dual tuned volume coil

Table 12: The magnitude of rows elements of open port admittance matrix of a dual tuned coil at a 9.4T phosphorous frequency (162.09 MHz). Units are in Siemens (S).

Y_{11}	Y_{12}	Y_{13}	Y_{14}	Y_{31}	Y_{32}	Y_{33}	Y_{34}
-1.006E-02	2.167E-02	2.604E-03	-8.039E-03	2.604E-03	-8.039E-03	-9.232E-03	2.543E-02
1.032E-04	-1.110E-04	2.874E-04	-2.271E-04	2.604E-03	-8.039E-03	3.141E-04	-1.744E-03
6.057E-06	-7.456E-06	3.211E-05	-2.455E-05	2.874E-04	-2.271E-04	7.412E-05	-1.666E-04
1.910E-06	-2.967E-06	1.457E-05	-9.384E-06	3.211E-05	-2.455E-05	2.142E-05	-7.423E-05
1.187E-06	-2.223E-06	1.046E-05	-5.862E-06	1.457E-05	-9.384E-06	1.059E-05	-5.216E-05
9.617E-07	-2.024E-06	9.255E-06	-4.779E-06	1.046E-05	-5.862E-06	6.756E-06	-4.537E-05
9.031E-07	-1.978E-06	9.255E-06	-4.779E-06	9.255E-06	-4.779E-06	5.695E-06	-4.373E-05
9.617E-07	-2.024E-06	1.046E-05	-5.862E-06	9.255E-06	-4.779E-06	6.756E-06	-4.537E-05
1.187E-06	-2.223E-06	1.457E-05	-9.384E-06	1.046E-05	-5.862E-06	1.059E-05	-5.216E-05
1.910E-06	-2.967E-06	3.211E-05	-2.455E-05	1.457E-05	-9.384E-06	2.142E-05	-7.423E-05
6.057E-06	-7.456E-06	2.874E-04	-2.271E-04	3.211E-05	-2.455E-05	7.412E-05	-1.666E-04
1.032E-04	-1.110E-04	2.604E-03	-8.039E-03	2.874E-04	-2.271E-04	3.141E-04	-1.744E-03

Table 13: The magnitude of rows elements of open port admittance matrix of a dual tuned coil at 9.4T sodium frequency (105.9 MHz). Units are in Siemens (S).

Y_{11}	Y_{12}	Y_{13}	Y_{14}	Y_{31}	Y_{32}	Y_{33}	Y_{34}
-2.169E-02	2.841E-02	6.837E-03	-9.894E-03	6.837E-03	-9.894E-03	-2.271E-02	3.183E-02
1.686E-04	-1.700E-04	4.040E-04	-3.996E-04	6.837E-03	-9.894E-03	1.188E-03	-1.926E-03
1.040E-05	-1.057E-05	4.329E-05	-4.201E-05	4.040E-04	-3.996E-04	1.487E-04	-2.020E-04
3.489E-06	-3.638E-06	1.763E-05	-1.688E-05	4.329E-05	-4.201E-05	5.383E-05	-8.001E-05
2.334E-06	-2.478E-06	1.170E-05	-1.112E-05	1.763E-05	-1.688E-05	3.355E-05	-5.191E-05
2.006E-06	-2.149E-06	9.948E-06	-9.419E-06	1.170E-05	-1.112E-05	2.716E-05	-4.283E-05
1.926E-06	-2.069E-06	9.948E-06	-9.419E-06	9.948E-06	-9.419E-06	2.555E-05	-4.054E-05
2.006E-06	-2.149E-06	1.170E-05	-1.112E-05	9.948E-06	-9.419E-06	2.716E-05	-4.283E-05
2.334E-06	-2.478E-06	1.763E-05	-1.688E-05	1.170E-05	-1.112E-05	3.355E-05	-5.191E-05
3.489E-06	-3.638E-06	4.329E-05	-4.201E-05	1.763E-05	-1.688E-05	5.383E-05	-8.001E-05
1.040E-05	-1.057E-05	4.040E-04	-3.996E-04	4.329E-05	-4.201E-05	1.487E-04	-2.020E-04
1.686E-04	-1.700E-04	6.837E-03	-9.894E-03	4.040E-04	-3.996E-04	1.188E-03	-1.926E-03

Table 14: The magnitude of rows elements of open port admittance matrix of a dual tuned coil at 9.4T oxygen frequency (53.4 MHz). Units are in Siemens (S).

Y_{11}	Y_{12}	Y_{13}	Y_{14}	Y_{31}	Y_{32}	Y_{33}	Y_{34}
-4.805E-02	5.130E-02	1.582E-02	-1.728E-02	1.582E-02	-1.728E-02	-5.180E-02	5.615E-02
3.345E-04	-3.353E-04	7.881E-04	-7.923E-04	1.582E-02	-1.728E-02	2.850E-03	-3.187E-03
2.059E-05	-2.061E-05	8.239E-05	-8.247E-05	7.881E-04	-7.923E-04	3.209E-04	-3.462E-04
6.789E-06	-6.806E-06	3.260E-05	-3.265E-05	8.239E-05	-8.247E-05	1.189E-04	-1.307E-04
4.499E-06	-4.516E-06	2.124E-05	-2.128E-05	3.260E-05	-3.265E-05	7.469E-05	-8.253E-05
3.854E-06	-3.870E-06	1.789E-05	-1.794E-05	2.124E-05	-2.128E-05	6.070E-05	-6.713E-05
3.697E-06	-3.713E-06	1.789E-05	-1.794E-05	1.789E-05	-1.794E-05	5.718E-05	-6.325E-05
3.854E-06	-3.870E-06	2.124E-05	-2.128E-05	1.789E-05	-1.794E-05	6.070E-05	-6.713E-05
4.499E-06	-4.516E-06	3.260E-05	-3.265E-05	2.124E-05	-2.128E-05	7.469E-05	-8.253E-05
6.789E-06	-6.806E-06	8.239E-05	-8.247E-05	3.260E-05	-3.265E-05	1.189E-04	-1.307E-04
2.059E-05	-2.061E-05	7.881E-04	-7.923E-04	8.239E-05	-8.247E-05	3.209E-04	-3.462E-04
3.345E-04	-3.353E-04	1.582E-02	-1.728E-02	7.881E-04	-7.923E-04	2.850E-03	-3.187E-03

- First row of each matrix is presented and matrix $\mathbf{Y_{i,k}} = \mathbf{circ}\,(\,Y_{i,k}\,)$
- $\mathbf{Y}_{13} = \mathbf{Y}'_{31}$ and $\mathbf{Y}_{14} = \mathbf{Y}'_{32}$

Appendix D

List of components used in dual tuned coils

Table 15 : List of the components used in a P_{31}- Na_{23} coil.

Name of Component	Manufacturer/Source	Part Number	Total Number
Tube 9.5" dia and 0.5" thickness	McMaster		1
Tube 12.5" dia and 0.25" thickness	McMaster		1
Front End Plate	INSL	Custom built	1
Back End Plate	INSL	Custom built	1
Front End PCB	Advanced Circuits	Custom built	4
Back End PCB	Advanced Circuits	Custom built	4
Variable Capacitor	Johansson	55HO2C	27
Chip Capacitor 3.6 pf	Voltronics		12
Chip Capacitor 7.5 pf	Voltronics		24
Chip Capacitor 9.1 pf	Voltronics		24
Chip Capacitor 13 pf	Voltronics		36
Chip Capacitor 20 pf	Voltronics		24
Chip Capacitor 820 pf	Voltronics		24
Inductor	INSL		2
SMA non-magnetic Connector	Digi-Key		4
Copper Tape	3M		
Nylon Screws	McMaster		24

Table 16 : List of the components used in a $Na_{23} - O_{17}$ coil.

Name of Component	Manufacturer/Source	Part Number	Total Number
Tube 9.5" dia and 0.5" thickness	McMaster		1
Tube 12.5" dia and 0.25" thickness	McMaster		1
Front End Plate	INSL	Custom built	1
Back End Plate	INSL	Custom built	1
Front End PCB	Advanced Circuits	Custom built	4
Back End PCB	Advanced Circuits	Custom built	4
Variable Capacitor	Johansson	55HO2C	27
Chip Capacitor 15 pf	Voltronics		12
Chip Capacitor 20 pf	Voltronics		24
Chip Capacitor 36 pf	Voltronics		24
Chip Capacitor 60 pf	Voltronics		36
Chip Capacitor 110 pf	Voltronics		24
Chip Capacitor 1000 pf	Voltronics		24
Inductor	INSL		2
SMA non-magnetic Connector	Digi-Key		4
Copper Tape	3M		
Nylon Screws	McMaster		24

Appendix E

The PCB layouts for the front and the back boards of a dual tuned coils

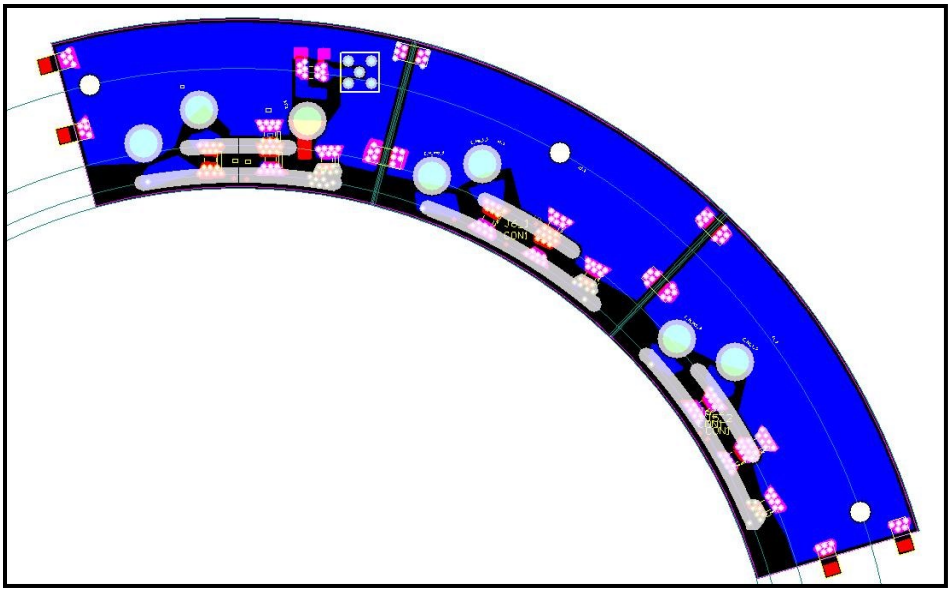

Fig. 40: Front side PCB.

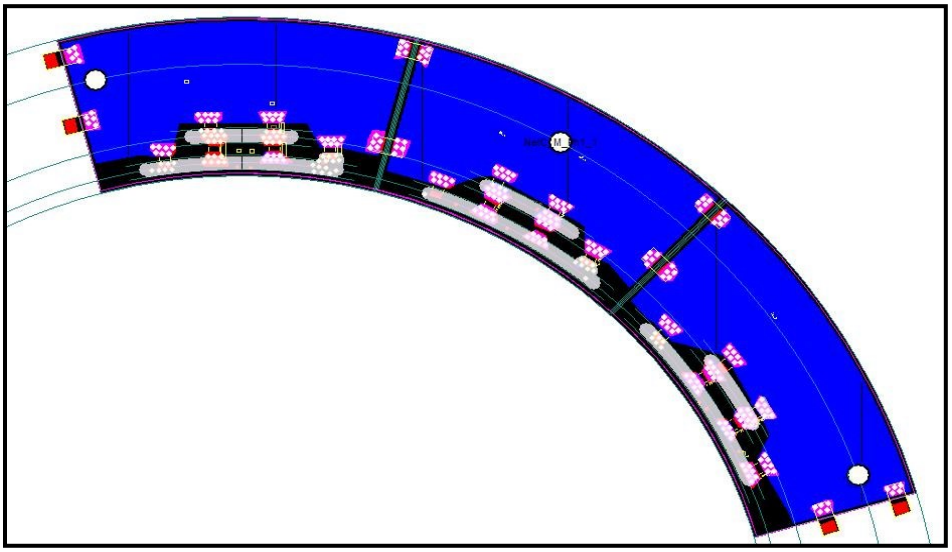

Fig. 41: Back side PCB.